Non-equilibrium long-range phase transition in cold atoms : theory and experiment

Vincent Mancois

Vincent Mancois. Non-equilibrium long-range phase transition in cold atoms : theory and experiment. Physics [physics]. Sorbonne Université; Nanyang Technological University (Singapour), 2018. English. NNT : 2018SORUS427 . tel-02924984

SORBONNE UNIVERSITÉ AND NANYANG
TECHNOLOGICAL UNIVERSITY

Doctoral school n°564: Physique en Ile-de-France

A work under the supervision of

David WILKOWSKI and Pascal VIOT

presented by

Vincent MANCOIS

in partial fulfilment of the requirements for the degree of :

DOCTOR OF PHILOSOPHY

Thesis subject :

Non-equilibrium long-range phase transition in cold atoms: theory and experiment

2018

Jury :

M	Eric BERTIN	Reviewer
M.	Jean-Claude GARREAU	Reviewer
M.	Sylvain GIGAN	Examiner SU
M.	Shau Yu LAN	Examiner NTU
M.	Massimo PICA CIAMARRA	Examiner NTU
M.	Pascal VIOT	Supervisor SU
M.	David WILKOWSKI	Supervisor NTU

Acknowledgement

I would like to thank my two supervisors Pascal Viot and David Wilkowski. They gave me the opportunity to work between two countries on both theoretical and experimental sides of the PhD's project. It was an amazing adventure. They taught me everyday with their respective expertise. I will always remember who to thank, for the first steps in research I was guided through.

I am thanking also the members of the jury for their interest and remarks.

I would like to thank also the two host universities SU and NTU as well as my colleagues in Paris and Singapore. Especially within NTU during the long nights of experiments: Chang Chi Kwong, Frederic Leroux, Manan Jain, Mehedi Hasan, Riadh Rebhi.

I thank my parents for their everlasting support and putting constantly new books between my hands.

Last but not least: I thank my wife Yunuo for lighting up my life everyday.

Contents

List of Figures

List of Tables

Chapter I

Foreword

During this thesis, I studied a cold atomic system interacting by a long-range force arising from the absorption of non-saturating laser beams. The atomic cloud was composed of bosonic strontium 88 (^{88}Sr) cooled and trapped on the $^1\mathrm{S}_0 \rightarrow ^3\mathrm{P}_1$ intercombination line. The same transition is used to create a long-range force. Cooling, then transferring the atoms in a two-dimensional (2D) optical dipole trap (ODT) of very small vertical extension, allows to study the effects of this long-range force in 2D where a phase transition is expected in the canonical ensemble. The long-range force resulting from the absorption of the photons in the cloud, is attractive and similar to the usual Newtonian gravity. Below a certain temperature, the system should collapse, nearly by the same mechanism stars are forming. The almost absent inter-particles scattering of ^{88}Sr in the ground state as well as a very low Doppler temperature close to the photon recoil makes it particularly advantageous to reach high density regimes.

The complexity arising from the narrowness of the intercombination line, which has a natural linewidth about 7.5 kHz, can be circumvented by working at large enough detuning. It is then possible to describe the light-matter interaction in a semi-classical way, the photons playing the role of a thermal reservoir. This picture is suitable to straightforward theoretical and numerical investigations.

The 2D shape given to the atomic cloud by the ODT is responsible for a different trapping potential between the ground state $^1\mathrm{S}_0$ and excited state $^3\mathrm{P}_1$. Those potentials can be made identical for the two states by tuning the ODT wavelength to a so-called magical value. The ODT is polarized vertically out of the plane and the pseudo gravity beams have their polarization in-plane, in order to reduce the effect of the re-emission of photons which contributes to a repulsive force between atoms. For this beam configuration, a magical wavelength exists. Calculation and measurement of the magical wavelength were performed, and we report trapping few 10^5 atoms at about 1 μK before activating the 2D gravity.

The principal characteristics of long-range forces are recalled in Chapter II and the already existing model of extended/collapsed gravitational transition in cold atoms is detailed in 1D and 2D at the end of this chapter. The initial aim of my thesis was thus to realize the 2D collapse experiment. The cloud horizontal shape was asymmetrical for practical reason but numerical simulations showed simply a displacement of the transition critical temperature. I refined the 2D model in Chapter III for more realism and includes finite temperature effects as well as the multiple scattering of photons, responsible for the limitation of the final collapsed phase size. The experimental setup working on the strontium atom, which involves two stages of cooling and the transfer into the dipole trap, is presented in Chapter IV.

Results of the experiment on the ^{88}Sr are presented in Chapter V, where evidences of the 2D gravity was found in one beam configuration among three, where the 4 lasers creating the gravity are at 90° of each other. The collapsed phase can be characterized by a compression factor defined by the ratio between the ratio between the cloud size under the 2D gravity by the cloud size after a long relaxation.

During the experiment, the ODT laser creating the 2D shape of our cloud of atoms started to lose power and drift, we consequently failed to trap efficiently the atoms for a long time and only saw temporary compressions below the critical temperature. The best compressions we saw was obtained for the 4 beam configuration and was about 60%, a value corroborated by recent numerical simulations and giving us hope to publish later those results. However, the loss of precise frequency lock on the ODT and power loss made difficult a quantitative analysis of the compression we observed.

Aside from the investigation of gravitational-like interaction, I studied the possibility of realizing a minimal Brownian motor within a system of trapped particles in 2D, similarly to our experimental situation. In Chapter VI, I describe the double symmetry breaking identified for being responsible for the appearance of a macroscopic current of particles. The 2D cloud ^{88}Sr is proposed as a test system to observe this macroscopic current thanks to a ballistic expansion of the cloud.

Chapter II

Introduction: Newtonian gravity meets cold atoms

In this chapter, we will explain how a cloud of cold atoms in presence of weakly absorbed lasers can be used to mimic long-ranged gravitational interactions. The definitions and peculiarities of LR forces are introduced in Section II.1. The derivation of the 1D artificial gravity force in the context of cold atoms is recalled in Section II.2. The generalization to 2D of this force is presented in Section II.3 alongside the possibility of a non-equilibrium phase transition, supported theoretically and numerically.

II.1 Characteristics of long-range forces

II.1.1 Definition of a long-range force

As opposed to short-range interactions, LR interactions are characterized by a potential algebraically decaying with a power of the inter-particle distance with an exponent smaller than the space dimension. LR forces constitute a very large branch of interactions in statistical physics that can be seen as ill-defined with respect to the theoretical tools we usually have access to. Those tools (ensemble equivalence, thermodynamic limit etc.) are derived from a triad of hypotheses constituting the foundations of statistical physics, that are:

- **Additivity** of the energy of two large systems. Which ensures the existence of a thermodynamic limit or equivalence of the statistical ensembles for large N.

- **Well behaved thermodynamic potentials**, such as concavity/convexity and extensivity for sufficiently large systems. Which ensures ensemble equivalence and thus, a simple framework for the study of phase transitions.

- **Ergodicity**, which ensures the attainability of equilibrium.

While the two first are addressing properties at equilibrium, ergodicity concerns the dynamical ones. Both aspects, equilibrium and dynamics are modified under the influence of LR interactions. The formal characterization of a LR interaction is contained within the algebraical expression of the corresponding two-body potential:

$$V(r) \propto \frac{C}{r^\alpha} \quad \text{with} \quad \alpha \leq d, \tag{2.1}$$

where d is the space dimension. Another definition exists from the force's expression:

$$\mathbf{F}(r) \propto \frac{D}{r^\beta} \quad \text{with} \quad \beta \leq d+1. \tag{2.2}$$

What makes those forces so important in physics and why do we have to question the standard kinetic approach? To answer these questions, we could refer to the remarks Vlasov made in [1] in the context of plasmas and electron gases[1]. In summary, those questions have the following answers. Regarding the first question, gravity and Coulomb interactions are both LR, which justifies on its own physicist's interest for the subject. Regarding the second question, in the context of plasma physics, if one imagines unbalancing the density of positive and negative particles, the system would globally reorganize itself in a search of charge neutrality. It is impossible to imagine changes of the scale of the system by only considering binary interactions, this justifies the seek for another description over the standard Boltzmann one.

a) Consequences of LR forces: non-extensivity

If we consider a sphere of radius r in a d-dimensional space where particles are distributed uniformly, the potential energy of a particle at the origin will be:

$$U(r) \propto C + \int_\epsilon^r \mathrm{d}s \; s^{d-1-\alpha}, \tag{2.3}$$

where ϵ is a short-range cutoff introduced *ad hoc*. $U(r)$ is represented for different values of α in Figure II.1, where C is chosen to cancel the lower bound of the integral in Equation 2.3. For $\alpha \leq d$, the largest contribution to the potential energy comes from large distances. The potential energy is then not bound when r increases, which translates into a lack of extensivity, it is represented by the exclamation points on the Figure.

Extensivity can be recovered formally by renormalizing the coupling constant [2]. Recovering extensivity is important, it means that energy scales with the number of particles N and that the thermodynamical potentials (free energy F and free enthalpy G) scale also as N. Which in the context of phase transitions, is primordial

---

[1] Vlasov coined the denomination *long-range* forces in this article.

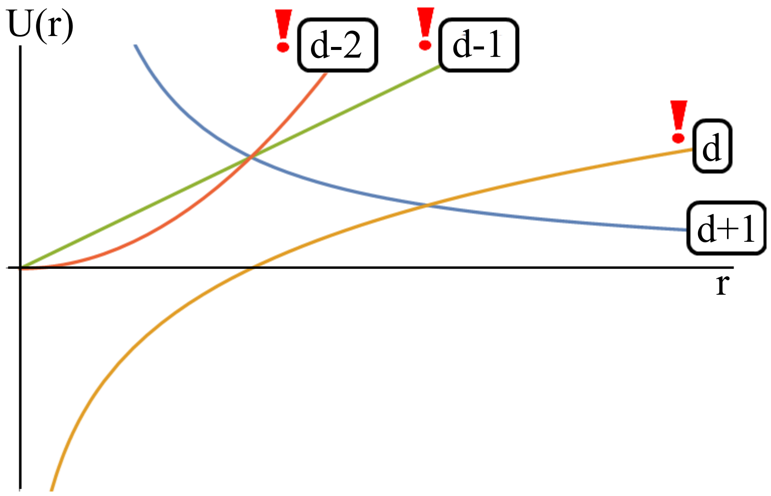

Fig. II.1 *Total potential energy* $U(r)$ *for different 2-body potentials* $1/r^{\alpha}$*. Labels referring to the different values of* α*. When* $\alpha \leq d$ *(long-range force) the potential energy diverges with the distance* r *(exclamation points). While for* $\alpha = d+1$ *and above (short-range force) the energy decreases at infinite.*

to correctly account for the competition between energy and entropy. Although, when extensivity is recovered it may not necessarily be the case for additivity.

b) Consequences of LR forces: non-additivity

Additivity is the property used to derive the canonical ensemble in statistical physics. In substance, additivity says that when coupling two systems of energies E_1 and E_2, the interaction energy between the two is negligible as compared to the sum $E_1 + E_2$ when the sizes of both systems become very large. It is true for short-range interactions. In this case only, the interaction energy is proportional to the interface of contact between the two systems and is thus negligible as long as one of the systems is large enough[2]. It is however dubious for LR forces as the two systems interact with each other not only at their interface. By definition, one cannot decouple two LR interacting systems by putting them apart, so even with no interface or contact the problem persists. Writing E_{12} the interaction energy between the two systems, one would find that the relative ratio $E_{12}/(E_1 + E_2)$ is never going to zero for LR forces. In the construction of the canonical ensemble, we must assume the existence of a heat bath that is not modified by its energy exchanges with a smaller system of interest. However, this "perturbative" picture is forbidden for LR forces and the construction of the canonical distribution is made more difficult.

---

[2] The ratio of the interface energy and bulk energy is supposedly scaling as $V^{\frac{d-1}{d}}$ for short-range forces but not for LR ones.

c) Consequences of LR forces: negative specific heat

An important feature of the entropy function is its concavity. It is admitted for short-range forces because of the following stability argument: combining two identical systems at equilibrium must resist transfers of energy.

$$S(E+\Delta E)+S(E-\Delta E)\leq 2S(E) \quad \leftrightarrow \quad S \text{ concave.} \tag{2.4}$$

The consequence of this property is that the heat capacity at fixed volume and number of particles is positive:

$$\left(\frac{\partial^2 S}{\partial E^2}\right)_{V,N}\leq 0. \tag{2.5}$$

This property is important for several reasons, but mostly because our physical intuition is used to flows of energy "from hot to cold systems", which is ensured as soon as S is concave. A negative specific heat is sometime a feature of LR forces in the microcanonical ensemble, while it is always positive (for SR and LR interactions) in the canonical ensemble because of the properties of the Legendre transformation. If a problem is more likely to be treated in the canonical ensemble, one can access the entropy from the free energy by Legendre transformation which can be schematically represented as follow: entropy ↔ free energy when S is concave. While when S has convex parts, only entropy → free energy holds. We say that the Legendre transformation is an involution for concave functions because if applied twice, it goes back to the original function. However, for convex functions or convex parts of functions, the double Legendre transformation will give the concave envelope of the original function (see *e.g.* [3]). Figure II.2 illustrates this inequivalence and shows an example of convex intruder in the microcanonical entropy computed within the mean-field Blume-Capel model. This model [4, 5] is an extension of the mean-field Ising model for spin 1 which takes into account the local crystal field anisotropy, it was introduced historically to explain the magnetic transitions in dioxide uranium. The fully connected (mean field) version of the Blume-Capel Hamiltonian of the model is:

$$H=\Delta\sum_{i=1}^{N}S_i^2-\frac{J}{2N}\left(\sum_{i=1}^{N}S_i\right)^2. \tag{2.6}$$

The microcanonical entropy S at a given energy is obtained by maximization of a constrained entropy $\tilde{S}$, with respect to the macroscopic magnetization m.

$$S(E)=\sup_m \tilde{S}(E,m) \quad \text{where} \quad m=\frac{1}{N}\left(\sum_{i=1}^{N}S_i\right). \tag{2.7}$$

On the other hand, the canonical entropy is obtained in two steps. The free energy F of the problem is calculated by minimization and the entropy is deduced by Legendre transformation. If the microcanonical entropy (blue solid) was concave,

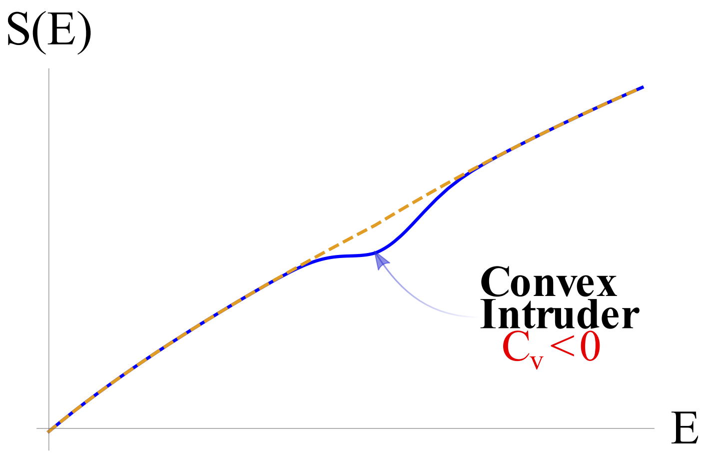

Fig. II.2 *Illustration of ensemble inequivalence in the mean field Blume-Capel model. Entropy (blue solid) and associated concave envelope (orange dashed) by double Legendre transformation.*

the canonical entropy (dashed orange) would be identical to the former. However, due to the presence of a convex intruder, the two entropies do not match: phase diagrams and critical parameters may differ between different ensembles. Indeed, while $S(E)$ is smooth in the microcanonical ensemble, its concave envelope has two discontinuities in first order at the extremities of the convex intruder. Between those two points, the slope is constant. It means that the temperature is constant over a compact set of energies, indicating a first-order phase transition. It has been argued that first-order phase transitions in the canonical ensemble are a signature of LR forces and ensemble inequivalence [6]. On the other hand, in presence of a second-order phase transition in the canonical ensemble, the ensemble equivalence holds over the transition line (see references in [7]).

To understand better the ensemble inequivalence, we can consider the appearance of a convex intruder in the microcanonical entropy but for SR interactions, which originates from finite size effect. Unlike for LR forces, the convex intruder for SR forces becomes closer and closer to the concave envelope when increasing the number of particles. As explained in the previous paragraph, the temperature is constant over this envelope and we can switch to the canonical ensemble to gain some insight on what is going on for the system as the two descriptions are equivalent for SR forces. In the canonical picture, the system absorbs energy while remaining at the same temperature: it indicates the existence of a latent heat and a phase separation. Within the range $[\epsilon_1, \epsilon_2]$ of the convex intruder, additivity ensures that the system of energy ϵ is in a ratio of $c \in [0, 1]$ of phase 1 and $1 - c$ of phase 2 where c is defined as $\epsilon = c\epsilon_1 + (1 - c)\epsilon_2$. Of course, those mixtures are either unstable or metastable because sensitive to time and fluctuations and easily turn into a full phase $c \to 0$ or 1 and are thus difficult to observe.

For LR forces on the other hand, the additivity being lost, one cannot invoke the phase separation argument anymore to explain the behavior of such systems in the convex intruder part of the entropy. This intruder resists the thermodynamic limit $N \to \infty$ and remains a feature of the microcanonical entropy. Because the ensemble construction follows the microcanonical → canonical hierarchy, we have the choice of accepting or denying the original canonical ensemble and keeping the seemingly more fundamental microcanonical one. Another way is to redefine the canonical ensemble in a more consistent way: describing properly a physical situation where a system is interacting with a heat bath. Nevertheless, one of the conceptual difficulties to construct a canonical ensemble for LR forces relies on what is commonly supposed for a system in contact with a thermal bath, that is every subpart is thermalizing independently, which is only possible because of the short-rangedness of interactions. Here because of the overall coupling, the system is trying to thermalize as a whole [8]. Since the coupling between the small system and the heat bath does not scale with the size of the small system as for SR forces, the heat bath may experience significant energy transfers without succeeding in thermalizing the small system or succeed, but at a different temperature [9]. The picture of a heat bath enslaving a smaller one has then to be trade for another one. The definition of a single temperature is also outdated, because the small system kinetic temperature may be different from the thermodynamic (bath) temperature, leading to non-equilibrium dynamics whose lifetime scales with the system size rather than with a mean collision time as for SR interactions. Finally, the kinetic temperature should include the LR coupling constant. This idea will be discussed further in the section dedicated to the Vlasov equation.

d) Consequences of LR forces: ergodicity breaking

Ergodicity is often defined as the equivalence between time average and statistical average for a physical quantity, but what does it really mean for the underlying system? It brings us to the other meaning of ergodicity, in term of attainability of equilibrium. The best is to illustrate the two meanings and their equivalence by a single example.

Due to a symmetry breaking during a phase transition, ergodicity breaking occurs. The reason behind is that the phase space has initially a certain symmetry group, which shrinks after a symmetry breaking. In the 2D Ising model, at high enough temperature the magnetization is zero, and the phase space is maximum. Below the critical temperature, the system will acquire a non-zero positive of negative mean magnetization, which restricts the phase space to only one half of the starting one [11]. If one waits for a while, a macroscopic spin flip may cause the magnetization to reverse, in this case the new phase space is restricted to the other half. However, at the thermodynamics limit, a global flip is no longer possible. As such, ordering leads to symmetry and ergodicity breaking. This point illustrates the inequivalence between statistical and time averaging: if one takes many copies of the system below the critical temperature and calculates the average magnetization, he will conclude on a zero average magnetization. This is because individual copies of the system will have positive and negative magnetizations with equal chances. But a single system will likely keep its non-zero magnetization with a fixed sign. It leads to an inequivalence between statistical average and time average. Now, there is another way to understand this property by focusing on the dynamics of the system. Because of the spontaneous magnetization acquired by a LR Ising system below the critical temperature, the set of thermodynamic parameters may lose its convexity as a consequence of the lack of additivity. Indeed, additivity ensures that we can divide a system into two subsystems of magnetization m_1 and m_2 and by tuning the respective size of those subsystems have a total magnetization $m = \alpha m_1 + (1-\alpha)m_2$ for any $\alpha \in [0,1]$. Figure II.3 shows the non-convex set of parameters between the points **c** and **d** while the line segment between **a** and **b** is contained in the parameter set. The two lines describe dynamics taking place in the microcanonical ensemble (fixed energy ϵ) while the magnetization m varies. Starting from a configuration in **c**, the system is unable to across the gap toward the **d** point. It is understood as follows in the context of spin models: the only accessible states at low energy are macroscopic states of a given polarization with a macroscopic fraction of the spins pointing in the same direction. Trying to move from one state to another without changing the energy, requires the whole system to flip at once. The non-ergodicity as well as the non-convexity of the parameters space are a consequence of the stiffness of the low-energy states. One way to restore ergodicity, would be to add fluctuations (thermal/quantum). It can be done by coupling the spins to a heat bath, the system would then explore higher energy states and be more likely to jump over the gap.

For LR interacting systems, two time-scales and dynamical phases are at play. A first collisionless phase dominated by the LR effects, followed by a collisional phase

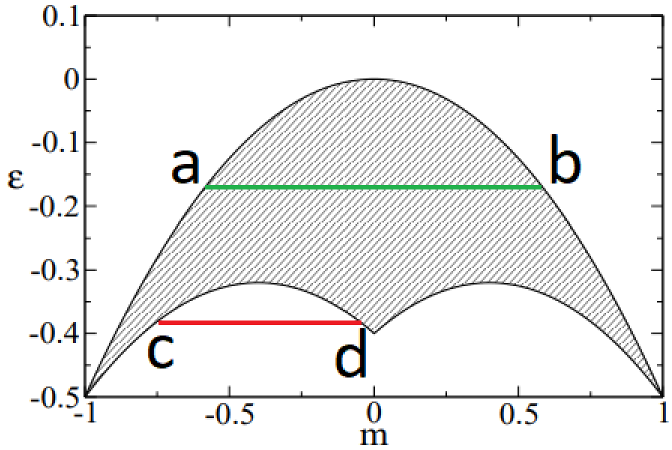

Fig. II.3 *Example of non-convex set of parameters accessible in the (ϵ, m) plan. All rights reserved D. Mukamel et al. [10] © 2005.*

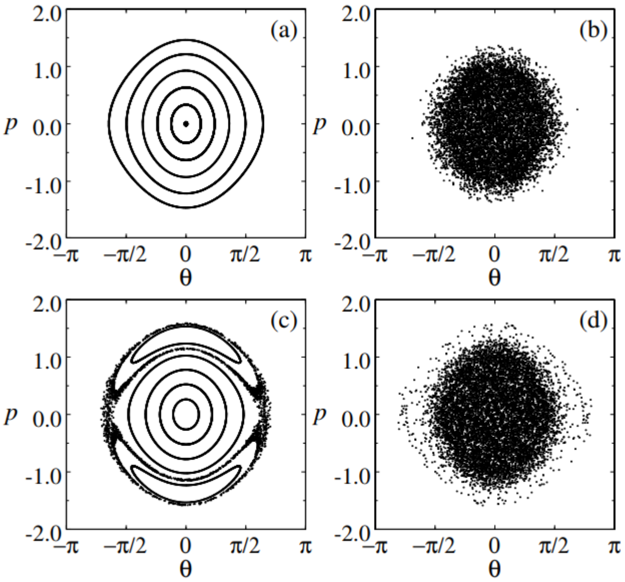

Fig. II.4 *Phase space snapshots of test particles in the HMF model. All rights reserved F.P. Benetti et al. [12] © 2012.*

dominated by SR interactions. The collisionless dynamics can be described by a Vlasov equation [13] for times scaling as $\ln(N)$ with an arbitrary good precision. The precision reduces beyond this time. If one waits longer, after a time $\propto N^{\delta}$ which characterizes the beginning of the collisional relaxation, the Vlasov approach ceases to be conceptually valid. Already within the Vlasov framework, ergodicity breaking occurs for LR forces [12] when the system is not initially virialized, leading to parametric resonances. Such resonances happen for some LR toy models as the Hamiltonian Mean Field model (HMF) describing N particles moving on a circle of radius one[3]. The effect of non-virialization and ergodicity breaking in the HMF model are reproduced in Figure II.4. While for ergodic systems, particles explore a convex portion of the entire phase space as shown by the Poincaré section in (a) and the phase-space snapshot in panel (b). It may follow from non-virial systems, the appearance of isolated islands where the system remains as shown in panels (c) and (d). Because of those islands, particles may remain stuck there, carrying energy away from the system's center and indicating an irreversible ergodicity breaking.

---

[3] The HMF model is defined by the Hamiltonian: $H = \sum_{i=1}^{N} \frac{p_i^2}{2} + \frac{1}{2N} \sum_{i,j=1}^{N} [1 - \cos(\theta_i - \theta_j)]$, where the $\{\theta_i\}$ indicate the particle positions on the circle.

II.2 Long-range interactions on table-top experiments

II.2.1 Former realizations

LR interacting systems are ubiquitous in physics. A system of neutral atoms at low temperature are known to experience this type of forces. The dipole-dipole interaction between two atoms has a R^{-3} dependence and LR dynamics have been observed in photo-association and excited Rydberg atoms experiments [14, 15, 16]. In the context of degenerate quantum gases, a $1/r$ force can be obtained from the dipole-dipole interaction of far off-resonant laser beams with a Bose-Einstein condensate [17].

Other realizations of long-range forces involve the usual Coulomb interaction between trapped ions (see [18, 19] for the first realizations in 1D). However, the inter-particles spacing between ions in those Coulomb crystals is about 10 μm [20] and is thus limiting the maximum density one can reach with those systems. Also, the single-species ions cloud is dominated by repulsive Coulomb force, while we are interested in this thesis by attractive long-range forces between particles. Hence not encouraged on using ions.

The physics of Rydberg atom is well developed as it constitutes a benchmark for quantum computation with neutral atoms. The strong LR forces between Rydberg states has surprising consequences on the dynamics of those atoms. One of those consequences, the Rydberg blockade (or dipole blockade) that has the effect of controlling the quantum state of one or several atoms, had been proposed [21] and used for quantum computing and fundamental entanglement tests [22, 23, 24]. Using two mesoscopic (about 20 atoms each) entangled clouds of Rydberg atoms, the overall dynamics can be shown to be sensitive to LR effects [25].

Propositions have been made to realize two-dimensional gravity by means of capillary interaction between colloids [26] and thermally driven gravitation by means of laser-colloids interactions [27]. Yet, no experimental realization of 2D gravitational-like dynamics has been achieved.

II.2.2 Radiation pressure as a long-range force

In this section we recall the results of [28]. They show that under certain circumstances, a pair of contra-propagating laser beams induces an attractive LR force of gravitational type in a one-dimensional cloud of cold atoms. Cold strontium-88 clouds are ideal platforms for those experiments because for their low atom-atom scattering properties and low Doppler temperature. The artificial gravity is created by addressing the intercombination line between the $^1\mathrm{S}_0 \rightarrow {}^3\mathrm{P}_1$ states. Under the influence of this quasi-gravity, the cloud of cold strontium trapped in a 1D cigar takes the characteristic shape of a self-gravitating system [29]. More details on 1D gravitational systems can be found in [30]. This section is first devoted to the derivation of the 1D gravitational force in the context of cold atoms.

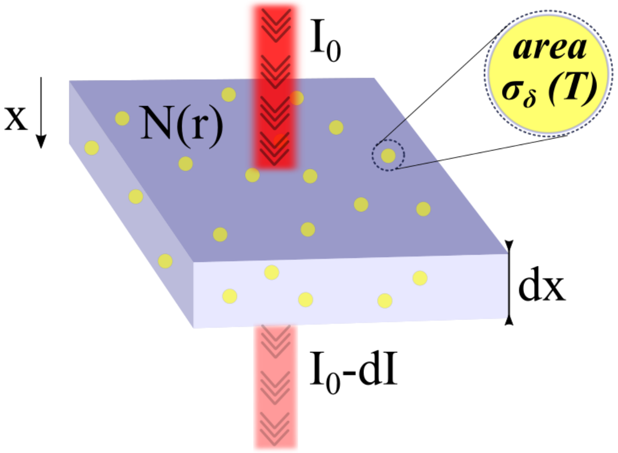

Fig. II.5 *Attenuation of the light intensity* I_0 *on a length* $\mathrm{d}x$ *due to a medium of atomic density* $N(\mathbf{r})$*. Each atom has an absorption cross-section* $\sigma_\delta(T)$*.*

As depicted in Figure II.5 we consider a laser beam propagating forward along $\hat{x}$ and passing through a medium made of N atoms of mass m. We denote the particles density as $N(\mathbf{r})$. In practice, the medium can be made 1D, 2D or 3D by addition of a trapping, it is realized practically by a dipole trap. In order to study the effect of the absorption of the laser passing through the medium, we model simply a slab in the yz plan, where each atom has an average absorption cross-section of $\sigma_\delta(T)$. This quantity depends on the detuning and temperature. The laser intensity $I(\mathbf{r})$ is attenuated along its propagation according to the differential Beer's law:

$$dI(\mathbf{r}) = -N(\mathbf{r})\sigma_\delta(T)I(\mathbf{r})\,\mathrm{d}x, \tag{2.8}$$

The atom finite temperature translates into a Doppler broadening of the spectral lines. The scattering properties of atoms by light -described by the absorption cross-section- are then modified depending on the temperature. This dependence is included formally by taking the convolution product of the zero-temperature absorption profile (Lorentzian of FWHM Γ) by the Boltzmann distribution: Gaussian of Variance[4] $\bar{v} = \sqrt{k_B T/m}$ where k_B is the Boltzmann constant. The convolution product describing the absorption, is the same for photons coming from either $\pm\hat{x}$ unless the medium has a non-zero global motion. Supposing the atoms to have a velocity $v\mathbf{e_x}$, we can thus write:

$$\sigma_\delta(T) = \sigma_0 \int_{\mathbb{R}} \mathrm{d}v \frac{e^{-v^2/2\bar{v}^2}}{\bar{v}\sqrt{2\pi}} \frac{1}{1 + I(\mathbf{r})/I_s + 4(\delta - kv)^2/\Gamma^2}, \tag{2.9}$$

---

[4] Or RMS if the center of mass of the atomic cloud is at rest.

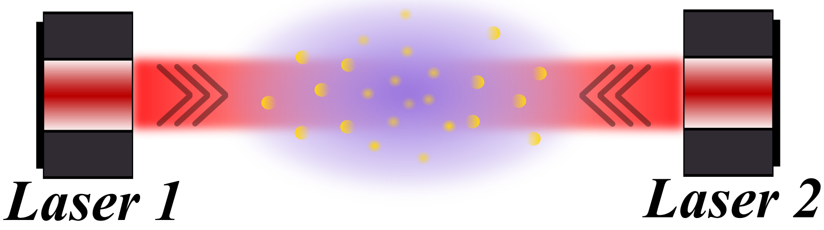

Fig. II.6 *Illustration of the absorption of two contra-propagating lasers. The brightest the atom is, the stronger the differential force it will experience.*

where the factor $\sigma_0 = 6\pi/k^2$ represents the zero temperature and resonant absorption cross-section. Also, we note something important not to be forgotten: the intensity must appear at the denominator to account properly for saturation and deviation from the Beer law (which does not account for saturation). However, for large enough detunings or low intensities, the term can be dropped, as it is the case in our experiment. To be closer to the real situation we infer on the spatial distribution of the atoms. In the experiment, the atoms are trapped in an optical dipole trap (see Chapter III Section III.3), well described by a multi-Gaussian distribution:

$$N(\mathbf{r}) = N \prod_i \frac{1}{\sqrt{2\pi}\sigma_i} e^{-x_i^2/2\sigma_i^2} = Nn(\mathbf{r}). \tag{2.10}$$

Where $N(\mathbf{r})$ is normalized to N and $n(\mathbf{r})$ is normalized to 1. We also precise the intensity profile to be Gaussian transversally and constant over the direction of propagation (collimated beam):

$$I(\mathbf{r}) = I_0 e^{-(y^2+z^2)/2w_\perp^2} I(z). \tag{2.11}$$

The Beer's law integrated gives access to the usual exponential absorption:

$$I(x) = e^{-\overrightharpoon{b_x}(\mathbf{r})} \quad \text{with} \quad \overrightharpoon{b_x}(\mathbf{r}) = \sigma_\delta(T) \int_{-\infty}^{x} dx' N(x', y, z). \tag{2.12}$$

The quantity $\overrightharpoon{b_x}(\mathbf{r})$ (resp. $\overleftharpoon{b_x}(\mathbf{r})$) is the *optical thickness* seen by the attenuated beam propagating positively (resp. negatively) along $\hat{x}$. As depicted in Figure II.6, in the case of two *identical* contra-propagating beams and under the hypothesis of a low optical thickness, we can add up the contributions coming from the two lasers. We assume that the light detuning is large enough compared to the Doppler broadening and natural linewidth to take the semi-classical expression of the radiation pressure. The differential force experienced by an atom at position $\mathbf{r}$ and of velocity $\mathbf{v}$ is then:

$$\mathbf{F}_{1\mathrm{D}}(\mathbf{r},\mathbf{v}) = \hbar\mathbf{k}\frac{\Gamma}{2}s_0 e^{-(y^2+z^2)/2w_\perp^2}\left(\frac{\overrightarrow{b}_x(\mathbf{r})}{1+4(\delta-\mathbf{k}\cdot\mathbf{v})^2/\Gamma^2} - \frac{\overleftarrow{b}_x(\mathbf{r})}{1+4(\delta+\mathbf{k}\cdot\mathbf{v})^2/\Gamma^2}\right). \tag{2.13}$$

Where $s_0 = I_0/I_s$ is the saturation[5] parameter. The exponential prefactor comes from the transverse intensity profile, which can be dropped when the beam waist is much larger than the atomic medium *i.e.* when $w_\perp \gg \sigma_y, \sigma_z$. We will put ourselves in this situation experimentally and consider a weak saturation parameter $s_0 \ll 1$. Thus, we may consequently write:

$$\mathbf{F}_{1\mathrm{D}}(\mathbf{r},\mathbf{v}) = \hbar\mathbf{k}\frac{\Gamma}{2}s_0\left(\frac{\overrightarrow{b}_x(\mathbf{r})}{1+4(\delta-\mathbf{k}\cdot\mathbf{v})^2/\Gamma^2} - \frac{\overleftarrow{b}_x(\mathbf{r})}{1+4(\delta+\mathbf{k}\cdot\mathbf{v})^2/\Gamma^2}\right). \tag{2.14}$$

At low temperature or large detuning $|\delta| \gg |\mathbf{k}\cdot\mathbf{v}|$ the denominators are equal as the laser frequency seen in the atomic frames does not vary too much. We are left with:

$$\begin{aligned}\mathbf{F}_{1\mathrm{D}}(\mathbf{r}) &= \hbar\mathbf{k}\frac{\Gamma}{2}s_0\left(\frac{\overrightarrow{b}_x(\mathbf{r}) - \overleftarrow{b}_x(\mathbf{r})}{1+4(\delta/\Gamma)^2}\right) && (2.15)\\ &= \hbar\mathbf{k}\frac{\Gamma}{2}s_0\left(\frac{N\sigma_0}{[1+4(\delta/\Gamma)^2]^2}\int_{\mathbb{R}} dx'\mathrm{sgn}(x'-x)n(x',y,z)\right). && (2.16)\end{aligned}$$

Taking the divergence of this force gives

$$\boldsymbol{\nabla}\cdot\mathbf{F}_{1\mathrm{D}}(\mathbf{r}) = \hbar k\Gamma s_0\frac{N\sigma_0}{[1+4(\delta/\Gamma)^2]^2}n(\mathbf{r}) \tag{2.17}$$

which is proportional to the density which is enough to prove that this force is algebraically equivalent to a 1D gravity.

II.2.3 Narrowband versus broadband transition

We made a quite non-trivial approximation while writing Equation 2.13, we indeed supposed that the transition is broad. This hypothesis relies on the condition that the natural linewidth of the transition addressed by the lasers is much larger than the photon recoil frequency. This hypothesis is then formally written:

$$\frac{(\hbar k)^2}{2m} \ll \Gamma. \tag{2.18}$$

---

[5] The saturation intensity I_s [31] is a convenient unit to express the laser intensity.

It is equivalent to say that the absorption of one photon does not put the atom out of resonance and usually yields to describe the system's density function by a Fokker-Planck equation [32]. When we do so, we assume the internal state of the atom to be reaching a stationary regime much faster than the external degrees of freedom (position and velocity). Since the internal state transient regime is of the order of Γ^{-1} s, we need the natural linewidth to be large (MHz or more) in order to decouple internal and external degrees of freedom.

In our case, the artificial gravity is created by addressing the intercombination line of strontium, this transition is narrow $\Gamma = 2\pi \times 7.5$ kHz. This linewidth has the subscript r because the color of the transition is red as well as the laser addressing it. The reason why we are still using the semi-classical expression of the force is because we take a detuning large enough as compared to the linewidth: $|\delta| \gg |\mathbf{k}\cdot\mathbf{v}|$, the absorption of a single photon is thus preferentially happening on the edge of the atomic velocity distribution and does not change strongly the scattering properties of the atom. It would not be the case close to resonance, where a single photon can change the detuning sign and thus change the scattering properties of the atom quantitatively.

In summary, the broadband approximation allows to describe the evolution of the velocity and position by small steps and to write mean forces such as Equation 2.13. For this reason, the broadband approximation allows a Brownian approach to the light-matter interaction. Otherwise, a full quantum treatment should be applied. We fortunately avoid this difficulty by choosing a large enough detuning.

II.2.4 Time evolution under the artificial gravity: general Smoluchowski equation

The atom dynamics is thus dictated by a semi-classical force. The internal variables evolving too quickly to be resolved by an observation on the external degrees of freedom. It is thus possible to write in a classical fashion, a Fokker-Planck equation by identifying correctly the elementary steps generating the diffusion process: the photon absorption and re-emission without surprise. It ultimately yields to the following [33] Vlasov-Fokker-Planck (VFP) equation:

$$\frac{\partial f}{\partial t} + \mathbf{v}\cdot\nabla_{\mathbf{r}} f + \frac{1}{m}\nabla_{\mathbf{v}}\cdot\left(\mathbf{F}(\mathbf{r},\mathbf{v})f\right) = D\frac{\partial^2 f}{\partial v^2}. \tag{2.19}$$

Where $f(\mathbf{r},\mathbf{v},t)$ is the phase space distribution function which encapsulates all the information about the N atoms interacting with light, D is the velocity diffusion coefficient originating from the photons re-emission and $\mathbf{F}(\mathbf{r},\mathbf{v})$ accounts for all averaged forces the atoms are subject to. Experimentally we have the following forces: a LR artificial gravity $\mathbf{F}_G(\mathbf{r},t)$ created by a certain number of lasers. If we work with a pair of lasers, we will write $\mathbf{F}_{1D}$, if we work with two orthogonal pair of lasers we will write $\mathbf{F}_{2D}$. We also have a harmonic trap with the restoring force $-m\sum_i \omega_i^2 \mathbf{x}_i$ created by an optical dipole trap. Finally, we have a friction force $-m\gamma\mathbf{v}$ resulting from the artificial gravity force which is also responsible for the temperature definition of the atoms. This last force is obtained by taking the lowest order in velocity of the force 2.13.

Equation 2.19 is characteristic of a Fokker-Planck equation as it expresses velocity diffusion through the right-hand term but also characteristic of a Vlasov equation as it has on its left-hand side, terms describing a collisionless dynamics of particles interacting with a LR force. To solve this partial differential equation, several assumptions can be made on the phase space density. We address first its separability. One must be careful with LR forces which show strong $\mathbf{r}-\mathbf{v}$ correlations in the microcanonical ensemble [34]. Our situation is however a bit special, as the laser brings energy to the system, it is obviously open and non-isolated. As such, the situation can be described in the canonical ensemble [35], the $\mathbf{r}-\mathbf{v}$ correlations may be dropped, and the phase space density is separable. As the atoms interact with the laser, they exchange energy at a certain rate Γ^{-1}. If this rate is much faster than any other time-scale, it may be correct to study the system in an overdamped limit where:

$$f(\mathbf{r},\mathbf{v},t) \xrightarrow{t\gg\Gamma} n(\mathbf{r},t)g(\mathbf{v}). \tag{2.20}$$

Separating position and velocity is also equivalent to describe a thermal equilibrium [36]; However, this hypothesis deserves to be scrutinized. The photon scattering rate scales as Γ^{-1} [37], which is in our case about 21 microseconds, the thermalization time should be no longer than few milliseconds [38] and is short as compared to usual trapping period in cold atoms experiment. It is thus safe to assume the system thermalized quite fast under the influence of the artificial gravity beams. However, it does not presuppose anything on the shape of the velocity distribution that is reached and depends on: the natural linewidth/detuning and also on additional trapping. Thanks again to the large detuning hypothesis, the velocity distribution does not deviate too far from a Gaussian [39]. Also, we work with quite modest trapping frequencies and are not bothered by the interplay between the trap characteristic time and thermalization characteristic time [40]. Injecting the separability/overdamped approximation for the phase-space distribution into the Fokker-Planck equation, multiplying by v_x and integrating over the velocity yields:

$$\begin{cases} m\bar{v_x}^2 \dfrac{\partial n(\mathbf{r},t)}{\partial x} = n(\mathbf{r},t)\mathbf{F}(\mathbf{r})\cdot\mathbf{e}_x, & (2.21) \\ \text{with } \ \mathbf{F}(\mathbf{r}) = -m\sum_i \omega_i^2\mathbf{x}_i + \mathbf{F}_G(\mathbf{r},t), & (2.22) \end{cases}$$

We see that the friction force is apparently gone, it has been absorbed into the temperature and is hidden inside the mean velocity $\hat{v}_x$. This equation can be used to find the stationary distribution at one dimension, soon below.

If we wish to follow the dynamics of the spatial distribution, then we must use another type of equation. There is a simple procedure, that allows to re-express the initial VFP Equation 2.19 acting on $f(\mathbf{r},\mathbf{v},t)$ into one (see [36] for the complete derivation) acting on $n(\mathbf{r},t)$. In the overdamped limit, the spatial distribution is not at equilibrium, but the velocity is (*Ibid*). We can then eliminate the velocity from the problem and recast the continuity equation on the spatial density. The transition between Fokker-Planck equations and continuity equations in phase space bear resemblance with the Navier-Stokes equations in fluid dynamics, we explain it now. We first notice that the diffusion described by the Fokker-Planck equation is in position and velocity. Secondly, we notice that, if the process at the origin of the diffusion has a high repetition rate and changes infinitesimally the values of the system's macroscopic variables, the dynamics will be smooth and thus an observer will not resolve the diffusion step by step. In our situation of atoms under the effect of light, the high repetition rate indicates that the atoms mean velocity and thus temperature are given *at any time* by the light intensity and detuning. The atom-light interaction is then identical to a situation within the canonical ensemble, where photons would play the role of a heat bath. As found in [41], the general Smoluchowski equation of the problem is:

$$\frac{\partial n(\mathbf{r},t)}{\partial t} = \nabla \cdot \left(\sum_i \frac{\omega_i^2}{\gamma} \mathbf{x}_i n(\mathbf{r},t) - \frac{\mathbf{F_G}(\mathbf{r})}{m\gamma} n(\mathbf{r},t) + \frac{k_B T}{m\gamma} \nabla n(\mathbf{r},t) \right). \tag{2.23}$$

Where we see explicitly this time the friction coefficient γ and defined $D = k_B T/m\gamma$ the spatial diffusion coefficient. This equation has sometimes the denomination Smoluchowski-Poisson (SP) equation. The Poisson's touch coming from the fact that the LR force obeys the same Poisson equation as gravity in one dimension. We will now recast this equation within a set of dimensionless parameters to anticipate its numerical resolution and theoretical investigation. The rescaling has also the effect of removing γ from the equation which is justified by the overdamped approximation.

II.2.5 2D Smoluchowski equation

Our experiment addresses specifically the 2D artificial gravity, we can thus refine the general Smoluchowski equation 2.23. We start by replacing the unspecified $\mathbf{F_G}$ by $\mathbf{F}_{\mathrm{2D}}$ resulting from the absorption of 4 contra-propagating lasers along the $\hat{x}$ and $\hat{y}$ axes. The harmonic trap is supposed to have an infinitely small extension vertically ($\omega_z \gg \omega_x, \omega_y$) and a finite size horizontally ($\omega_x = \omega_y = \omega_\parallel$). Because of this excessive asymmetry, we eliminate the z variable of the problem putting ourselves in the plan $z = 0$. The only remnant of the vertical spatial extension is kept within the factor $1/\sigma_z\sqrt{2\pi}$ coming from the normalized 2D density $n(\mathbf{r}_{\mathrm{2D}})$. We thus have $n(\mathbf{r}) = \frac{1}{\sigma_z\sqrt{2\pi}} n(\mathbf{r}_{\mathrm{2D}})$.

$$\begin{aligned}\mathbf{F}_{2\mathrm{D}}(\mathbf{r}) &= \hbar k\frac{\Gamma}{2}s_0\left(\frac{[\overrightarrow{b}_x(\mathbf{r})-\overleftarrow{b}_x(\mathbf{r})]\mathbf{e}_x+[\overrightarrow{b}_y(\mathbf{r})-\overleftarrow{b}_y(\mathbf{r})]\mathbf{e}_y}{1+4(\delta/\Gamma)^2}\right)\\ &= C\int_{\mathbb{R}}[dx'\mathrm{sgn}(x'-x)n(x',y)\mathbf{e}_x+dy'\mathrm{sgn}(y'-y)n(x,y')\mathbf{e}_y],\end{aligned} \tag{2.24}$$

with the introduction of the constant C giving a typical energy scale of the 2D artificial gravity.

$$C=\frac{\hbar k\Gamma}{2}s_0\frac{N}{\sigma_z\sqrt{2\pi}}\frac{\sigma_0}{(1+4(\delta/\Gamma)^2)^2}. \tag{2.25}$$

In a second time, we rescale the time and position variables as:

$$t(\mathrm{old})=\frac{\gamma}{\omega_\parallel^2}t(\mathrm{new})\quad\text{and}\quad\mathbf{r}_{2\mathrm{D}}(\mathrm{old})=\sqrt{\frac{C}{m\omega_\parallel^2}}\mathbf{r}_{2\mathrm{D}}(\mathrm{new}). \tag{2.26}$$

We thus lose sight of the friction coefficient γ. It is normal since it characterizes the fastest timescale from the problem and must disappear somehow by the overdamped approximation.

Now that the natural units for the equation have been chosen, we can rewrite the SP equation

$$\frac{\partial n(\mathbf{r}_{2\mathrm{D}},t)}{\partial t}=\nabla\cdot\left[\mathbf{r}_{2\mathrm{D}}n(\mathbf{r}_{2\mathrm{D}},t)-\mathbf{F}_{\mathbf{G}}(\mathbf{r}_{2\mathrm{D}})n(\mathbf{r}_{2\mathrm{D}},t)+\Theta\nabla n(\mathbf{r}_{2\mathrm{D}},t)\right], \tag{2.27}$$

as a function of the position $\mathbf{r}_{2\mathrm{D}}=(x,y)$ and the reduced temperature Θ

$$\Theta=\frac{k_BT}{C}. \tag{2.28}$$

We derived the equation of evolution of a system of cold atoms in the presence of a harmonic trap and a gravitational force in two dimensions for an arbitrary number of beams in the xy plan. We are thus free to choose any beam configuration we wish. The SP equation is useful to describe systems in the canonical ensemble (fixed T) and in the microcanonical ensemble (varying $T(t)$). The stationary solutions of the SP equation correspond to local entropy maxima or free-energy minima. But those stationary solutions which correspond to a finite entropy are not the only solutions toward which the dynamics is attracted. Since those extrema are only local, the system may either attracted toward those solutions or collapse. It is the subject of the next paragraphs, to determine the possibility of gravitational collapses within the frame of the SP equation.

a) Remarks: thermodynamic ensembles and space dimension

Within the canonical ensemble, for self-gravitating systems in one dimension [29], the gravity never overcomes the diffusion and the cloud remains diluted. A similar conclusion is obtained in the microcanonical ensemble, as the non-singular potential cannot lead to a divergence of the density. In conclusion, the one-dimensional self-gravitating system is known to be stable and we will derive within the section below its stationary distribution.

The situation is different in 2D [42], as the cloud can collapse in the canonical ensemble, albeit not in the microcanonical one.

If we were in the microcanonical ensemble, the ansatz for the separability of the phase-space density and the hypothesis that there is no $\mathbf{r}-\mathbf{v}$ correlations would fall apart. However, our system of cold atoms is not a standard self-gravitating system because of the presence of the lasers defining the temperature and killing the cross-correlations. Having the advantage of working in the canonical ensemble, we propose to re-derive the stationary distribution for the 1D gravity below before addressing the collapse with the 2D gravity.

b) Remarks: 1D configuration

If the gravitational force $F_G(\mathbf{r})$ has only one component along $\hat{x}$ which means a pure 1D gravity, there is no collapse [43]. The diffusion is always stronger than attraction as there is no singularity in the potential. This model describes correctly the 1D experiment [28] ran with strontium 88 atoms. In the experiment, the presence of the LR force is probed directly (spatial density) and indirectly (breathing oscillations). The spatial distribution reaches a stationary profile that has an analytical expression [29]. We suppose the gravitational force acting only along $\hat{x}$. We then have:

$$\frac{\partial n(x,y,z)}{\partial x} = \frac{\hbar k}{k_B T}\frac{\Gamma}{2} N s_0 \frac{\sigma_0}{[1+4(\delta/\Gamma)^2]} n(x,y,z) \int \mathrm{d}x' \mathrm{sgn}(x'-x) n(x',y,z). \quad (2.29)$$

From this integro-differential equation, we start by factorizing $n(x,y,z) = n(x)n(y,z)$ and set $y = z = 0$. We also define a new quantity $\bar{x}$, such that:

$$\bar{x} = \left(\frac{\hbar k}{k_B T}\frac{\Gamma}{2} s_0 \frac{N\sigma_0}{[1+4(\delta/\Gamma)^2] 2\pi\sigma_y\sigma_z}\right)^{-1}. \quad (2.30)$$

The factor $2\pi\sigma_y\sigma_z$ appearing from obvious reasons when looking at Equation 2.10. We are thus left with the following equation to solve:

$$\frac{\partial n(x)}{\partial x} = \frac{n(x)}{\bar{x}} \int \mathrm{d}x' \mathrm{sgn}(x'-x) n(x'). \quad (2.31)$$

This differential equation can be made linear in two steps, first by introducing the variable

$$I(x) = \int_{x}^{+\infty} \mathrm{d}x' n(x'). \tag{2.32}$$

We obtain then:

$$I''(x) - \frac{1}{\bar{x}} I'(x)[2I(x) - 1] = 0. \tag{2.33}$$

We integrate this equation once and perform another change of variable $I(x) = 1/K(x)$. It yields to the linear equation:

$$K'(x) + \frac{1}{\bar{x}} K(x) = \frac{1}{\bar{x}}. \tag{2.34}$$

Rewinding to the initial function and having the initial condition $I(0) = 1/2$ by symmetry of the distribution function, we obtain the stationary distribution in one dimension:

$$\boxed{n(x) = \frac{1}{4\bar{x}} \frac{1}{\cosh^2(x/2\bar{x})}.} \tag{2.35}$$

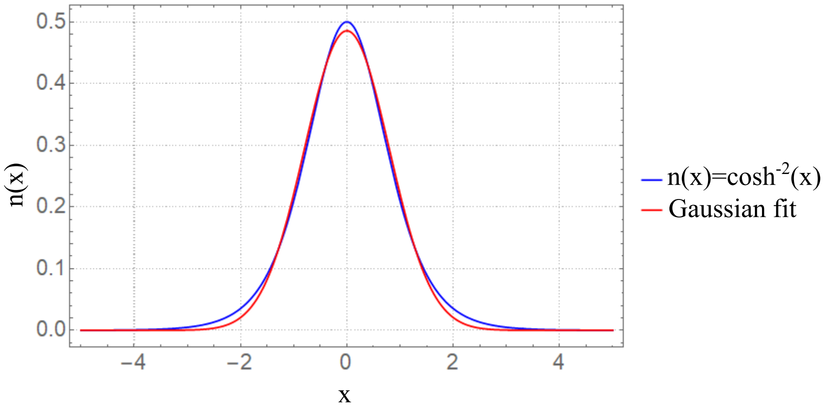

Fig. II.7 *Stationary position distribution for with (blue solid) and without (red solid) the 1D gravitation. The deviation from the Gaussian is seen in the wings and indicative of the LR force.*

Figure II.7, shows this distribution in one dimension and how it deviates from a Gaussian distribution. Deviations from the Gaussian distribution are visible in the left and right tails of the distribution and originate from the LR force. The simple inspection of the spatial distribution is thus limited to characterize the LR force. Another method, indirect, can be used to characterize the LR force rather than looking at the spatial distribution at rest. By giving a kick to the atom in the harmonic trap, the oscillations of the center of mass can be measured as well as their frequency. It has been showed, that the frequency of those oscillations is modified [44] due to the LR force. It illustrates how the motion of the overall system is affected by the LR nature of the interactions. The experiment of the 1D gravity with cold atoms was realized and characterized directly and indirectly as mentioned before in reference [28].

II.3 Realization of a 2D self-gravitating system

II.3.1 Phase transition in 2D: real versus artificial gravity

We mentioned previously that a two-dimensional SGS of particles is known to show a phase transition [45, 42] in the canonical ensemble[6]. Consider a homogeneous disk of radius R and total mass m. We put this system in contact with a heat bath at temperature T and wish to know whether the system can collapse. Since the easiest way to characterize the collapse is to imagine all the particles at the minimum of the gravitational potential, we can verify if the system is thermodynamically favorable to a configuration where $R \to 0$ at fixed T and m. Since we suppose a certain distribution -a disk a radius R- we can compute the Boltzmann entropy defined as:

$$S = -\int \mathrm{d}^2r\, \mathrm{d}^2v f(\mathbf{r}, \mathbf{v}) \ln f(\mathbf{r}, \mathbf{v}). \tag{2.36}$$

Where $\int \mathrm{d}^2r\, \mathrm{d}^2v f(\mathbf{r}, \mathbf{v}) = 1$. Since the system is in a gravitational field, the balance between energy and entropy will lead eventually to an equilibrium. The most suitable thermodynamic potential to look at when one wishes to vary the temperature of a system at a fixed energy E is the Massieu function, defined:

$$J = S - \beta E, \tag{2.37}$$

where $\beta = 1/k_B T$ is the Boltzmann factor. As the system is homogeneous and at temperature T, we maximize S at fixed temperature, energy and density, and obtain that the phase space distribution factorizes as:

$$f(\mathbf{r}, \mathbf{v}) = \rho_0 H(|\mathbf{r}| \leq R) \frac{e^{-\mathbf{v}^2/2\bar{v}^2}}{2\pi\bar{v}^2}. \tag{2.38}$$

where H is the Heaviside step function, $\bar{v} = \sqrt{k_B T/m}$ the mean velocity and ρ_0 the constant mass density such that $\rho_0 = m/\pi R^2$. We now compute every term of the right-hand side of the Massieu function J. Starting with the energy:

$$E = m^2\bar{v}^2 + \frac{1}{2}\rho_0 \int_{|\mathbf{r}|<R} \mathrm{d}^2r\ \Phi(\mathbf{r}). \tag{2.39}$$

---

[6] In the microcanonical ensemble, a maximum of entropy always exists, and a collapsed phase is not thermodynamically stable.

Due to rotational symmetry, the gravitational potential is easy to obtain by means of the Gauss theorem applied to the gravitational force $\mathbf{F} = -m\nabla\Phi$. The advantage of using the force over the potential, is that the potential in r depends on all the mass distribution while the force in r depends only on the mass enclosed by the disk of radius r. We find $\Phi(\mathbf{r}) = m\mathcal{G}\ln(r)$. With the use of $\int x\ln(x)\,\mathrm{d}x = \frac{x^2}{2}[\ln(x) - 1]$, the total energy (constant removed) becomes:

$$E = m\bar{v}^2 + \frac{m^2\mathcal{G}}{2}\ln(R). \tag{2.40}$$

The homogeneity is correct, but the constant removed from the logarithm gives impression that it is not. The entropy can be shown simply to be:

$$S = \ln(\bar{v}^2 R^2). \tag{2.41}$$

When removing constant terms that do not change the result once again. The Massieu function -where also terms independent of T and R have been removed- is then:

$$J = \ln(\bar{v}^2 R^2) - \beta\left[m\bar{v}^2 + \frac{m^2\mathcal{G}}{2}\ln(R)\right]. \tag{2.42}$$

We make R go to small values $R \ll 1$, it yields that the Massieu function diverges positively or negatively depending on the temperature:

$$\lim_{R\to 0} J = 2\ln(R)\left(1 - \frac{T_c}{T}\right) \quad \text{where} \quad T_c = \frac{k_B\mathcal{G}m}{4}. \tag{2.43}$$

At T_c the system changes of behavior. Below the critical temperature, J is going to ∞ as R reduces. There is no global maximum of the Massieu function, and the system is bound to undergo a collapse. It corresponds to the formation of a Dirac peak. For $T > T_c$, J goes to $-\infty$ as R reduces. There is thus a global maximum of the Massieu function and the system reaches a stable equilibrium.

We discussed above the collapse in 2D with an isotropic gravity. However, reproducing this isotropy with lasers and atoms is impossible since it would require an infinite number of lasers. As shown before, the true 2D gravity in the canonical ensemble does not display a free-energy maximum below a certain temperature: the logarithmic divergence of the potential fights on an equal footing with the logarithmic divergence of entropy. An intermediate situation is a 1D+1D configuration created by 4 lasers, which does not reproduce the logarithmic potential but has been shown numerically to display a zero-order phase transition. The collapse is possible also in the 1D+1D configuration within a certain temperature [41]. We can anticipate this phase transition by noting a main difference with the 1D case. In the 1D case, the optical thickness is almost constant, and the gravitation created is thus constant, while in 2D the optical thickness increases because of the interplay between the two dimensions. The force will thus increase up to a maximum dictated by the short-range repulsion, indicating the end of the compression. We expect thus the formation of a singularity if one had vanishing short-range repulsions. The transition has been shown numerically (see below) to be continuous and is then characterized as a zero-order phase transition. The steady state reached by the system after the maximum compression is attained, will be highly out of equilibrium because of the existence of *escape directions* at 45 degrees of the gravity axes. Along those directions, no laser beams are forbidding the atoms to escape. Therefore, in a realistic experiment, an additional harmonic trapping is added: to confine the movement of the particles and to avoid dramatic losses of the optical thickness which would ultimately lead to a decrease of the compression.

The prediction of this transition is given by the breakdown of the previous SP equation. We recall now that the SP equation can be derived by a maximum entropy production principle [45] and as such it is insightful to evaluate the time evolution of the Boltzmann entropy function $S(t) = -\int n \ln(n) dr$ with the help of the SP equation [41]. In the correctly rescaled variables, the derivative of the entropy function with the help of the SP equation gives:

$$\dot{S}(t) = -\int \nabla \cdot [n\mathbf{r} - n\mathbf{F}_G + \Theta \nabla n]\, \mathrm{d}^2 r - \int \dot{n}\, \mathrm{d}^2 r. \tag{2.44}$$

Integrating by part and using the Poisson equation for the gravitational force, yields:

$$\dot{S}(t) = -2 - 4\int n^2\, \mathrm{d}^2 r + \Theta \int \frac{|\nabla n|^2}{n}\, \mathrm{d}^2 r + \text{ boundary terms.} \tag{2.45}$$

The boundary terms are all vanishing since the density is zero at infinity. Setting $u = \sqrt{n}$ and making use of the functional inequality $\int u^4 \leq \mathcal{A} \int |\nabla u|^2 \int u^2$, we have:

$$\dot{S}(t) \geq -2 + (\Theta - \mathcal{A}) \int \frac{|\nabla n|^2}{n}\, \mathrm{d}^2 r, \tag{2.46}$$

where $\mathcal{A}$ is a constant determined numerically equal to ~ 0.171 (see [41]). We see that the time evolution of the entropy function is depending on the reduced temperature Θ only. When Θ is high enough, the Boltzmann entropy increases. This increase will stop at a given maximum, characterizing the thermodynamic equilibrium of the system. Everything is consistent with the maximum entropy principle in this case, we simply expect the system to remain extended. If however, Θ is low enough, the Boltzmann entropy may diminish without bound: which breaks the assumption on which was derived the SP equation. This breakdown characterizes a situation where no local maximum of entropy is reached and corresponds to $S(t) \to -\infty$, characterizing the formation of a Dirac peak and a "gravitational" collapse.

Let us note that in principle, the applicability of concepts such as entropy maximum, free energy minimum and H-theorems[7] [46] or even the use of the Boltzmann entropy is dangerous for self-gravitating systems: when the system collapses in three dimensions because of the singular potential, the free energy decreases *ad aeternam* and it is not compensated by the logarithmic divergence of the entropy. Thus, no minimum is reached for the free energy. Also, with the 3D potential not regularized at short distances, the partition function cannot be calculated.

Another problem [47] in using the Boltzmann entropy is that, it implicitly suggests that the equation of state of an ideal gas applies locally to the equilibrium state. We have then two problems because of the words *ideal*, *local* and *equilibrium*. Indeed, the Boltzmann entropy applies for a homogeneous fluid at a given temperature without any additional potential or forces [48]. The correct entropy function would be the Gibbs entropy which has the same form as the previous one but takes the N-particles distribution function in argument: this would be necessary to account for correlations between particles due to the force. The second problem is that, for LR forces, an equation of state cannot be defined in terms of local quantities because of the non-vanishing particles correlations. Finally, LR interacting systems are also long-lived in the absence of dissipation which makes difficult the application of equilibrium thermodynamics theorems. It seems that the Gibbs entropy is more reliable, and it indeed leads to more accurate thermodynamical variables in many cases. However, the Gibbs entropy is constant with time and cannot be used to determine the dynamical behavior of the system. Another point given supporting the usage of the Boltzmann entropy is the particularity of the Smoluchowski equation to obey automatically an H-theorem for the free energy. It is natural because to obtain this equation we assumed a constant temperature which corresponds to an equilibrium state.

We are thus in-between the justified and unjustified use of the entropy function and the "gravitational" denomination since we use explicitly the Smoluchowski formulation which by nature (1) forbids the true gravothermal collapse (in the Antonov sense [49] which involves heat currents and thus a non-homogeneous temperature) but (2) respects the H theorem in the canonical ensemble.

II.3.2 Numerical simulations

To simulate the time evolution of the system, we are interested in algorithms in the canonical ensemble. Simulating this SP equation for the density is equivalent to simulate the Langevin equations for each particle (see [41]): we are thus focusing on molecular dynamics simulations. Bruno Marcos had already designed the program for those simulations. Initially using the GADGET-2 [50] to study self-gravitating systems, he modified it to account properly for the harmonic trap and the heat bath. The initial code was modified to use a Langevin-Leapfrog algorithm, presented in

---

[7] The idea that equilibrium (finite and fixed values of the usual thermodynamic quantities) is reached at a minimum of a functional H, matching with a canonical equilibrium.

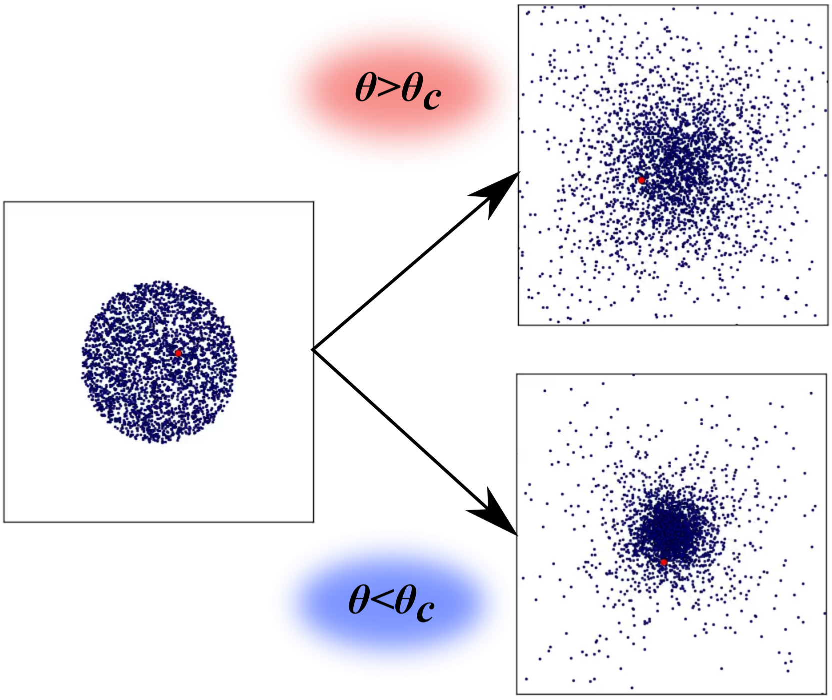

Fig. II.8 *Snapshots of the 2D distribution above and below critical temperature* θ_c*. Overdamped simulations of* $N = 1000$ *particles (blue dots).*

[51]. The algorithm uses a linked-list technique [52] to speed up the force calculation which is usually the longest in simulations. The linked list technique uses disjoint elements of memory rather than arrays that are joint memory spaces. The use of a discretized space of cell size σ and the linked-list cell algorithm allows to reduce the naive $\mathcal{O}(N^2)$ scaling of the pair interaction to a more economic $\mathcal{O}(N)$ scaling.

a) Density profiles above and below critical temperature

Figure II.8 illustrates the collapsed and extended phases observed numerically. The collapse is a zero-order phase transition (without discontinuity), thus without any brutal change in the density. However, by averaging the 2D density profile over the polar angle and looking at $\rho(r)$, one can have strong indications that the system enters a collapsed phase for low enough reduced temperature. Figure II.9 shows the different radial density profiles for a wide range of reduced temperatures. It shows results from simulations in the overdamped regime. We also varied the time-step of the algorithm and see discrepancies of the central density for reduced temperatures below 0.18. We have to take a small enough time step dt in order to remove any dependence of the numerical simulations on the critical temperature Θ_c.

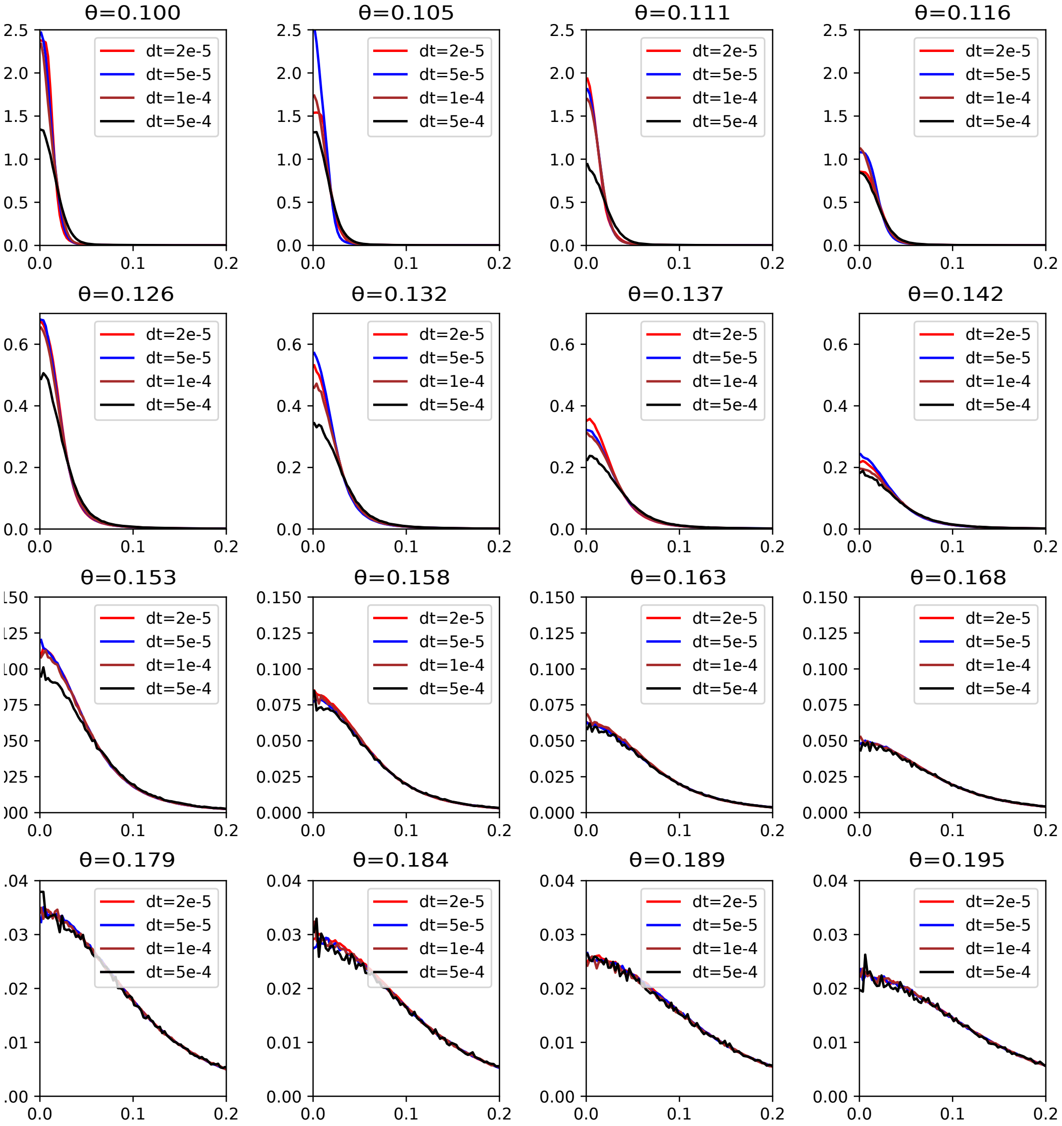

Fig. II.9 *Density vs radial position (arbitrary units) profile for* $N = 1000$ *and various time-steps (see insets). The critical temperature is visually around* $\Theta_c \approx 0.14$.

b) Time-step refinement and critical temperature Θ_c

We vary further the time-steps to have a reliable signature for collapse. Figure II.10, shows the density at $r = 0$ for various time-steps and temperatures. We notice that for small enough time-steps ($\leq 10^{-4}$), the different curves tend to match. The relevance of small time-steps appears below the collapse, when particles start spending more time next to each other. One way to take into account the dynamics of the collapse would be to vary the time steps of the integrator along the simulation. Nevertheless, by lack of time we did not implement this adaptive algorithm.

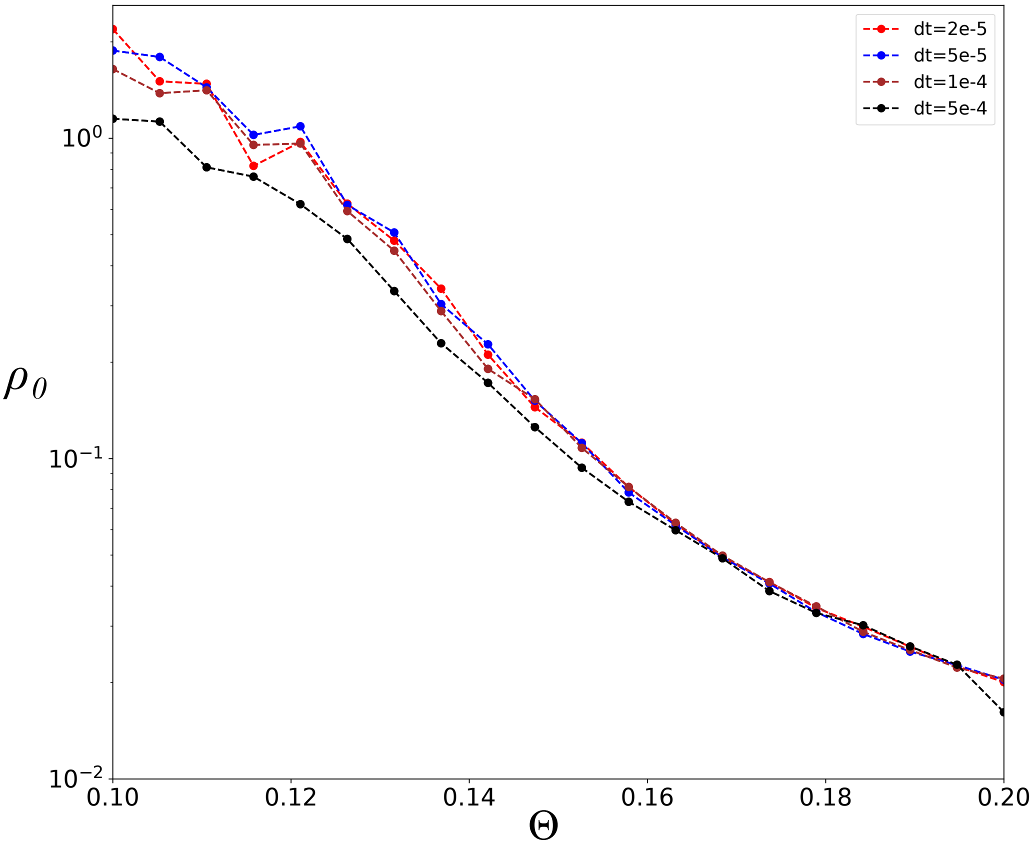

Fig. II.10 *Density at* $r = 0$ *versus reduced temperature for various time-steps. Curves are matching for* $\mathrm{dt} \leq 10^{-4}$*. Simulations made for* $N = 1000$ *particles.*

After understanding better the algorithm regarding its dependence on the time-step, we focused on the proper characterization of the collapse *i.e.* by determining the critical temperature. One way to do so is to consider the transition between extended phase and collapsed phase occurring where is the inflexion point in the density profile. For figure II.10 it corresponds to $\Theta_c \approx 0.14 - 0,15$. This critical temperature is of the same order of magnitude as the one obtained theoretically ~ 0.171 by looking at the entropy creation consecutive to the SP dynamics.
As we recovered results from previous works, we also generalized them to other situations where for instance, the two pairs of lasers are not delivering the same power.

c) Effects of $x - y$ force imbalance

In the situation where the force is not the same along x and y, for instance because of a power imbalance the laser beams, it is natural to ask whether the collapse survives. It is expected that in the extreme case of a vanishing force along one axis,

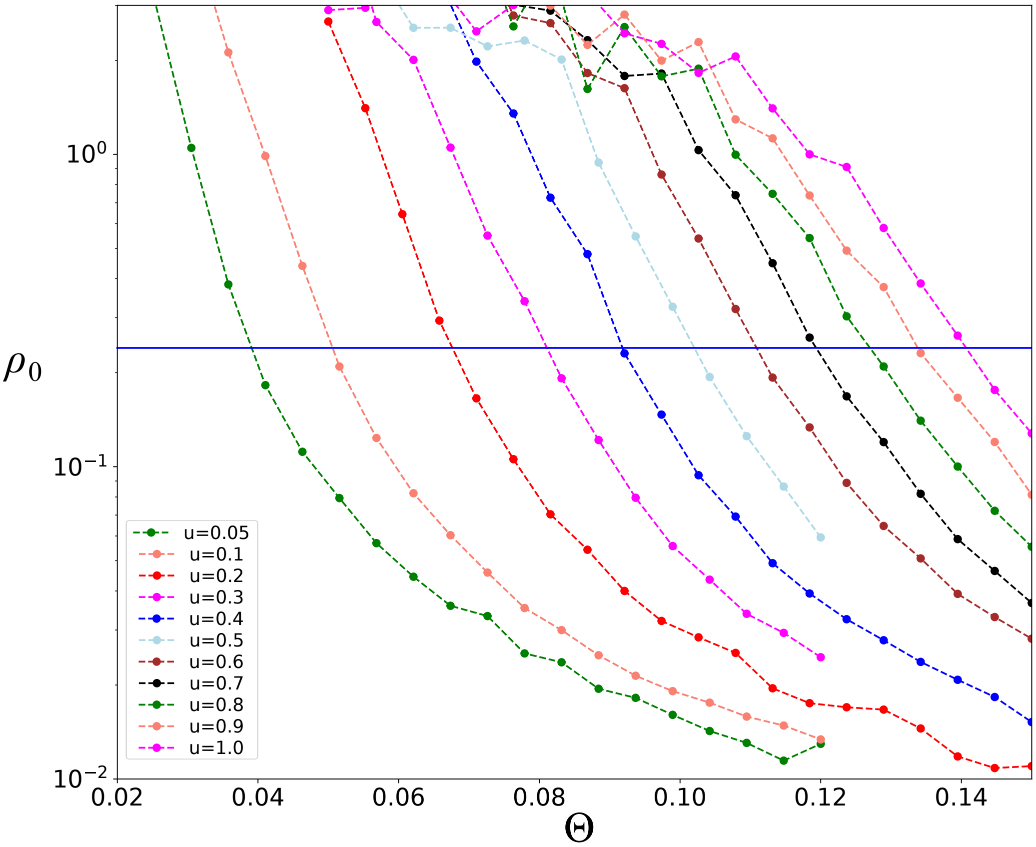

Fig. II.11 *Density versus reduced temperature for various time-steps. Curves are matching for* dt $\leq 10^{-4}$. *Simulations made for* $N = 1000$ *particles.*

one recovers the pure $1D$ gravity where no collapse is observed. The transition between $2D$ collapse and $1D$ no collapse can be observed by introducing an asymmetry parameter u controlling the ratio between the forces along x and y. Figure II.11 show how the density profile is shifting toward lower temperatures when increasing the asymmetry: when reducing the force along one direction, it requires a lower temperature to reach the same density as for equal forces. An unusual result however is the seemingly presence of the collapse at *any asymmetry parameter* $u \neq 0$ except perfect 0 which corresponds to the total extinction of the LR force along one direction. The transition between $2D$ and $1D$ seems then continuous according to the simulations, since any non-vanishing force added transversally to the $1D$ configuration will lead to a collapse at a finite temperature.

Figure II.12 shows the evolution of the critical temperature Θ_c with respect to the asymmetry parameter. Since we don't vary the number of particles within each simulation, we take the same criterion for determining Θ_c: the density of particles has to cross a fixed value represented by the blue level in Figure II.11.

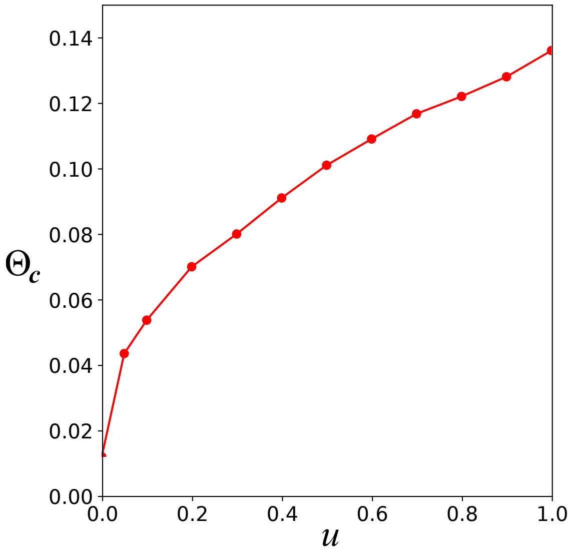

Fig. II.12 *Critical reduced temperature* Θ_c *for various* $x - y$ *force imbalance parameter* u*. Simulations made for* $N = 1000$ *particles.*

II.4 Conclusion

We gave a general introduction on long-range forces, an ill-defined group of forces with respect to standard tools in statistical physics, among which gravity belongs to. We have also recalled previously known results for two-dimensional self-gravitating systems: the existence of a phase transition in the canonical ensemble but forbidden in the microcanonical ensemble. This point alone, illustrates the inequivalence between the two ensembles for long-range forces.

We have then reminded an important result: the possibility to mimic gravity with a simple design of trapped cold atoms with pairs of contra-propagating lasers. The effect in one dimension was already observed, a small deviation from the bare Gaussian distribution from the trap and we expect to see a different behavior in two dimensions (four lasers) because of the interplay between the different directions which allows the particles to form a Dirac peak below a critical temperature or for a large enough force: in 2D the optical thickness increases because of the feedback between the different directions, while in 1D the optical thickness is constant and forbids a collapse.

The numerical simulations, reinforcing the possibility of observing a collapse in 2D were reproduced and extended to asymmetric cases. In conclusion, the transition resists asymmetry between the $x - y$ imbalances but is difficult to localize because of its smoothness. The presence of a small confining potential has also been considered. First, to give the atomic cloud its right shape (1D, 2D etc.) and secondly to reduce atomic losses in the directions where the artificial gravity is absent. Beyond the standard collapse where the 4 gravitational beams are at 90° from each other, we will also question the importance on the number of beams and their angle in Chapter V, it is another matter of importance to be addressed experimentally.

The Smoluchowski-Poisson equation derived previously is the reminiscence of the Keller-Segel model [53] in two dimensions that describes the dynamics of bacterial colonies and biological cells. Bacteria leave chemical behind them, that other bacteria are attracted by. When the bacterial population exceeds some critical value, the whole system collapses in a finite time (see *e.g.* [54]). The originality of the previous model is more striking than simply recovering the predictions of Keller-Segel equations. It is indeed possible to collapse the system only with a 4 crossed beam configuration that breaks the rotation symmetry of the real 2D gravity. The present model 2D artificial gravity is thus simpler to realize experimentally and still encapsulates the finite-time collapse. It was realized by J. Barré *et al.* [41] and is at the origin of the thesis project. Right now, we are concerned by the realism of our model and wish to go one step beyond. We will start by considering undesirable effects -such as the finite temperature effects and photon spontaneous emission- that will work against the gravitational collapse in the next chapter.

Chapter III

Model refinement and design of the experiment

Anticipating on the experiment, we compute some predictions of the model developed in Chapter II Section II.3 to a more realistic case. We start by restoring the temperature effects that were not considered in the derivation of the gravitational force in Section III.1. Then we address the effects of the next scattering events: spontaneous emission followed by re-absorption (multiple scattering). The photons creating the gravitational force are absorbed photons that will finally be re-emitted. The multiple scattering is the process by which a spontaneously re-emitted photon is reabsorbed by another atom. It leads then to unwanted repulsion between atoms, going opposite to the collapse dynamics. We expect thus the multiple scattering to be responsible for a lowering of the critical temperature. The effects of multiple scattering are discussed in III.2. Finally, the design of the optical dipole trap geometry and wavelength is presented in III.3.

III.1 Finite temperature effect

The finite atom temperature during the experiment has the effect of broadening the spectral lines (Doppler broadening). For the transition on which the long-range (LR) force is acting, the broadening is important since the bare linewidth Γ is narrow, we have indeed a Doppler broadening about $k\bar{v} \approx 3\Gamma$, so that the spectral line is three times larger than at zero temperature. A broad transition would have a much smaller Doppler broadening such that $k\bar{v} \ll \Gamma$. Thus, effects of the finite temperature are important and should be accounted for in the model. The transition is expected to appear at a critical reduced temperature $\Theta \approx 0.13$ [41], as indicated by the theoretical analysis in II Section II.3 and the numerical simulations realized in Chapter II Section II.3.2. We recall that in the derivation of the force, the Doppler effect is neglected and thus $\mathbf{F}_G$ does not depend on the velocity. The reduced temperature Θ depends on the real temperature T and the typical energy C of the LR force. There are then two ways to probe the collapse transition: changing the temperature, the detuning or the intensity. To locate more precisely the parameters for which the transition occurs, we start accounting for more undesirable effects that we neglected initially. The temperature of the atom is the first and we recall, the 2D shape is given to the system of atoms by using an optical dipole trap of very large horizontal dimensions $\sigma_x = \sigma_y$ and of small vertical dimension σ_z. To restore velocity effects on the atoms absorption we do the following substitution:

$$\frac{1}{\Gamma^2 + 4\delta^2} \quad \to \quad \int_{\mathbb{R}} g(v) \frac{1}{\Gamma^2 + 4(\delta - kv)^2} dv \tag{3.1}$$

with the usual thermal velocity $\bar{v} = \sqrt{\frac{k_B T}{m}}$. We recognize the expression given by Equation 2.9, except that we are only restoring afterward this velocity dependence[1]. We find after calculation, the following replacement for the bare Lorentzian lineshape:

$$\boxed{\frac{1}{\Gamma^2 + 4\delta^2} \quad \to \quad \frac{1}{2\Gamma}\sqrt{\frac{\pi}{2}}\frac{1}{k\bar{v}}\mathrm{Re}\left(\mathcal{F}\left[\frac{\delta + i\Gamma/2}{k\bar{v}\sqrt{2}}\right]\right)} \tag{3.2}$$

Where $\mathcal{F}(x)$ is the Faddeeva function [55] defined by

$$\mathcal{F}(x) = e^{-x^2}\mathrm{erfc}(-ix) = \frac{i}{\pi}\int_{\mathbb{R}} \frac{e^{-t^2}}{x - t} dt \tag{3.3}$$

Using $\sigma_0 = 6\pi/k^2$, the 2D typical energy given by Equation 2.25 becomes

$$\boxed{C = \frac{3\hbar\Gamma^3 N \pi^{3/2}}{8\sqrt{2}k^3\bar{v}^2\sigma_z} s_0 \mathrm{Re}\left(\mathcal{F}\left[\frac{\delta + i\Gamma/2}{k\bar{v}\sqrt{2}}\right]\right)^2} \tag{3.4}$$

The finite temperature has the effect of reducing C as compared to the zero-temperature case. To compensate this decrease we have either to increase the laser intensity or use lasers closer to resonance. Also, a useful expansion of the Faddeeva function exists at large detuning, supposing that $|k\bar{v}|, \Gamma \ll |\delta|$, we found up to second-order and after integration:

$$\int_{\mathbb{R}} \frac{g(v)}{\Gamma^2 + 4(\delta - kv)^2} dv \approx \frac{1}{4\delta^2}\left(1 + 3\left(\frac{k\bar{v}}{\delta}\right)^2\right) \tag{3.5}$$

Thanks to the previous expressions that account for the finite temperature on the 2D force typical energy, we can extract the critical detuning δ_c at a given saturation parameter s_0, number of atoms N and temperature T that corresponds to the critical reduced temperature $\Theta_c \approx 0.125$. Like this, we reduce the range for the

---

[1] To be completely correct we should have carried it all along since the beginning, but it would have made the formulas not tractable.

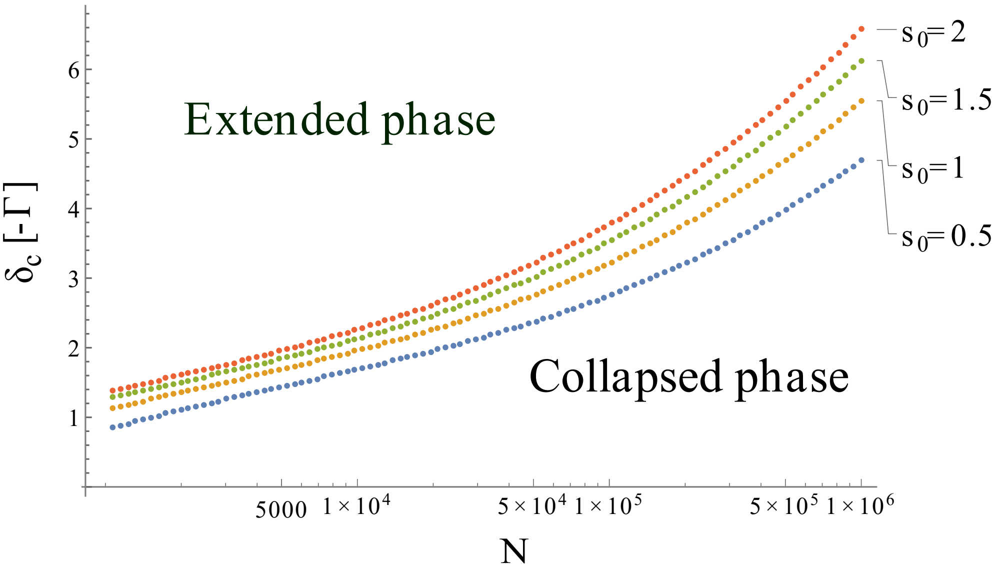

Fig. III.1 *Critical detuning dependency on the number of atoms N and the saturation parameter s_0 after restoring the finite temperature effects in the 2D gravity typical energy C. The critical line goes up for larger intensities and down for larger temperatures (not represented).*

detunings that we must set our lasers to see the gravitational collapse. Figure III.1 shows the critical detuning for $s_0 = 0.5, 1, 1.5, 2$ and various number of atoms. For all those curves we supposed having a fixed trap giving a cloud of initial RMS of $\sigma_x = \sigma_y = 250$ μm and $\sigma_z = 10$ μm. We see that the critical line does not change significantly with the saturation parameter but depends strongly on the number of atoms. Reducing the number of atoms requires to put the laser closer to resonance and brings the system in an unstable state. Reasonable critical detunings are then $\delta \approx [-4\Gamma, -2\Gamma]$. Along with the critical detuning, the optical thickness along one laser may also be computed in a similar fashion if we make the approximation of an isotropic compression. The optical thickness is then:

$$b = \frac{3\sqrt{\pi}N\Gamma}{2^{3/2}k^3\bar{v}\sigma_x\sigma_y}\mathrm{Re}\left(\mathcal{F}\left[\frac{\delta + i\Gamma/2}{k\bar{v}\sqrt{2}}\right]\right) \tag{3.6}$$

With this formula, it is possible to calculate approximately the compression factor CF defined as the ratio of the initial and final RMS of the atomic cloud during compression. To compute those initial and final RMS we remember the approximation made in the derivation of the force, namely $b \ll 1$. To be understood, the optical thickness is low enough to allow compression. Due to the compression, b increases as the cloud RMS reduces because $b \propto \mathrm{CF}^2$ since the compression is two-dimensional. This compression stops supposedly when the cloud is so dense that the light cannot enter the medium: typically, when $b \approx 1$. Within those criteria, supposing an initial RMS of 250 μm, number of atoms about $N = 3 \times 10^5$, a detuning of $\delta = -3\Gamma$ and a temperature of $T = 1\ \mu$K, the optical thickness is about 0.1. The compression factors are then typically of three, which is larger than the compression factors obtained for the 1D artificial gravity experiments with strontium [28] of only of 1.5 at best. We thus expect much stronger compressions than for the 1D gravity

With those high compression factors, we are encouraged to compute another interesting quantity: the phase-space density. This quantity is important to characterize the appearance of quantum degeneracy effects in cold atoms experiments (see e.g. [56]). It is written $n\lambda_{dB}^3$ where λ_{dB} is the de Broglie thermal wavelength. We extrapolated from our model a final phase-space density about 0.3, which is below the threshold of degeneracy effects at 2.6. It is nevertheless high enough to be mentioned, since it involves only laser cooling. All those values seem promising, but we forgot an important effect that might displace significantly the critical temperature: the random re-emission the photons creating the artificial gravity and that will heat up the cloud, this is the subject of the next section.

III.2 Multiple scattering

III.2.1 First event approximation of multiple scattering

When an atom absorbs one photon from the laser, the excited state has a particular angular momentum - for us $J_e = 1$ - and will re-emit light in a favored direction [57] following a defined radiation pattern. The frequency of the re-emitted photon is either equal (elastic scattering) or different (inelastic scattering) from the absorbed one. In the case of intense laser excitations, it is known that the emission spectrum splits in three and forms a Mollow triplet [31]. However, we work at low intensity and the re-emitted photons are supposedly at the same frequency. They thus have a high probability of being re-absorbed which induces another force -repulsive- going against the artificial gravity. It is necessary to choose the proper polarization and atomic cloud characteristics to minimize the effect of this multiple scattering or it might impede the gravitational collapse.

An atom excited by a component of the electric field of polarization $\boldsymbol{\epsilon}$ will re-emit a fluorescence photon by spontaneous emission according to the following angular-distribution function [58] :

$$\mathcal{R}(\theta, \phi, \boldsymbol{\epsilon}) = \frac{3}{8\pi}\left(1 - |\hat{r} \cdot \boldsymbol{\epsilon}|^2\right). \tag{3.7}$$

We note that for a linear polarization along $\hat{z}$ the radiation pattern is maximum in the plane orthogonal to the induced dipole and zero along it as shown in Figure III.2. While for a circularly polarized photons (quantization axis along $\hat{z}$ as defined in the circular basis $\{\mathbf{e}_0, \mathbf{e}_+, \mathbf{e}_-\}$) they are non-zero everywhere:

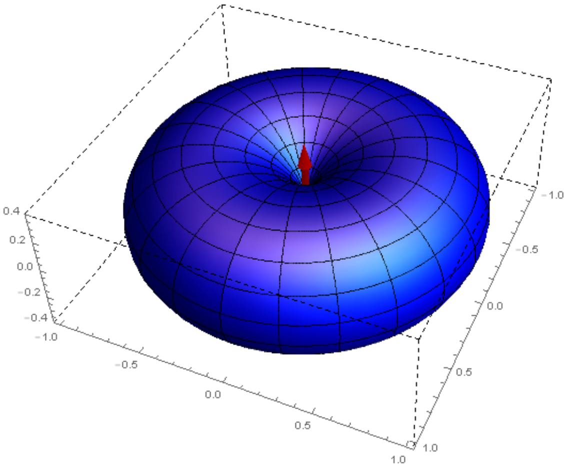

Fig. III.2 *Linear dipole (red arrow) radiation pattern. Most of the power radiated is send orthogonally to the dipole.*

$$\mathcal{R}(\theta,\phi,\mathbf{e}_0) = \frac{3}{8\pi}\sin^2(\theta), \tag{3.8}$$

$$\mathcal{R}(\theta,\phi,\mathbf{e}_\pm) = \frac{3}{16\pi}(1+\cos^2(\theta)). \tag{3.9}$$

We consider shining a laser of polarization $\boldsymbol{\epsilon}$ over an atom, following an absorption the re-emitted photon is possibly re-absorbed by *another* atom, we speak of multiple scattering [59]. The re-absorption probability -with the constraint that the power radiated is constant- is

$$\mathcal{R}(\theta,\phi,\boldsymbol{\epsilon})\frac{\sigma_R}{|\mathbf{r}-\mathbf{r}'|^2}, \tag{3.10}$$

where σ_R is the re-absorption cross section and $|\mathbf{r}-\mathbf{r}'|$ the distance between the atom emitting the photon and the one receiving it. The angular coordinates denote now the ones of the $\mathbf{r}-\mathbf{r}'$. This re-absorption yields a kick and the receiver will acquire a recoil momentum $\hbar\mathbf{k}$ at most $\frac{\Gamma}{2}s_0$ times per second if the laser is resonant. The single-laser multiple scattering force between two atoms will then be

$$\hbar k\frac{\Gamma}{2}s_0\mathcal{R}(\theta,\phi,\boldsymbol{\epsilon})\chi\sigma_0\frac{\mathbf{r}-\mathbf{r}'}{|\mathbf{r}-\mathbf{r}'|^3}, \tag{3.11}$$

where χ accounts for the difference between the absorption scattering cross-section and the re-absorption cross-section. The computation of this factor can be quite complicated (see *e.g.* [31]) and is supposed to be close to 1 since only the elastic scattering contributes (only low saturation used here). The multiple scattering is then in first approximation a Coulombian interaction. If the cloud of atoms is described by the density $n(\mathbf{r})$ over a volume $\mathcal{V}$ and choose the polarization linear in the plane for each of the four beams creating the artificial gravity, we will most likely re-emit photons out of the atomic cloud. Since each beam is characterized by the same saturation parameter s_0 (the same intensity) and that orthogonal directions don't interfere, the four linearly polarized beams give a multiple scattering force in the volume $\mathcal{V}$ equal to:

$$\boxed{\mathbf{F}_{\mathrm{M}}(\mathbf{r}) = \hbar k \frac{\Gamma}{2} 4 s_0 \chi \sigma_0 \frac{3}{16\pi} \int_{\mathcal{V}} \frac{\mathcal{R}(\theta', \phi', \boldsymbol{e}_x) + \mathcal{R}(\theta', \phi', \boldsymbol{e}_y)}{2} \frac{\mathbf{r} - \mathbf{r}'}{|\mathbf{r} - \mathbf{r}'|^3} n(\mathbf{r}') d^3 r'.} \tag{3.12}$$

Here, we approximate the radiation pattern as the mean of two linear ones, which will set a upper bound on the multiple scattering force. It is because replacing the saturation parameter by four times its value is not completely true as the contra-propagating beams will interfere. Hence, the intensity should be modulated in plane to account for this interference. We are however only interested in deriving an order of magnitude of this multiple scattering versus the artificial gravity. The effect of interferences is to create a dipole potential (optical lattice) and will be particularly important when the saturation parameter becomes large [60], otherwise the atoms will fly over the details of the light potential and will wash out the effect of interferences. We discuss briefly the effects of those light potentials in Appendix A, where we consider different beam configurations and look for low intensities how the velocity distribution is modified. We found no quantitative modifications depending on the beam configuration and recovered the semi-classical result that at large detuning the temperature scales linearly with the saturation parameter. The reason why we found the semi-classical result even if we work use the narrow intercombination line is that we work at large detuning which avoid us a fully quantum treatment as derived in [39]. This last reference also shows that the semi-classical limit is recovered at large detuning.

III.2.2 Relative strength between multiple scattering and gravitational force

We simplify the system to be an ellipsoid of constant density n_0. The artificial gravity in 2D given by Equation 2.24 takes the simple form

$$\boxed{\mathbf{F}_{2D}(\mathbf{r}) = -\hbar k \frac{\Gamma}{2} s_0 \frac{\sigma_0 n_0}{(1 + 4(\delta/\Gamma)^2)^2} \left(x\mathbf{e}_x + y\mathbf{e}_y \right).} \tag{3.13}$$

We can now compute the ratio between the multiple scattering and 2D gravity forces over the ellipsoid volume:

$$\mathcal{V} = \{(x, y, z)\ ,\ \frac{x^2}{\sigma_x^2} + \frac{y^2}{\sigma_y^2} + \frac{z^2}{\sigma_z^2} \leq 1\}. \tag{3.14}$$

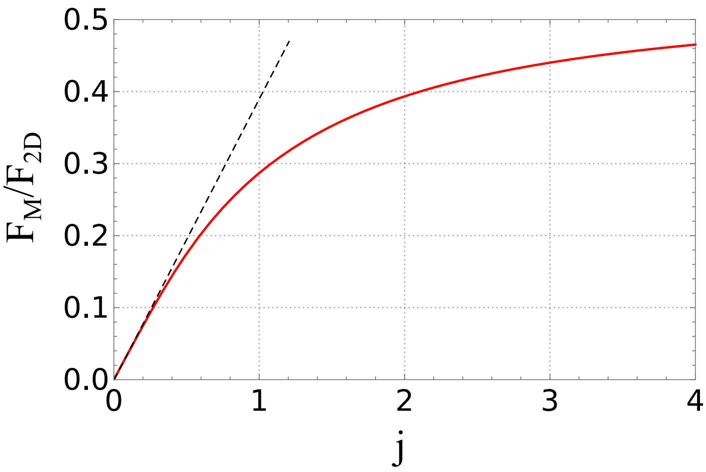

Fig. III.3 *(red continuous) Ratio between multiple scattering and 2D gravity for an atom at* $(1, 0, 0)$ *and a ellipsoid aspect ratio* j*. (black dashed) Linear behavior at* $j \to 0$*.*

The ratio of the two forces modulus is calculated inside this volume, where a rescaling is performed to express the integral in Equation 3.12 in terms of $j = \sigma_x/\sigma_z$ (or identically σ_y/σ_z) the ellipsoid aspect ratio. The most extreme situation being for atoms located at $(0, 0, \pm 1)$, where the artificial gravity is zero and only the multiple scattering is acting on the atoms, pushing them away vertically. This pathological case is one of the reasons why we need a strong vertical confinement, to contain the atoms that would otherwise leave the system. We are rather interested here into the $(1, 0, 0)$ position where the multiple scattering is maximum and the 2D gravity as well, it will be a good position to test the relative strength between the two forces.

The integration is performed numerically and the $1/|\mathbf{r} - \mathbf{r}'|^2$ divergence is regularized by adding a small real part to the denominator. We are especially interested in the high aspect ratio $j \to 0$. We plot along a larger span to verify the opposite situation where the aspect ratio is $j \gg 1$ and that the ratio of the two forces becomes constant. Indeed, the contribution of the multiple scattering becomes constant as the cloud is expanded along $\hat{z}$: it is similar to calculate the Coulombian force generated by an infinitely long wire of constant linear charge.

Figure III.3 shows the ratio between multiple scattering and the 2D gravity, the ratio becomes negligible, *i.e.* $F_M/F_{2D} \ll 1$, when the inverse aspect ratio is $j^{-1} \approx 10 - 20$. For a cloud of in-plane RMS of 150 μm, it would correspond to a cloud thickness of roughly 10 μm. It is small, but accessible to our optical setup.

III.3 Design of the 2D dipole trap

III.3.1 Trap losses

The main characteristics of a good trap are its loading rate and lifetime, the latest depending on atom losses. In perfect vacuum, losses arise from collisions between at least two objects: an atom with either other atoms or photons. We have only ^{88}Sr present in our trap because of the isotope shift[2] between the different Bosonic species. Different scattering processes are listed (not all) below and their importance for ^{88}Sr is discussed.

- **Atom** $|g\rangle$ + **Atom** $|g\rangle$: Scattering between two strontium atoms in the ground state are described by the scattering length which for our main isotope ^{88}Sr is nearly zero (see table IV.2). It can be disregarded.
- **Atom** $|g\rangle$ + **Atom** $|g\rangle$ + **Atom** $|g\rangle$ Three-body scattering occurs only at extremely high densities (see *e.g.* [61]) and can be disregarded.
- **Atom + Atom + photon** Such as photo-association. See [62] in general and for Sr^{88} excited molecules (not stable) see [63, 64]. For photo-association on the inter-combination line of alkaline earth metals see [65, 66]. They occur at frequencies far from the one we are working with and can be disregarded.

Another point not mentioned previously is the heating due to the ODT beam absorption and spontaneous emission. It is not a problem in our case since the trap depth depends on I/δ while the spontaneous emission rate depends on I/δ^2 (see e.g. [67]), it is then possible to reduce heating from the dipole trap beam to a minimum by increasing the detuning enough. The lifetime of the atoms in the ODT has been measured to be of a minute or more for the ^{88}Sr, which indicates that no substantial heating originates directly from the atom-ODT interaction.

III.3.2 Dipolar trapping on the strontium-88 intercombination line

As it will be detailed in the next paragraphs, the dipole trapping potentials (light shifts) are not the same in the excited state and ground state. They can be made equal for some magical wavelength [68] of the dipole laser. We propose to calculate and measure the magical wavelength that cancels the differential light shift of the $^1\mathrm{S}_0(m=0)\rightarrow{}^3\mathrm{P}_1(m=\pm1)$ intercombination line, transition used to drive the 2D artificial gravity. As such, we will ensure that the 2D gravity is the same independently of the atoms position in the dipole trap. The method to calculate this wavelength is identical to the one explained in [69].

---

[2] The ^{87}Sr blue resonance is shifted of ~ -50 MHz from the ^{88}Sr resonance. The ^{86}Sr blue resonance is shifted ~ -100 MHz from the ^{88}Sr resonance. We consider then our blue MOT loaded with one species and by extension the ODT too.

a) Beam polarizations

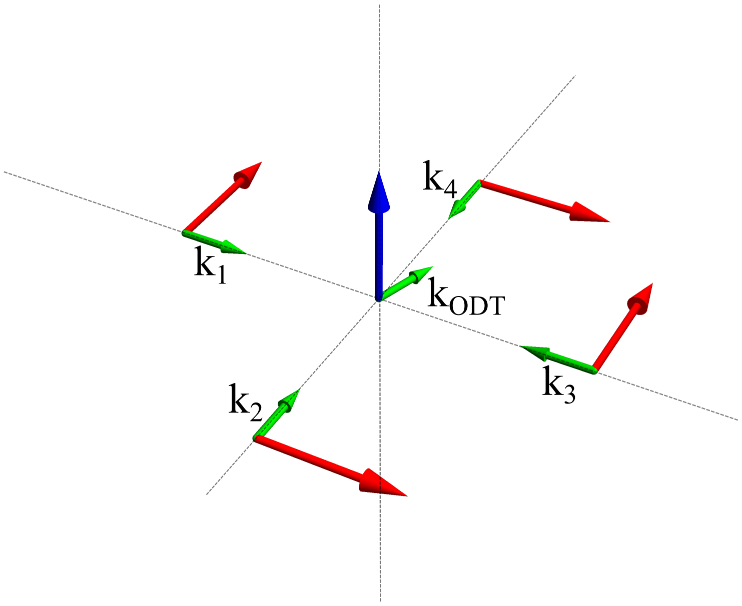

Fig. III.4 *Polarizations of the different beams to account in the light shift calculation. (blue) Dipole trap polarization. (red) 2D gravity beam polarizations. (green) wave vectors. The three gray lines are orthogonal. The ODT wave vector 14 ° away from one of the 2D gravity axis (given by k_2 and k_4).*

The dipole trap laser polarization will determine the light shift and since we already constrained the artificial gravity to have a linear polarization in-plane to reduce the multiple scattering, there is only one choice possible for the polarization of our dipole trap: linear out of the plane as depicted in Figure III.4. As represented on the figure, the ODT wave-vector is not aligned with the 2D gravity axes but differ from 14° from one of them, it comes from setup constraints.

b) Light shifts

While shining a far-detuned light on an atom, the electron tends to follow the local electric field oscillations. The electron is driven at the frequency of the light resulting in an electric dipole $\mathbf{p}(\mathbf{r})$ proportional to the local electric field $\mathbf{E}(\mathbf{r})$. The proportionality factor is the complex polarizability α. As the atom is in a particular state $|i\rangle$, its response may change, and the complex polarizability should be written more generally $\alpha_i(w_L, \boldsymbol{\epsilon})$ to account for the electric field polarization. The potential experienced by the atom in the state $|i\rangle$ is known as the light shift or light displacement:

$$U_i(\mathbf{r}) = -\frac{1}{2}\left\langle \mathbf{p}(\mathbf{r})\cdot\mathbf{E}(\mathbf{r})\right\rangle = -\frac{1}{2}\mathrm{Re}(\alpha_i(w_L,\boldsymbol{\epsilon}))|\mathbf{E}(\mathbf{r})|^2, \tag{3.15}$$

all the geometric and energetic details are contained in the complex polarizability coefficient and the biggest trouble is to access this quantity for the states of interest. The usual way to determine the different polarizabilities is to relate them to the strength of optical transitions [70]. It is then possible to first relate the polarizability to the dipole matrix elements using time-dependent perturbation theory [37]:

$$\mathrm{Re}(\alpha_i(w_L,\boldsymbol{\epsilon})) = \frac{e^2}{\hbar}\sum_{j\neq i}\mathrm{Re}\left(\frac{|\left\langle j\right|\hat{\mathbf{r}}\cdot\boldsymbol{\epsilon}\left|i\right\rangle|^2}{\omega_{ji}-\omega_L-i\Gamma_{ji}/2}+\frac{|\left\langle i\right|\hat{\mathbf{r}}\cdot\boldsymbol{\epsilon}\left|j\right\rangle|^2}{\omega_{ji}+\omega_L+i\Gamma_{ji}/2}\right) \tag{3.16}$$

Where, assuming a large detuning compare to the decay rate between states j and i $|\delta| \gg \gamma_{ji}$ yields:

$$\boxed{\mathrm{Re}(\alpha_i(w_L,\boldsymbol{\epsilon})) = \frac{2e^2}{\hbar}\sum_{j\neq i}\frac{\omega_{ji}|\left\langle j\right|\hat{\mathbf{r}}\cdot\boldsymbol{\epsilon}\left|i\right\rangle|^2}{\omega_{ji}^2-\omega_L^2}.} \tag{3.17}$$

Although we discarded the transition rates $\{\Gamma_{ji}\}$ from the previous expression, they however have a strong role to play in the calculation of the polarizability. Indeed, it is known [71] that the transition rate between a single excited state couple by vacuum fluctuations to its ground state is given by the Weisskopf-Wigner formula:

$$\Gamma_{ge} = \frac{\omega_{eg}^3}{3\pi\epsilon_0\hbar c^3}|\langle e|\,|\hat{\mathbf{d}}|\,|g\rangle|^2. \tag{3.18}$$

This rate is simply written Γ for the two-level atom. The matrix element is known as the reduced-dipole element. It encapsulates no geometry since the vacuum is isotropic. If however, we consider a set of degenerate states and break the isotropy by imprinting an electric dipole with an external field [58] the spontaneous emission rate between two sub-levels should include this loss of symmetry:

$$\Gamma_{J_g,m_g;J_e,m_e}(\boldsymbol{\epsilon}) = \frac{\omega_0^3}{3\pi\epsilon_0\hbar c^3}|\left\langle J_e,m_e\right|\hat{\mathbf{d}}\cdot\boldsymbol{\epsilon}\left|J_g,m_g\right\rangle|^2. \tag{3.19}$$

It is convenient to make use again of the spherical basis $\{\mathbf{e}_0,\mathbf{e}_+,\mathbf{e}_-\}$, in which electric-dipole transitions are written more easily. The dipole operator may now be decomposed as:

$$\hat{\mathbf{d}} = \sum_q \hat{d}_q\mathbf{e}_q^*. \tag{3.20}$$

This allows the use of the Wigner-Eckart theorem [72] to obtain the transition rate:

$$\Gamma_{J_g,m_g;J_e,m_e}(\boldsymbol{\epsilon}) = \frac{\omega_0^3}{3\pi\epsilon_0\hbar c^3} \langle J_e, m_e| \hat{d}_q |J_g, m_g\rangle |^2 \tag{3.21}$$

$$= \Gamma_{J_g,J_e} \frac{2J_g+1}{2J_e+1} | \langle J_e, m_e | J_g, m_g; 1, q\rangle |^2. \tag{3.22}$$

The total rate between two fine structure manifolds $J_e,\ J_g$ is modified to take into account the degeneracy (first term) and the pumping by the laser (second term). Since the total transition rate Γ_{J_g,J_e} is usually the only quantity available in the literature, we are left with a set of Clebsch-Gordan coefficients to compute:

$$\langle J_e, m_e | J_g, m_g; 1, q\rangle\ . \tag{3.23}$$

In the end, the polarizability (real part) becomes a function of the transition rates:

$$\mathrm{Re}(\alpha_i(w_L, \boldsymbol{\epsilon})) = 6\pi\epsilon_0 c^3 \sum_{j\neq i} \frac{\Gamma_{ji}(\boldsymbol{\epsilon})}{\omega_{ji}^2(\omega_{ji}^2 - \omega_L^2)}. \tag{3.24}$$

The Γ_{ji} can be re-written as:

$$\Gamma_{ji}(\boldsymbol{\epsilon}) = \zeta_{ji} \frac{\Gamma_{J_j,m_j;J_i,m_i}(\boldsymbol{\epsilon})}{\Gamma_{J_j,J_i}} \Gamma_{J_j,J_i}. \tag{3.25}$$

The ζ_{ji} are a set of empirical correction factors which account for the deviation from the idealized dipole behavior of the electron. Especially in the s states, where the electron travels close to the nucleus, which deviates from the image of an electric dipole of well separated charges.

The interaction of a multi-level atom with an electrical field of a given polarization leads to energy shifts of the different levels, it is known as the Stark effect. When the intensity and detuning is high enough, the dispersive atom-light interaction is almost conservative and perturbation theory yields the expression of a dipole potential in which the atom will evolve. Since this potential is proportional to the electric field intensity, the force experienced by the atom is proportional to the gradient of the intensity. We need to introduce the correct description for a laser intensity to derive the dipolar force associated.

We emphasize the fact that the dipole force is non-negligible for the dipole trap (the trapping of our model) but negligible when coming from the artificial gravity beams interferences as explained in Appendix A, it is important to not confuse the two.

c) Magical wavelength configuration

A magic wavelength configuration [68] -if it exists- is particularly useful for several reasons. The atomic frequency being independent of the position in the trap and laser cooling can be performed. Even better, absorption spectroscopy and fluorescence imaging can be ran inside the trap, which gives access to many physical quantities, such as the optical thickness.

Calculation of the magical wavelength for the $^1\mathrm{S}_0 \rightarrow {}^3\mathrm{P}_1$ $(m = \pm 1)$ transition in a linearly polarized ODT is given below. We found $\lambda_M = 925$ nm. This near infrared wavelength is accessible with tunable Ti:Sapphire laser (see Chapter IV Section IV.3.3 for technical details).

As expressed by Equation 3.15 the light shift for a state $|i\rangle$ is going to be proportional to the intensity of the electric field. Also, we wish to create a 2D cloud of atom, what is the intensity profile of our ODT laser? The fundamental mode of a laser is called TEM_{00}, for more details we can refer to [73]. The zero (Gaussian) mode is the main contribution of standard lasers, the quality of this mode being measured by the M^2 factor. The M^2 factor is defined as $M^2 = \pi w_0^2 \theta / \lambda$ where θ is the half-angle beam divergence and w_0 the beam radius. A Gaussian beam has a M^2 factor of 1 and any other mode has a larger factor. Our ODT laser has a M^2 factor of less than 1.1. It is a reasonable approximation to consider the mode to be perfectly Gaussian. The 2D shape is given to our cloud by taking a strongly elliptical Gaussian beam propagating along $\hat{y}$:

$$E(\mathbf{r}) = E_0 \sqrt{\frac{w_{0x} w_{0z}}{w_x(y) w_z(y)}} \exp\left(-\frac{x^2}{w_x(y)^2} - \frac{z^2}{w_z(y)^2} - i\Phi \right), \tag{3.26}$$

where Φ is the Gouy phase and for $i = \{x, z\}$ the different waists are $w_i = w_{0i}\sqrt{1 + (z/z_{Ri})^2}$. The Rayleigh lengths are $z_{Ri} = \pi w_{0i}^2/\lambda$. Expanding to second-order the previous expression we find that the potential is harmonic close to the origin (Figure III.5) and we can easily identify the trap depth

$$U_i(\mathbf{0}) = \mathrm{Re}(\alpha_i(w_L, \boldsymbol{\epsilon})) \frac{E_0^2}{2}, \tag{3.27}$$

and trap frequencies

$$\omega_x = \sqrt{\frac{4U_i(\mathbf{0})}{m{w_{0x}}^2}} \qquad \omega_z = \sqrt{\frac{4U_i(\mathbf{0})}{m{w_{0z}}^2}} \qquad \omega_y = \sqrt{\frac{U_i(\mathbf{0})}{m} \left(\frac{1}{{z_{Rx}}^2} + \frac{1}{{z_{Rz}}^2} \right)}. \tag{3.28}$$

The trapping potential takes then the simpler form:

$$U_i(\mathbf{r}) = -U_i(\mathbf{0}) + \frac{m\omega_z^2}{2} z^2 + \frac{m\omega_x^2}{2} x^2 + \frac{m\omega_y^2}{2} y^2. \tag{3.29}$$

By application of the equipartition theorem, we relate those frequencies to temperature of an ensemble of non-interacting atoms harmonically trapped:

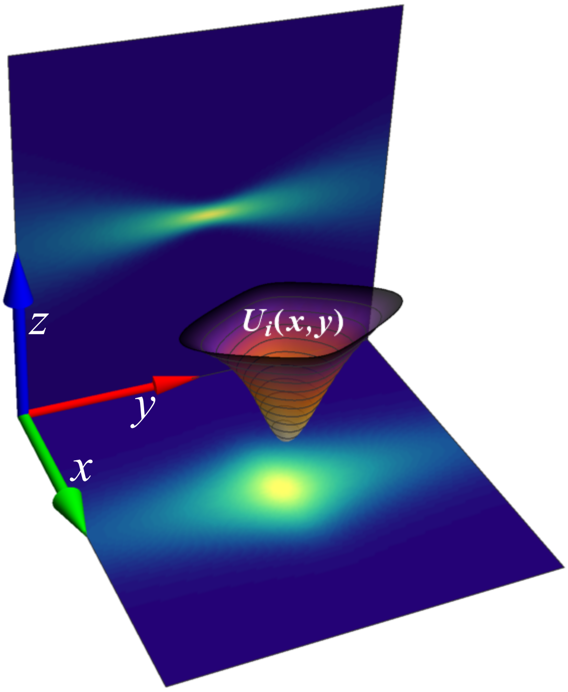

Fig. III.5 *Focused elliptical Gaussian beam propagating along the red arrow. Projections of the light intensity and associated Dipole potential $U_i(x, y)$. The trap is deep vertically and looser horizontally, hence two dimensional.*

$$\frac{k_B T}{2} = \frac{m\omega_z^2}{2}\left\langle z^2\right\rangle = \frac{m\omega_x^2}{2}\left\langle x^2\right\rangle = \frac{m\omega_y^2}{2}\left\langle y^2\right\rangle . \tag{3.30}$$

If we wish to express the trap frequencies as a function of the saturation parameter, the previous trap depth written as function of E_0 is satisfying. However, a slightly more convenient formula for the trap frequencies include the power of the laser rather than the electric field intensity:

$$I(\mathbf{r}) = \frac{c\epsilon_0}{2}|E(\mathbf{r})|^2. \tag{3.31}$$

The power is also related to the intensity and the waists obtained by transverse integration of the intensity function:

$$P = I_0\frac{\pi}{2}w_{0x}w_{0z}. \tag{3.32}$$

Then the electric field amplitude is:

$$E_0 = \sqrt{\frac{4P}{\pi w_{0x}w_{0z}c\epsilon_0}}, \tag{3.33}$$

and the trap depth

$$U_i(\mathbf{0}) = \frac{2\mathrm{Re}(\alpha_i)P}{\pi w_{0x} w_{0z} c\epsilon_0}. \tag{3.34}$$

d) Magical wavelength calculation and measurement

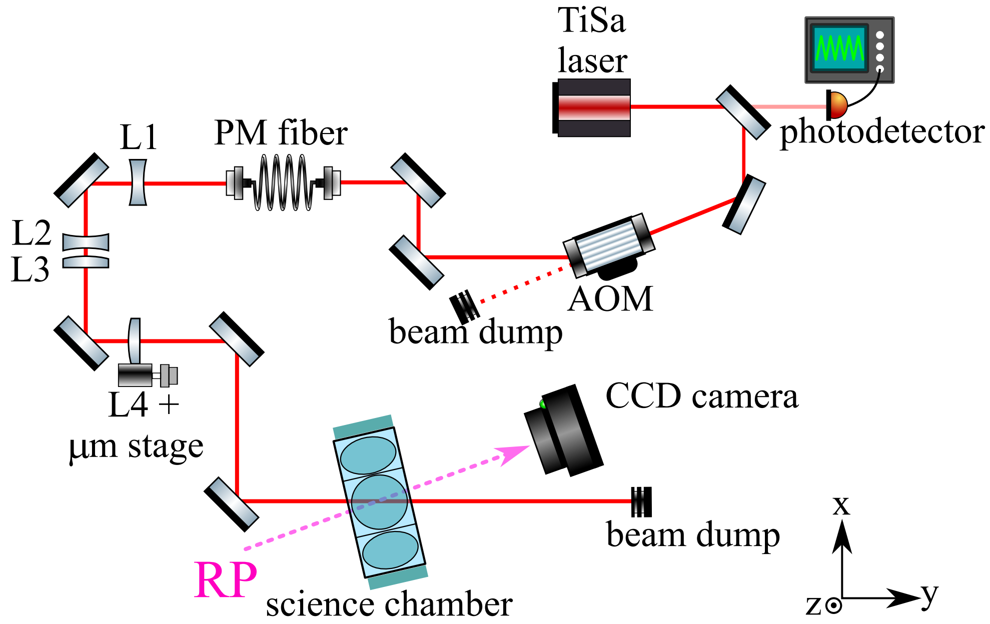

Fig. III.6 *Magical wavelength measurement setup, a red probe (pink dashed) addressing the intercombination line is absorbed by the atoms in the science chamber. We compare the absorption peaks position with and without the ODT beam (red). At the magical wavelength, the two absorption peaks are matching.*

When the 2D gravity beams address the intercombination line of naked Bohr frequency ω_{eg}, nothing guaranties that this frequency remains constant in the ODT because of the energy shift experienced by the atom inside the trap. Therefore, the resonance condition might be not fulfilled at every position of the ODT. The deviation from the bare Bohr frequency is:

$$\Delta\omega(\mathbf{r}) = \omega_{eg}(\mathbf{r}) - \omega_{eg} = \frac{|E(\mathbf{r})|^2}{2}(\alpha_g - \alpha_e) \tag{3.35}$$

We wish to have only a spatial dependence due to the artificial gravity and not from the ODT differential light shift between the upper and lower levels. We can suppress $\Delta\omega(\mathbf{r})$ by finely tuning the ODT wavelength. In this configuration, the Bohr frequency ω_{eg} is the same either in the vacuum or in the ODT. For the calculation of the strontium-88 light shift and magical wavelengths, we used 28 states of interest below the principal quantum number $n \leq 11$. The different rates and correction factors are found in the literature in [74, 75, 76, 77, 78, 79]. Once all those parameters are gathered, we simply have to apply together Equations 3.24 and 3.25 for the direct calculation of the polarizabilities. This calculation has to be compared with the measurement which is realized schematically as in Figure III.6. The set of lenses L1 to L4 are giving the elliptical beam profile to the ODT and the μm stage on the last lens allows a fine tuning of the ODT position that maximize the trap loading. The $^1S_0(m = 0) \rightarrow {}^3P_1(m = \pm 1)$ intercombination line of the cloud of strontium-88 is addressed by a linearly polarized (xy plan) red probe. The ODT polarization is linear along $\hat{z}$, choosing the quantization axis along the ODT polarization has the consequence that the light shifts of the $m = \pm 1$ levels are the same by symmetry. We could add a DC bias magnetic field along $\hat{z}$ in order to be insensitive to stray magnetic fields. There are two reasons why we do not work with this bias field in practice. First, we work at large detuning with the artificial gravity and are not concerned by the slight additional broadening that stray magnetic fields can create. Second, adding a magnetic field breaks the symmetry (Zeeman effect) between the $m = \pm 1$ states and we cannot address the two states with only one gravitational beam, we thus reduce the efficiency of the artificial gravity by if doing so.

The measurement is done in two steps, a first absorption spectroscopy is performed after loading the atoms in the ODT and a second one is performed after releasing the atoms from the ODT. The ODT wavelength λ is changed by regular step between 860 nm and 940 nm.

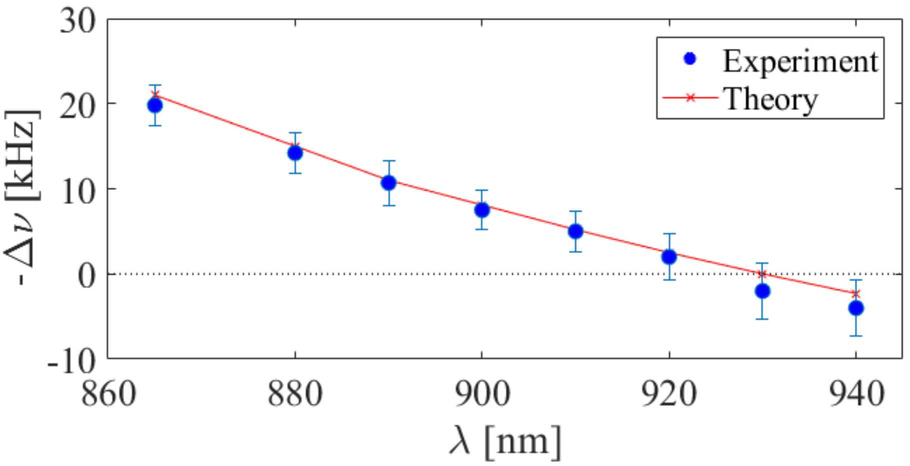

Fig. III.7 *Relative light shift in* $\mathbf{r} = \mathbf{0}$ *of the* $^1S_0(m = 0) \rightarrow {}^3P_1(m = \pm 1)$ *by a linear* $\mathbf{e}_z$ *polarization ODT. Cancellation of the relative shift is observed at* $\lambda \approx 925$ *nm.*

The differential frequency shift $\Delta\nu = \langle \Delta\omega \rangle / 2\pi$ versus λ is shown in Figure III.7. We represent the fact that the absorption imaging gives an average light shift by a bracket $\langle\rangle$. Indeed, the spectrum we obtain by absorption spectroscopy is skewed (inhomogeneous broadening) since atoms from the center of the trap experience a larger shift than the one on the edge, the spectral line are no longer symmetrical. This skewness disappears at the magical wavelength, also when the differential light shift cancels. We find the magical wavelength experimentally around $\lambda_M \approx 925$ nm which is in very good agreement with our calculation. The differential light shift is negative for $\lambda < \lambda_M$ and positive for $\lambda > \lambda_M$.

In summary, we chose the ODT laser to be locked at λ_M for the reasons given in Section III.3.2, that a non-zero differential light shift is equivalent to have a variable atomic frequency within the ODT: a traveling atom in the ODT will be at resonance when at the center, then out of resonance on the edge of the trap and thus experience a spatial dependent force. Since our modelization for the gravitational force is taken with a fixed atomic frequency, we must suppress expressly the light shift, formally done by setting the ODT wavelength to λ_M.

Chapter IV

Experimental setup

The strontium source was designed to specifically deal with quantum gases, while many experiments around the world are focusing on the $^1S_0 \rightarrow {}^3P_0$ clock transition [80, 81, 82]. Strong efforts where made after successfully mounting the setup to optimize the loading rate of the magneto-optical trap up to 6.10^9 s^{-1} [83]. This high loading rate leads to numerous advantages but mainly: having higher duty cycle and a higher atom number. Ultimately and hopefully, quantum degeneracy will be reached by the end of 2018 thanks to the work of the current Ph.D. students and the advantages of the initial design of the setup.

For our experiment, the gravitational collapse didn't require to work at high densities and we found ourselves running the experiment without repumping atoms. Reducing the atoms number, lead unfortunately to a decrease of the signal. Working in two dimensions as well reduces the signal observed and then required us to rethink the imaging system with a higher resolution < 2 μm and larger numerical aperture.

The Singaporean hot and wet weather is very demanding for everyone, the Nanyang Technological University is then in charge of cooling and drying the air not only for students, but as well for the experimental apparatus. In the laboratory, the humidity level is near-constant 53 % and the temperature maintained at 22 °C. Another potential source of instability is the mechanical vibrations arising from activities on the campus and inside the physics department. For this reason, the optical tables of the experimental apparatus are isolated from the ground thank to active damp feet. Among the three optical tables, two are dedicated in preparing the MOT beams and one is hosting the atomic source and optical dipole trap apparatus.

This chapter will expose in detail the experiment preparation, while the measurement scheme and imaging system will appear later on, in their own dedicated chapter. A short introduction (Section IV.1) on alkaline-earth elements and especially the strontium atom used in this experiment, will expose their properties and modern use. In section IV.2, we will then go through the apparatus in two steps. First, for the atomic flux preparation and the trapping. The initial design of the experiment (used to study non-Abelian gauge transformations with the ^{87}Sr [84]) was substantially modified for the collapse experiment. As such, the apparatus backbone went through a complete overhaul. In addition to this re-optimization, the ODT design plus magical wavelength measurement previously presented, were original works realized during this thesis. Section IV.3 will be devoted to the description of the different lasers who as well, had their internal components re-optimized. Finally, the high resolution imaging system we designed especially for the experiment will be presented in Section IV.4.

IV.1 Strontium atom

IV.1.1 Alkaline-earth metals: history and properties

Earths designate historically substances that are insoluble in water, nonmetallic and remaining unchanged while heated. Earths sharing similarities with alkalis where called naturally: alkaline earths before anyone knew about their atomic detail. Both alkali metals and alkaline-earth metals have positive oxidation numbers and form respectively salts or oxides. That is why, historically those two groups of atoms were names after their compound properties and not considered as metals. Humphry Davy in 1808 was the first to experimentally realize the separation of the metal cation from its anionic counterpart by electrolysis, see [85] for a historical review. Davy, thank to eloquent demonstrations of his theory, established himself into highest positions in the British science society. Internationally recognized during his early career, he is also responsible for a paradigm shift in the theory of acids, pulling the rug out from under Antoine de Lavoisier and proving him wrong. Subsequently to Davy's seminal work, the group of alkaline earth was renamed alkaline earth metals. This chemical group is made of six elements: beryllium (Be), magnesium (Mg), Calcium (Ca), Strontium (Sr), Barium (Ba), Radium (Ra). All those elements, exception made of Radium, have major commercial applications:

- Be is one of the lightest metals and has one of the highest melting points. It is then used as a structural material for high-speed aircraft, missiles and satellites. In high-energy physics, the low atomic number -and thus low sensitivity to energetic particles- of beryllium is used to build windows close to the beam line of particles accelerators (see the example of LHC beam pipes design [86]).

- Mg tarnishes slightly in air and ignites upon heating in air, burning with a dazzling white flame. It is used for flashlight photography, flares and pyrotechnics. It is lighter than aluminum and in alloys is essential for airplanes construction. Nevertheless, it is not candidate to replace aluminum due to its high flammability. Magnesium has other uses in the production in iron, steel and titanium. In atomic physics, magnesium is a potential candidate for next

Fig. IV.1 *Humphry Davy giving a lecture and executing a demonstration of his work at the Surrey institution. Photo courtesy and copyright of the Lewis Walpole Library.*

generation frequency standards [87]. It is however less developed compare to current Sr and Yb optical standards.

- Ca, under ionic form, is an essential constituent of leaves, bones, teeth and shells. It is without saying that it is also vital in the health of muscles, as well for blood circulation and digestive system correct functioning. The metal is used for its reducing properties in the preparation of other metals like uranium. It is also used as deoxidizer, desulfurizer or decarburizer for various alloys and serves in flashed getters to remove residual gases in vacuum tubes. In atomic physics, ^{40}Ca was the first species of alkaline earth metal to be brought to quantum degeneracy in 2009 [88]. Calcium has been used for optical atomic clocks both for single-ion clocks or for many atomic clocks [89]. However, and despite many advantages, calcium magneto optical traps are not efficient due to the complex energy levels [90], and other species of atoms -Sr, Yb, Hg- have been more usually preferred for optical frequency standards.

- Sr gives a beautiful crimson color to flames and is used in pyrotechnics and for the famous maritime distress signal flares. One of the strontium isotopes, ^{90}Sr is radioactive with a short half-life, being consequently a dangerous actor of nuclear fallouts and radioactive wastes. ^{90}Sr is a "bone seeker" and its presence can cause cancer. In atomic physics, the section IV.1.2 sums up recent uses of the strontium atom in the context of frequency standards and quantum gases.

Isotope	Mass [Da]	Abundance	Nuclear spin	Magnetic moment [μ_N]
^{88}Sr	87.905619	82.58%	0	0
^{87}Sr	86.908884	7.00%	9/2	-1.093
^{86}Sr	85.909267	9.86%	0	0
^{84}Sr	83.913430	0.56%	0	0

Table IV.1: Strontium isotope abundance. (NIST data)

- Barium is mostly used as a getter in vacuum tubes and for high contrast X-Ray of the digestive system. Historically, alchemists during Middle Ages were attracted by it because after exposure to the sun, it could glow for years. In atomic physics, barium has been studied in the context of Paul traps[1], a fundamental tool for quantum information processing. Novel techniques of trapping ions and neutral atoms together [92], gives now the possibility to control and study single ion in an atomic cloud [93], formation of molecular ions [94] and possible applications for sympathetic cooling [95].

- Radium was formerly used in luminous paints. In the mid-1920s, this type of paints was abandoned due to the death of five "Radium Girls", who were at this time working in factories and assigned the painting of dials for watches and clocks. Now, most of the practical uses of Radium derive from its radioactivity, especially in medicine as a cancer treatment. However, it is an element dangerous to handle and has been progressively replaced by safer isotopes of Cesium and Cobalt. In atomic physics, radium was recently used in an attempt to find a non-zero permanent Electric Dipole Moment [96]. This search is motivated to explain the matter-antimatter asymmetry in our Universe or reveal new sources of charge-parity violation which would put severe constraints on many models in Physics.

IV.1.2 The strontium element

a) Introduction

Strontium is a mixture of four natural and stable isotopes. On Earth, strontium occurs under few mineral forms, one being more important than the others because more commonly refined: the strontium sulfate or Celestine.

b) Inter-particles scattering

Interactions between atoms at low temperature are usually simplified [37]. The complex potential describing collisions between two atoms has its detailed structure

---

[1] In the honor of its inventor Wolfgang Paul who invented this method [91]. Also known as quadrupole ion trap or radio frequencies trap.

Isotope	Scattering length $[a_0]$	Abundance
^{88}Sr	-2	82.58%
^{86}Sr	+800	9.86%
^{84}Sr	+124	0.56%

Table IV.2: Scattering length of strontium Bosonic isotopes.

blurred and replaced by a simpler potential. Consequently, the scattering between atoms becomes only depends on few parameters and despite those important simplifications, this Utopian picture still encapsulates a very wide range of phenomena of the physics of composite molecules[97] and quantum phases [98]. In this last case, even if interactions are not necessary to reach Bose Einstein condensation (BEC), they are present in any real system and needed to reach thermal equilibrium and in consequence, interactions are a mediator of degeneracy[2] and have to be taken into account to correctly understand the modification of critical parameters (as the critical temperature of a transition) in comparison with the ideal non-interacting case [99].

Strontium is an interesting case in the field of quantum gases. Its main Bosonic isotope has a near zero scattering length (see table IV.2). Those values where obtained from photo-association spectra by different groups [79, 100]. Degeneracy was first reached on the ^{84}Sr isotope [101, 102]. The next Bosonic isotope is the ^{86}Sr which shows an extremely large scattering length and is then limited by inelastic three-body losses. As the inelastic collision rate varies as n^2 and the elastic scattering rate varies as n. The trick to reach degeneracy on this isotope is to lower the density [103]. Finally, the most abundant Bosonic isotope ^{88}Sr was brought to degeneracy by sympathetic cooling with its Fermionic counterpart ^{87}Sr [104].

Photo-association[3] and Feshbach resonances[4] have open the opportunity to produce molecules from ultracold gases. The first is the result of the interaction of two unbound atoms absorbing a photon to an excited molecular state, the second is the interaction of two unbound atoms where the scattering is made resonant with a molecular state by continuously tuning the scattering length. Properties of intra- and inter-species scattering have been a serious center of interest of experi-

---

[2] Collisions at low energies can be reduced to a single quantity, the scattering length a describing the amplitude and type of two-body interactions. Interestingly, if interactions are not necessary to reach BEC in its theoretical derivation, it is not the case experimentally. The sign and magnitude of a matters, in fact stable BEC is only possible for positive values of a.

[3] First evidence of photo-association was given before atoms where optically cooled or trapped by Scheingraber and Vidal in [105]. They observed fluorescence of free to bound transition while shining UV light on Mg_2 molecules. Photo-association is used to determine the scattering properties of atoms in their ground states [106].

[4] It was found in [107] that for specific values of the magnetic field, the two-body scattering length diverges, indicating the appearance of a bound state. A clear formalism was given soon after [107]. The phenomenon is named in honor of Herman Feshbach, who studied this problem in the context of nuclear physics.

mentalists. In the special case of strontium, more and more examples of theoretical [108, 109], ab-initio [110], semi-empirical [111] and experimental [100] determination of scattering lengths and dispersion coefficients appeared in the literature, they give important information to test models of atomic potentials or molecular wavefunctions [112]. Those data are used then by experimentalists to take advantage of inter-species scattering properties to bring one of the two species close to degeneracy [113, 104] which would have been impossible before. Indeed, precise measurements of scattering lengths of several elements -which has beaconed experimentalists to reach quantum degeneracy- has been made possible by photo-association spectroscopy measurements.

Interestingly, physics of ultracold atoms is not a closed field because of the numerous universal behavior that appear in several regimes. Atoms within the realm of very low temperatures, erase the complex structure of atomic potentials thank to their large wavefunctions. If two atoms interact in context of Feshbach resonances, the divergence of the scattering length makes each atom an actor of a strongly correlated dynamics. It is the so-called unitary regime [114] where few parameters are then enough to describe the system of interacting atoms. This sheds light over many-body physics models that are still to be tested. Strontium Feshbach resonances [115] have been used to create condensates of molecules. It is even possible to combine three atoms into an Efimov state[5] when reaching the same type of universal behavior as in Feshbach resonances. In the future, atomic physics might become the torchbearer of other physics field because of the universality at low-energy applying virtually to any other field such as condensed matter or high-energy physics.

c) Electronic levels of ^{88}Sr

The electronic structure of strontium 88 consists of two valence electrons. The two main transitions used for cooling and trapping are:

- The broad singlet to singlet $^1\mathrm{S}_0 \rightarrow {}^1\mathrm{P}_1$. The transition lies in the visible blue at 461 nm and has a natural linewidth of $\Gamma_b = 2\pi \times 32$ MHz or conversely a lifetime of $\tau_b = 5.26$ ns [100]. Other values of this linewidth can be found in the literature such as in a previous measurement [117]. In this state, atoms can escape toward the $^1\mathrm{D}_2$ state with a non-negligible branching ratio of $\sim 10^{-5}$. The atoms have then 33% chances to decay towards the $^3\mathrm{P}_2$ and 66% towards the $^3\mathrm{P}_1$. This problem is circumvented using repumping lasers (see section IV.2.4).
- The singlet to triplet $^1\mathrm{S}_0 \rightarrow {}^3\mathrm{P}_1$ which is dipole semi-forbidden[6] due to the required spin-flip is an example of metastable state[7]. The transition lies in

---

[5] Realized experimentally for the first time with cesium atoms in 2006 [116]

[6] Forbidden by strict selection rules but allowed by spin-orbit coupling.

[7] Metastability, in this context means that the lifetime of the state is much larger than other

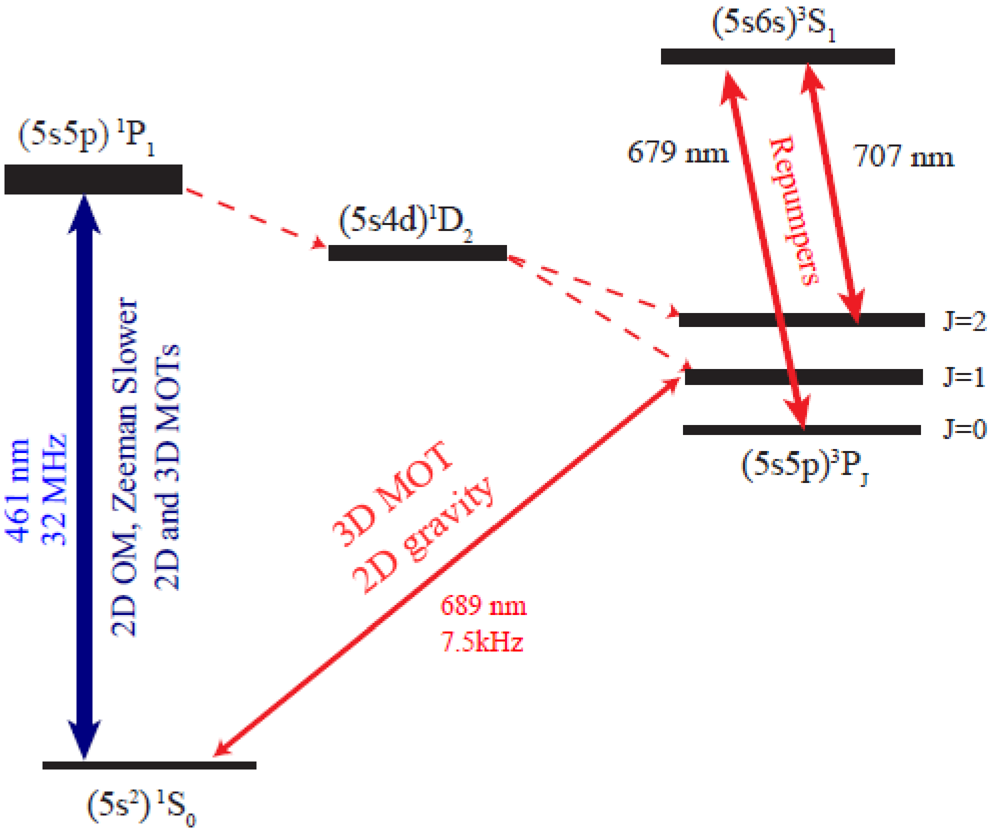

Fig. IV.2 *Simplified energy levels for the* ^{88}*Sr.*

the visible red at 689 nm and has a natural linewidth of $\Gamma_r = 2\pi \times 7.5$ kHz or conversely a lifetime of $\tau_r = 21.4\ \mu$s [69].

The other principal state of interest is the ^{3}P$_0$, whose linewidth is near zero for bosonic isotopes in the absence of external fields, while it is close to $\sim$ 1 mHz for the ^{87}Sr due to the hyperfine interaction. The reason is the following. Some states have a near zero linewidth and thus a lifetime of the order of thousands of years. This is the case for the ^{3}P$_0$ state in ^{88}Sr. However, while switching to the ^{87}Sr , the non-zero nuclear spin allows hyperfine interaction with higher states and gives a finite linewidth [118] to the state. Hyperfine mixed states are among the favorite candidates to create frequency standards [119].

IV.2 Experimental setup and sequence

We will present here the different elements constituting the experimental setup, from the atomic source, different cooling and trapping stages and finish by the imaging

---

typical excited states. The slow decay from a metastable state, usually unwanted is compensated by repumping the state into another state more likely to close faster the transition cycle.

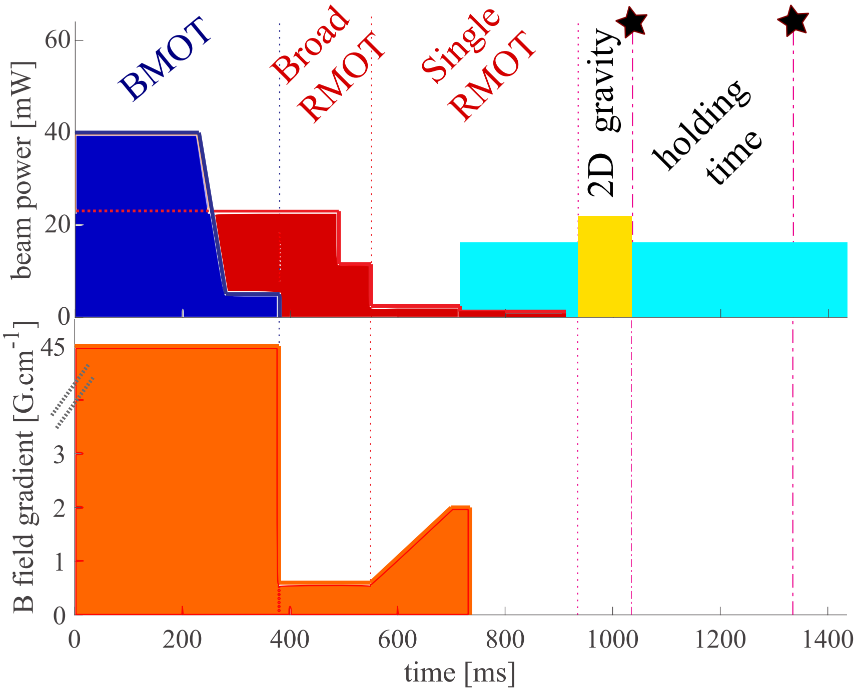

Fig. IV.3 *Experimental sequence with blue and red MOT (resp. BMOT and RMOT) beams power and magnetic field gradient value. (deep blue) blue MOT power. (red) red MOT power. (sky blue) ODT beam in arbitrary unit. (yellow) 2D gravity beams in arbitrary unit. (orange) Magnetic field gradient. Black stars indicate the two moments at which fluorescence imaging are performed, once right after the 2D gravity and a second time after a long holding time to deduce the temperature and compression factor.*

.

scheme. For a historical overview of strontium experiments of different groups over the world as well as a discussion on degenerate gases of strontium, see the recent review [120]. The setup used for this experiment was developed over the last 8 years and a complete description of it can be found is [83]. Several topics where covered over the last few years from coherent superflashes [121, 122] to non-Abelian gauge fields [84].

The experimental setup is designed for either Fermionic ^{87}Sr and Bosonic ^{88}Sr species of strontium. Since we work with the Bosonic ^{88}Sr, which has zero nuclear spin, the complex energy structure simplifies to minimal one represented in figure IV.2, which will be enough to explain each stages of the experiment.

The time sequence regarding the cooling, trapping, 2D gravity collapse and fluorescence imaging is depicted in Figure IV.3. The optical transitions at 461 nm (blue) is nearly closed and thus advantageous for cooling or trapping. The broad $\Gamma_b = 32$ MHz transition ($^1S_0 \to ^1P_1$) can be addressed by converting a 922 nm laser into 461 nm by frequency doubling. This blue laser is then used for the 2D optical molasses, the Zeeman slower, the 2D MOT deflector and the 3D MOT. After this first stage of cooling called blue MOT (BMOT). Drawings and details of the blue laser are given in Section IV.3.1. On the other hand, the narrow $\Gamma_r = 7.5$ kHz transition ($^1S_0 \to {}^3P_1$), used for the two next stages of cooling, a broadband red MOT (Broad RMOT) and a singleband red MOT (single RMOT). This transition is addressed by an external-cavity diode laser (ECDL) injecting several slave diodes to power the MOT beams and long-range force beams. Typical ECDL have a linewidth below the megahertz, which is not low enough to resolve the narrow 7.5 kHz transition so that the laser linewidth is reduced by locking the laser on a Fabry-Perot cavity. Since this transition has a low capture velocity range, we address the atoms with the red laser only for the last stages of cooling in the 3D MOT. Details on the special attention given to the frequency locking and the narrowing of the linewidth of the red laser and its optical paths are provided in Section IV.3.2. The atoms are then transfered from the single RMOT to the dipole trap (sky blue on Figure IV.3) at the middle of the single RMOT. The 2D gravity is then turned on while the atoms are in the dipole trap (yellow on Figure IV.3). The 2D gravity beam addresses also the $^1S_0 \to {}^3P_1$ transition and comes from an additional path of the red laser.

While operating on the blue transition, atoms can escape toward the $^1D_2$ state with a non-negligible branching ratio of $\sim 10^{-5}$. The atoms have then 33% chances to decay towards the $^3P_2$ and 66% towards the $^3P_1$. The optical pumping procedure to circumvent this trapping within the $^3P_2$ state is detailed below in section IV.2.4.

IV.2.1 Atomic source: vacuum and 2D molasses

Atomic vapors of alkali metals and alkaline-earth metals, used in many atomic physics experiments, are very corrosive for fused silica windows and forbid their use as view-ports. One must find other materials, less reactive to those species and able to sustain high temperatures[123, 124]. Diamond and sapphire are few of this kind but the former being too expensive, sapphire is usually preferred. Other apparatus involving a buffer gas are efficient to reduce contact between atoms and the cell walls. However, scattering between the element of interest and the buffer gas lead to collisional broadening and shift of the spectroscopic lines, it is a subject of interest for clock transitions to access dispersion coefficients of the atom driving the clock and the residual gas [125].

In our case, a solid strontium source (Figure IV.4) is loaded in a stainless-steel cylinder heater at 550 °C, this oven generates an atomic strontium vapor by sublimation. A higher temperature is possible and would increase the brightness of the atomic beam, if needed in another experiment. The temperature is maintained thank to a negative feedback loop and ensures a constant particle flux from the effusive beam. This beam is collimated by going through a multichannel nozzle

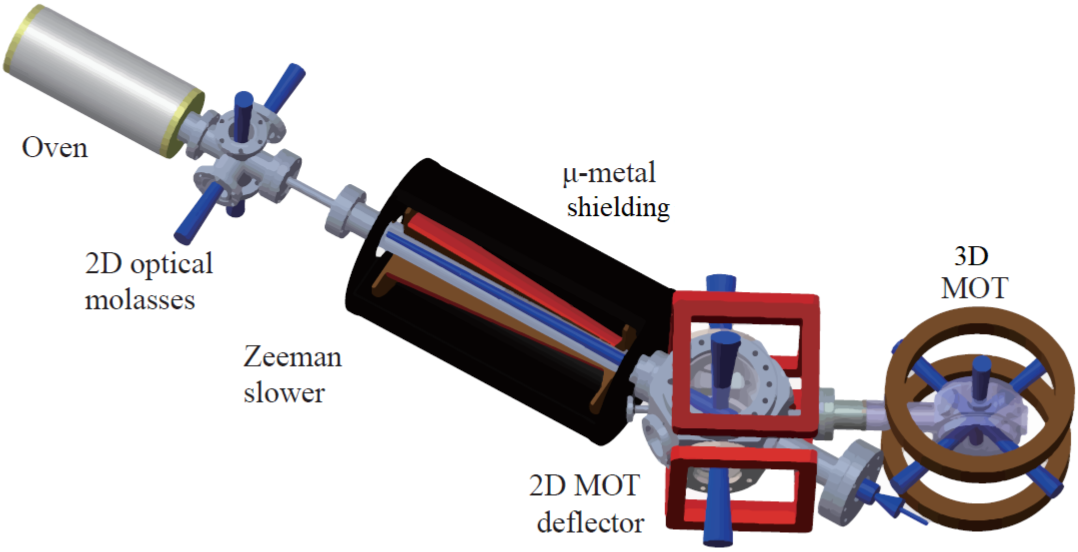

Fig. IV.4 *Schematic overview of the setup.*

made of nine hundred Monel 400[8] micro-tubes of 1 cm long. The inner and outer diameters of each micro-tube are of 200 μm and 300 μm respectively. The temperature of this nozzle is maintained roughly 50 °C higher than the oven to ensure that the micro-tubes are not clogging from strontium condensation.

The collimated beam has nevertheless a non-zero divergence that can be improved by adding a transverse molasses red detuned on the broad 461 nm transition. It is done 15 cm after the nozzle using two pairs of retro-reflected beams having an elliptical shape (beam waists: 1 cm and 0.5 cm). The major axis of the beam being oriented along the atomic beam. Optimal loading rate is found for detuning of -18 MHz = -0.55 Γ_b. Thank to this transverse cooling, the blue MOT loading rate is being improved by a factor three.

After going through the 2D molasses, the atomic beam travels over 10 cm in a tube of inner diameter 1 cm. This filters part of the residual hot atoms having a high transverse velocity component. It results from this previous filtering, a differential pressure between the oven and the next part of the experimental apparatus (Zeeman slower and 2D MOT) which are benefiting from an improved vacuum[9]. The longitudinal cooling is then taken in charge by the next element of the apparatus: the Zeeman slower, detailed below.

IV.2.2 Zeeman slower

The nearly collimated atomic beam has its longitudinal speed reduced using a 32 cm long Zeeman slower: the atoms are moving in an inhomogeneous magnetic

---

[8] A type of nickel-Copper alloy, very resistant to alkalis and high temperatures.

[9] Another last differential pressure tube is place between the 2D MOT and the science chamber.

field and face a counter-propagating laser beam red detuned. Its principle is the following: in the presence of a homogeneous magnetic field, the *generalized* condition of resonance $\delta(B_0, \omega_0, \omega_L, \vec{v}) = 0$ for a two-level atom is modified if one of the levels has a non-zero magnetic moment. To slow down an atom, it needs to absorb many photons and if B_0, ω_L are constant, atoms end up quickly out of resonance after $\Gamma_b \lambda_b^2 m/h \approx 1500$ absorptions, limiting the slowing distance to only few millimeters and the slowing time to few milliseconds. To make atoms responsive to the photons over a longer distance, the magnetic field can be made spatially dependent on $B(\vec{x})$ along the atomic beam, allowing one to follow the resonance condition over tens of centimeters.

Our Zeeman slower is made of a 32 cm long solenoid-type coil. The coil is realized by winding flat copper wires in a tapered way. The optimum current of 6,6 A gives a magnetic field varying from 500G at the entrance of the solenoid to -100 G at the output. The laser beam is addressing the broad 461 nm transition with a frequency detuning of $-13\Gamma_b$ and a power $\sim$ 120 mW. The view-port is made of z-cut sapphire[10] and maintained at a temperature of 375 °C.

Under those parameters, atoms with a longitudinal speed lower than 525 m.s^{-1} can be slowed down. After the Zeeman slower, the velocity distribution loses its typical Maxwell-Boltzmann shape and displays a peak at $\sim$ 100 m.s^{-1}, which to sum up things makes atoms lose 80 % of their speed in the process, or noting that $v_{rec} = 9.85$ mm.s^{-1}, it is equivalent to say that in average an atom has absorbed $\sim 5 \times 10^4$ photons.The loading rate of the blue MOT benefits greatly from the use of a Zeeman slower, it is in overall improved by a factor of 300.

To avoid any perturbation in the rest of the apparatus, the strong magnetic field of the Zeeman slower is confined using μ-metal[11] sheets. Finally, because the shielding modifies only the coils external field, overall efficiency of the Zeeman slower is not affected by the shielding.

IV.2.3 2D magneto-optical trap

After the Zeeman slower, the atomic beam is deflected and further cooled transversally using a 2D MOT (see Figure IV.5). This 2D MOT has an escape direction along its symmetry axis. Thus, it is guiding atoms along this axis and deflect them at any reasonable angle. By choosing a 30° angle with respect to the previous Zeeman slower, it guaranties us several advantages:

- The intense optical beam used for the Zeeman slower does not cross the region in the science chamber and thus prevents disturbing the experiment.

---

[10] Sapphire is slightly birefringent and must be cut perpendicular to its optical plane, allowing to retain the polarization of any normally incident laser.

[11] A nickel-iron alloy with very high permeability, typically $10^5 \quad \mu_0$. The magnetic flux entering a μ-metal will flow inside rather than exiting. The best shape for the shield is then a fully close container surrounding the solenoid.

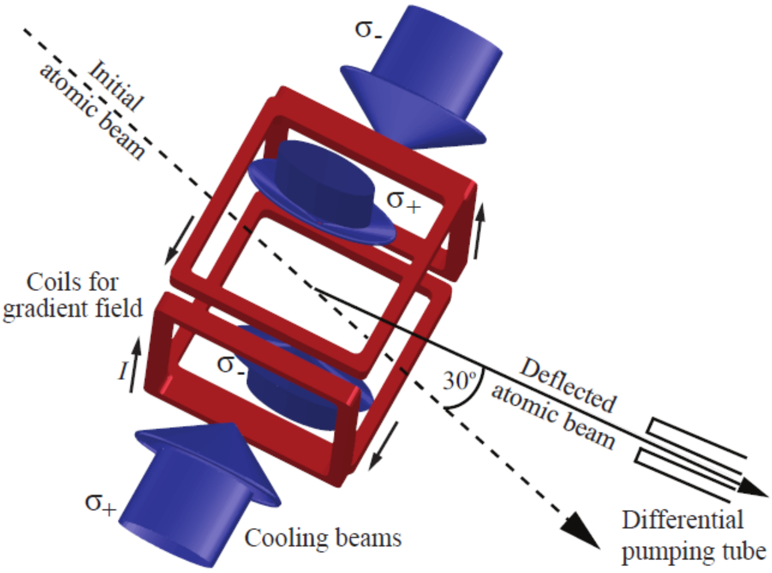

Fig. IV.5 *Schematic view of the 2D MOT atomic beam deflector. After being deflected at an angle of θ =30° from its incident direction, the atomic beam passes through a differential pumping tube.*

- The deflection allows to prevent hot atoms and unwanted isotopes to enter the science chamber.

- Deflecting atoms that way, will clear an additional optical axis for the science chamber.

- Once the science chamber is loaded, the 2D MOT can be turned off as a switch. Such that the input flux of atoms drops to zero without requiring any mechanical blocker.

The two-dimensional quadrupole magnetic field is generated using four square shaped coils. Each coil has a square geometry of inner and outer dimensions of respectively 15 cm and 19 cm. Additionally, each coil is formed by 22×2 turns layers of a 1 mm copper wire. Optimal loading of the 3D mot in the science chamber is found at a magnetic field gradient of 7.5 G.cm^{-1}. Regarding the retro-reflected beams, 180 mW is borrowed from the 461 nm laser and its detuning set to $-0.9\Gamma_b$. After a succession of AOMs, the power then available is P_{2D} =100 mW, among which 60% is being sent to the horizontal direction to supply the deflection. The remaining power is sent along the vertical direction to help focusing and further cool transversally the atomic beam before entering the science chamber.

IV.2.4 Blue 3D MOT

After being deflected, the atomic beam enters the science chamber through a differential pumping tube with an average longitudinal velocity of 50 m.s^{-1}. The beam is slow enough to be captured on the broad blue transition but requires further cooling to allow trapping on the narrow red transition which has a typical capture velocity of 1 cm.s^{-1}.

To save space and laser power dedicated to the trapping, the MOT beams are retro-reflected and overlapped. The magnetic field gradient is generated by a pair of coils in anti-Helmholtz configuration and its optimal value maximizing loading of the blue MOT is found at 45 G.cm^{-1}. The three beams -along $\hat{x}, \hat{y}, \hat{z}$- have a typical waist of 1 cm and a power of 17 mW. The optimal detuning is found to be -1.8 Γ_b.

The $^1S_0 \rightarrow ^1P_1$ transition is not exactly closed and leaks towards the underlying $^1D_2$ state below (see Figure IV.2). Atoms in the latter state are likely to decay to the metastable state $^3P_2$ and are then lost. The lifetime of the blue MOT is then reduced to few tens of milliseconds. To avoid this problem and close the transition, repumpers lasers are required and in general two schemes (see [126]) can be implemented. Using only one laser at resonance on the 497 nm transition which couples the long lived $^3P_2$ the $^3D_2$ state and by spontaneous emission to $^3P_1$, which decays back nicely into $1S_0$ and thus closes the MOT cooling cycle. The second technique, which is used in our experiment, is to repump atoms from the $^3P_0$ and $^3P_2$ states to the $^3S_1$ with respectively two lasers at 679 nm and 707 nm. Then, spontaneous emission brings down the atoms to the $^3P_1$ which decay into $^1S_0$ and closes the transition at the end of the day. The loading rate of the blue MOT is highly improved (of a factor $\sim$3) by the addition of repumpers whatever scheme is chosen.

After loading the trap, the atom number and density can be estimated by using standard absorption imaging with a detuned probe beam on the 461 nm transition. The peak density is estimated to be typically $n = 3 \times 10^9$ cm^{-3} and since the blue MOT has a size of $\sim$ 1 cm. At the end of this first trapping stage, we work at most with a population of a billion[12] of ^{88}Sr at an average temperature of 2 mK measured by time-of-flight (TOF). The blue MOT has a surprisingly long lifetime which can be attested by eye if one turns of 2D MOT and records the fluorescence signal of the 3D blue MOT. This long lifetime can be explained by the combination of two factors: the low two-body collisional loss coefficient (as mentioned in [112]) and the ultra-high vacuum quality realized experimentally.

In order to further cool and increase the phase space density, the power of the blue MOT is ramped down to 5 mW in 50 ms. This low power blue MOT phase lasts for 100 ms (see Figure IV.3).

---

[12] Peak density and number of atoms would be different for other strontium isotopes given their respective abundance and scattering properties.

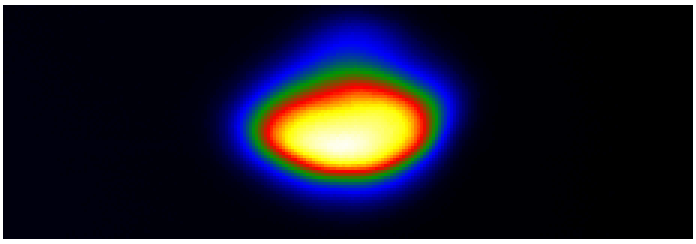

Fig. IV.6 *Fluorescence imaging (horizontal view) of the singleband red MOT.*

IV.2.5 Red 3D MOT

The first realization of trapping strontium on its $^1S_0 \rightarrow {}^3P_1$ spin-forbidden line at 689 nm happened 20 years ago [56]. The main advantage of this transition is the very low Doppler temperature $\sim \hbar\Gamma_r$, close to the photon recoil temperature $(\hbar k_r)^2/2mk_B$. This temperature and a higher spatial density of $\sim 10^{11}$ atoms.cm^{-3}, allowed physicists to reach phase-space densities as high as 10^{-2} with only laser-cooling techniques. It was even possible recently to push forward into this "all-optical means" direction [127] and produce a BEC of strontium without the usual evaporative cooling [101]. We will not be interested into degeneracy for our experiment and thus use the same standard design of magneto-optical trap as for the blue transition. The time sequence for the red MOT (Figure IV.3) can be simplified in two important phases: broadband trapping and single band trapping. The first takes advantage of an artificial broadening of the 7.5 kHz bare transition into 2 MHz which spans over a larger velocity range. Indeed, after the blue MOT, the RMS speed $\bar{v} \approx 0.5$ m.s^{-1}. The broadening addresses 2MHz$\sim 3\bar{v}/\lambda_r$ at a modulation rate of 25 kHz. It means that we are in the so-called wideband regime of frequency modulation and create about 80 resolved sidebands [128]. This first stage aims to transfer as many atoms from the blue to the red MOT as possible (30% in our case). The broadband sequence finishes with a low power phase is then performed as in the blue MOT sequence for further compression and cooling.

Consecutive to this broadband phase, the frequency modulation of the red laser is turned off and a single-band phase is performed. The last step before transferring in the optical dipole trap consists in decreasing further the red beam power and increasing the magnetic field gradient for maximum compression.

We access number of particles, sizes, optical thickness and density of the cloud by a standard absorption imaging. We have typically a cloud of vertical RMS $\sigma_\perp \approx 180$ μm and a horizontal RMS $\sigma_\parallel \approx 380$ μm. The total number of atoms is about 10^8 for a density 5×10^{11} atoms.cm^{-3}. We benefit highly from the narrow transition and reach a temperature of 2 μK prior to loading the ODT. In our case, the temperature is being reduced further to the detriment of the atom number.

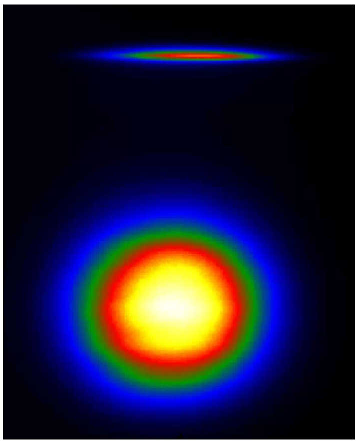

Fig. IV.7 *ODT and MOT, horizontal view. The image is realized by a fluorescence imaging on the blue* $^1S_0 \rightarrow ^3P_1$ *transition. The MOT has been released 20 ms prior to the picture.*

IV.2.6 Optical Dipole Trap

First insights on trapping atoms using dipole force was given in 1968 by Letokhov in [129], the author studied at the time how the velocity distribution is narrowed in a intense standing light wave and focused later (see [130]) on dragging forces in standing waves. The trapping effect was observed on micron-sized particles in liquids and gas in 1970 by Ashkin [131]. The first realization of the dipolar force on neutral atoms (Sodium) is due to Bjorkholm *et al.* in 1978 [132] and the true trapping -at the time only of several seconds- was made possible by Ashkin, Bjorkholm, Cable and Chu in 1986 [133].

The ODT is loaded during the single-band phase of the red MOT. We then release the MOT, it is illustrated by the horizontal fluorescence imaging in Figure IV.7.

a) ODT: power, beam waists and cloud size

The maximum power[13] delivered at the magical wavelength by the laser is 0.95 W. The atomic cloud after loading in the ODT have RMS about $\sigma_x = 60$ μm, $\sigma_y = 160$ μm and $\sigma_z = 6$ μm. We report $2{\times}10^6$ atoms at best -when all repumpers are working during the blue MOT phase- for a temperature of about 1 μK. The next step in the characterization in the ODT following its loading, is the measurement of its trapping frequencies. As, if the ODT beam is in the fundamental transversal mode of the laser and that the intensity is high enough, the trap is well approximated by a harmonic potential.

---

[13] At the level of the atoms and not at the output of the laser.

b) ODT: depth and frequencies

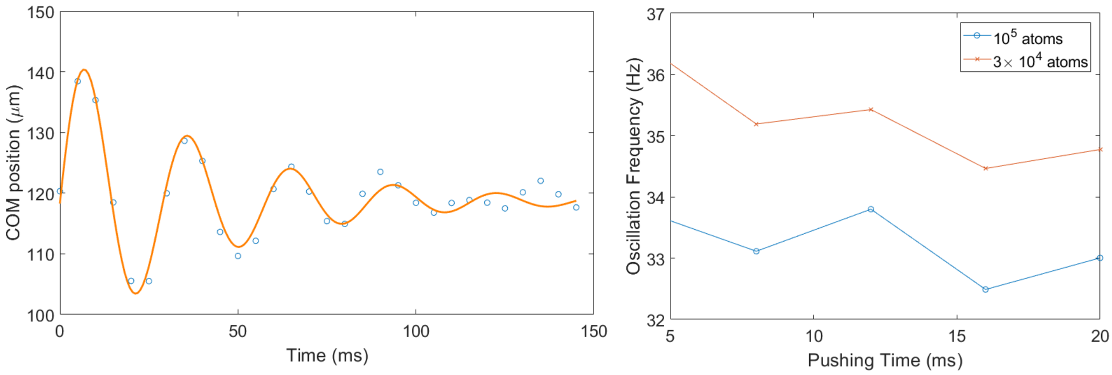

Fig. IV.8 *Fitting of the center of mass -quasi- harmonic motion along $\hat{x}$. (Left) For a kick of 20 ms with a resonant red probe. (Right) Dependence of the oscillation's frequency for different kicking time and number of atoms N=3×10^4 and N=10^5 atoms.*

Figures IV.8 show a measurement of the in-plane ODT frequencies ω_x. The measurement relies on the recording of the center of mass motion of the cloud in the ODT after a kick given a probe beam at resonance with the $^1S_0 \rightarrow ^3P_1$. In Figure IV.8 (left), we observe a damping and a desynchronization of the oscillations after typically $\simeq$ 100 ms, this is due to the imperfect harmonicity of the trap. The motion of an atom on the edge of the trap must account for lower frequencies corrections (the trap is an inversed Gaussian and not a perfect parabola) which become visible after a certain number of the fast harmonic oscillations. In Figure IV.8 (right), we observe a kick duration dependence on the measured frequency. The longer the kick is, the higher the atoms are put in the trap and experience a restoring force lower than in the central part of the trap. The deviation from the ideal harmonic trap is thus immediate and yields a reduced measured frequency. We also observe lower frequencies for larger number of atoms either because of a saturation of our probe that is not pushing homogeneously the atoms initially or either because, the more we have atoms, the more some of them are contributing to the desynchronization due to the anharmonicity at the edge of the trap.

The measurement along $\hat{y}$ yields a ω_y of only several Hertz and was thus quite difficult to fit with this method. The last axis $\hat{z}$ is unfortunately inaccessible to direct observation. By lack of luck, our ODT laser lost a lot of power right before and during the experiment and forced us also to abandon this method, only relevant to measure ω_x but not the others. We thus backed up our frequency measurement by means of the equipartition theorem (see Chapter III Equation 3.30) and our knowledge of the ODT characteristic sizes. It is thus possible to access every frequency and found about $\omega_x = 2\pi \times 23$ Hz, $\omega_y = 2\pi \times 7$ Hz and $\omega_z = 2\pi \times 1$ kHz before the power drops. Those frequencies together with the beam waists accessible by using a simple CCD camera, correspond to a trap depth of about $U(\mathbf{0}) = 25\ \mu\text{K}$ (upper bound).

c) ODT: mechanical stability

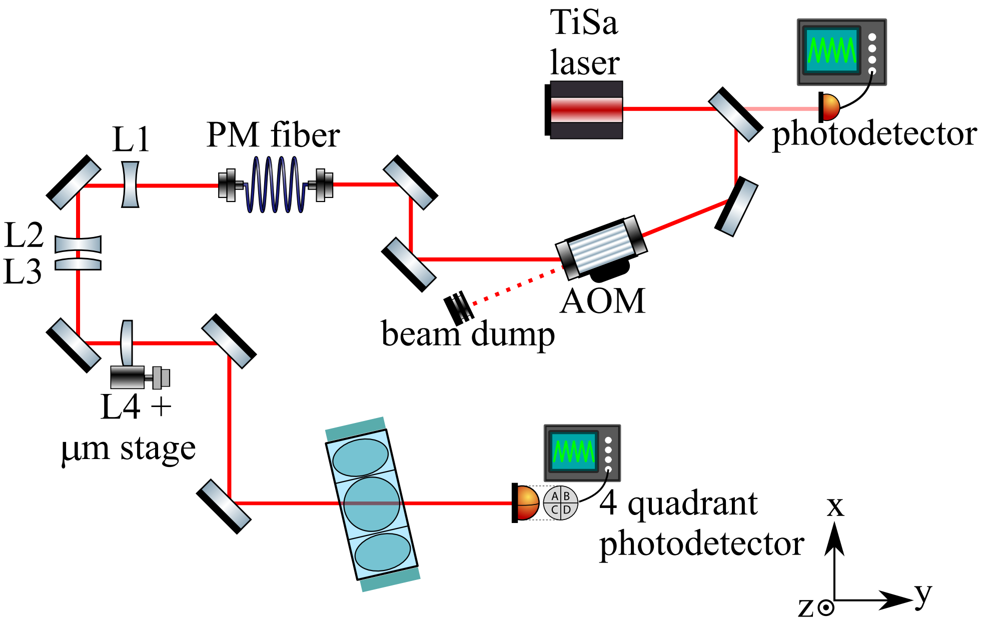

Fig. IV.9 *ODT's vertical stability measurement. The ODT beam is focused at low power -using a μm stage- on a 4-quadrant photodetector that keeps track of the beam position in the xz plan.*

Another point of interest is the ODT beam stability that is verified using the simplified setup represented on Figure IV.9. Since this beam is as thin as possible along $\hat{z}$ to give the 2D shape to our atomic cloud, it is sensitive to vibrations of the optical table. It is made worse by the nearly 1.5 meter long distance between the fiber output of the ODT and the atoms. Already between the lenses L1 and 4 are more than 1 meter of lever arm. We need such a long distance to prepare the beam shape by a succession of telescopes. The ODT beam propagating along $\hat{x}$ and using a four-quadrant photodetector, we are able to monitor its transverse yz motion. Actually, we don't run the exact same sequence as the experiment, we purposely focus on two key moments where mechanical instabilities arise, namely the two violent changes of magnetic field at the end of the blue MOT and the single-band red MOT. When the magnetic field changes rapidly, the optical table experiences a torque and vibrates. Track of the motion along $\hat{z}$ is particularly interesting since micrometers instabilities are comparable with the cloud thickness σ_z and can eventually weaken the trapping.

This measurement is given in Figure IV.10 where curves in green depict the bare experiment and curves in black the same experiment after reinforcing the

ODT support with additional steel rods. The effect of this reinforcement is quite visible, as the dark amplitude is generally smaller than the green one. The first jump at 0.1 s corresponds to the end of the blue MOT. The same phenomenon -for the red MOT this time- is visible at 0.7 s but much weaker because of the difference in the magnetic field values (see Figure IV.3). This measurement shows that the amplitude of this undesirable movement is small enough (about 1 μm) compared to the trap size.

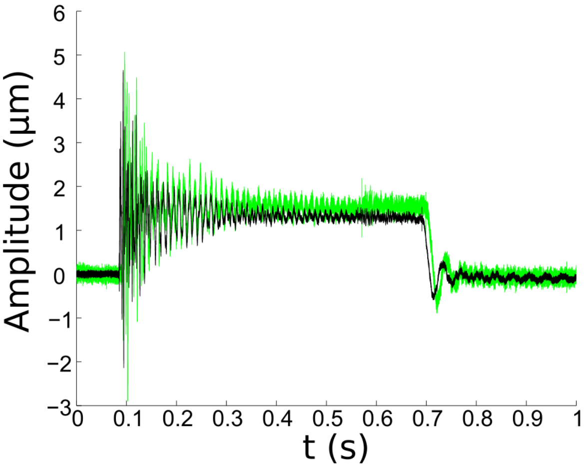

Fig. IV.10 *Four quadrant photodetector measurement of the ODT motion along $\hat{z}$. Amplitude of the movement during the pre-collapse sequence. The green curve (black curve) are realized before (resp after) adding reinforcing steel rods to the optical table. The effect of those rods is to reduce the amplitude of the ODT vertical motion during the abrupt change of the magnetic field (at 0.1 s and 0.7 s).*

IV.3 Laser system

This section is dedicated to the generation of different laser beams and their stabilization scheme. Stability of frequency, intensity and polarization ensures reproducibility of the experiment. There are three sections for respectively: the blue 461 nm, red 689 nm and IR 925 nm lasers.

IV.3.1 Blue laser at 461 nm

The 461 nm transition is addressing many elements: 2D optical molasses, Zeeman slower, 2D and 3D magneto-optical traps. The laser used is a commercial TOPTICA composed of: a master diode lasing at 922 nm, a tapered amplifier (TA) and a frequency-doubling cavity. To sum-up, the 922 nm beam is amplified then frequency doubled to the desired 461 nm wavelength. However, total power required to supply the complete experimental setup exceeds the power that can deliver our commercial laser. To generate more power, a polarizing cube extracts a small amount of infrared (IR) light after the master laser, which is sent to another optical table to be amplified and frequency doubled. The direct output of 461 nm light or "first path" is thus devoted to the 2D molasses, spectroscopy cell, 2D and 3D magneto-optical traps. Conversely, the secondary output of 922 nm light or "second path" is addressing the Zeeman slower which requires the most power among any other elements and the largest detuning.

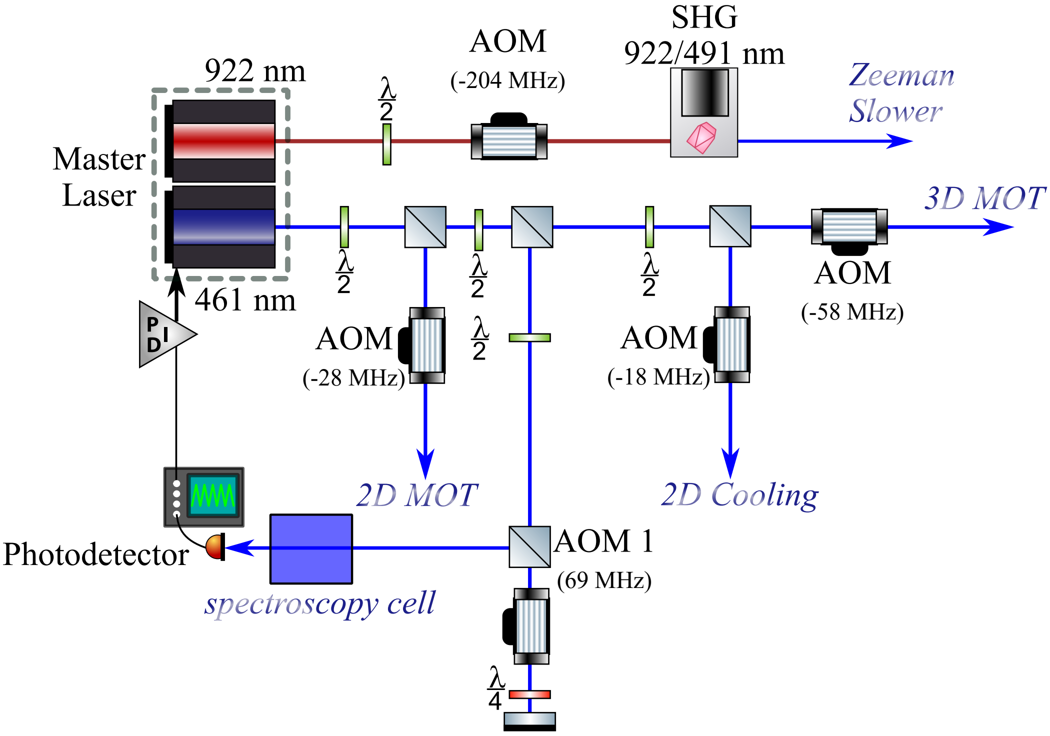

Fig. IV.11 *Optical setup for the 461/922 nm "blue" laser. The indicated frequencies are relative to the atomic reference (at $\delta = 0$).*

We first focus on the first path represented by the 461 nm output beam on Figure IV.11 and give a brief description of the commercial laser. The primary laser consists in a extended diode-laser (ECDL) delivering enough IR power at 922 nm to inject a tapered amplifier stage which amplifies the optical signal. The tapered amplifier (TA) can be seen as a laser-diode which achieves population inversion for a high enough incident power and driving current [134, 135]. If TAs compete with fiber amplifiers by their compactness, they however exhibit much stronger noise and nonlinear distortions. The main consequences of those distortions are self-phase modulation and four-wave mixing. Fortunately, the first effect[14] is not problematic

---

[14] Known as the Kerr effect, which can be described as a change of the refractive index when

for a laser working continuously. The four-wave mixing as well isn't a big deal (see e.g. [136]), since the laser linewidth is quite small compare to the natural linewidth of the transition. The IR beam goes then through a series of mode matching optics which ultimately injects a second-harmonic generator (SHG) unit. This unit consists in a "bow-tie" ring optical resonator[15] with a $\chi^{(2)}$. Second harmonic generation was demonstrated by Franken [137]. The 922 nm beam enters through one semi-reflective entry mirror into the SHG and is converted into 461 nm when interacting with the non-linear PPKTP[16] crystal. In the conversion process, two photons of frequency ω_i are "combined" into a new photon of frequency $\omega_f = 2\omega_i$. Details and fundamentals of nonlinear frequency conversion can be found in [138]. The total output power of the first path -after the SHG unit- is 240 mW.

The frequency of the laser beam is then given by the phase-matching condition of the SHG cavity and is not yet known with respect to any resonance. The lock on the $^1S_0 \rightarrow {}^1P_1$ transition is ensured by taking away few milliwatts of the laser beam and sent to a spectroscopy cell. The cell consists in an oven where a piece of metallic strontium is heated and generates a quasi-collimated atomic beam of optical thickness ~ 0.7. The laser beam is polarized σ^- and sent perpendicular to the atomic beam to reduce the Doppler broadening to a minimum depending on the quality of the collimation. A pair of Helmholtz coils is placed across the laser beam which set the quantization axis and allows to tune the Zeeman shift and thus the lock point, by a change of the coil current. The frequency-current calibration gives 36 MHz.A^{-1}, this degree of freedom for the frequency, allows to scan the lock point across any strontium isotopes. The laser is absorbed when crossing the atomic beam and transmission spectroscopy [139, 140] is realized. The frequency modulation for the spectroscopy is done by the AOM 1 (see figure IV.11) in a double pass configuration, the frequency is modulated at a rate of 15 kHz with a modulation depth of 15 MHz. The detected transmission signal is demodulated[17] and sent to a couple of fast and slow PID controllers acting on the PZT[18] controlling the cavity length of the master laser.

Apart from the frequency lock acting on the master laser, the second path is intensity-locked to avoid amplitude modulation at 15 kHz. This lock requires to work at a lower power than the absolute maximum given by the laser but ensures more repeatability.

The second path is represented by the 922 nm output beam on the figure IV.11

---

the optical intensity varies. It is then particularly important in the case of pulsed lasers.

[15] An optical resonator is a set of optical elements which allows light to circulate in a closed path. It can be used to stabilize or increase optical power, filter frequencies, clean the transverse mode of a laser, converting frequencies etc.

[16] Periodically poled potassium titanyl phosphate. Periodic poling consists in a formation of layers of alternate orientations in a birefringent material. The periodic structure created this way is more efficient than crystals for second harmonic generation.

[17] Frequency modulation spectroscopy are reviewed in [141, 142, 143]

[18] Lead zirconate titanate or PZT is a ceramic material that shows piezoelectric effect. Applying a voltage on it will change its size and gives a fine mechanical control over optical elements.

and is addressing the Zeeman slower. The few milliwatts of IR go through a succession of optical elements that amplifies its power. The beam first injects a slave diode which provides then enough power ($\sim$ 30 mW) to be sent into a homemade TA. The TA is controlled in temperature using a thermoelectric cooler (TEC) based on the Peltier[19] effect[144]. A thermistor measures the temperature of the TA which is sent into a comparison loop which sends the correct feedback to the Peltier module through PID controllers. The response time of the thermistor is quite slow; however, the TA doesn't experience fast changes of temperature but only slow thermal drifts. The TA delivers 700 mW of IR which is then sent through a polarization maintaining (PM) fiber to another SHG cavity. The 922 nm IR beam is converted up to 95% into 461 nm blue. However, the mode matching between the output of the TA and the PM fiber is not perfect and as a result, 50% of the IR light is transmitted to the SHG and $\sim$ 120 mW of blue are produced at the end of the second path.

IV.3.2 Red laser at 689 nm

The red laser system is used for the 3D red MOT and for probing as it is sketched on figure IV.12. To cool on a narrow transition, we need a precision over the laser frequency that is impossible to obtain with the previous locking scheme. The study and applications of ultra-narrow lasers is a whole field of research on itself, it is technically challenging and fundamental for testing theories in physics. An interesting review on ultra-low noise lasers and their applications can be found in [145]. Several strategies can be implemented to narrow-down the bare linewidth of a diode laser. At the level of the light source, the use of an extended cavity diode laser (ECDL) of length L =10 cm narrows the laser spectrum of a factor L^{-2} [146] and limits the noise due to spontaneous emission [147]. The idea of ECDL, for a continuously tunable single mode laser was introduced by Littman and Metcalf [148]. The ECDL is in a Littrow configuration. In this configuration, the laser diode (gain medium) gives a diverging beam which is collimated and sent on a diffraction grating. The diffracted light is retro-reflected[20] back toward the gain medium which enables wavelength-selective feedback. The lasing threshold is optimized by mode matching (auto-collimating) the diffracted beam back into the diode. The disadvantage of this configuration however, arises from the change of angle of the laser output beam when tuning its wavelength. We have under optimal conditions a intensity threshold of $\sim$ 55 mA. At the output of the laser, two optical isolators of 60 dB and 30 dB that ensures the absence of parasitic optical feedback in the diode. The laser having then a linewidth below 1 MHz and needs further refinement. At this point, the linewidth is limited by the cavity length, spontaneous

---

[19] Jean Peltier (1785-1845) a French watchmaker found in 1834 that, when an electrical current passes across the contact between two different conductors in a circuit, a temperature difference would appear.

[20] The grating in external cavities combine the function of filter and external mirror.

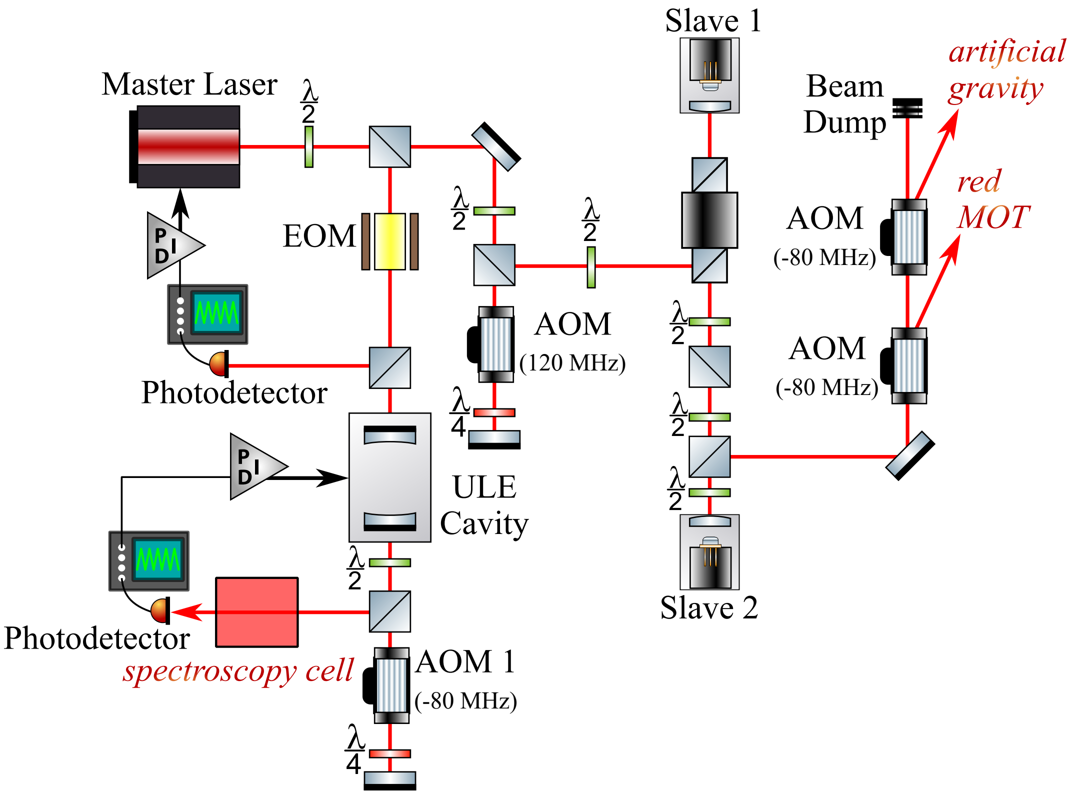

Fig. IV.12 *Optical setup for the 689 nm "red" laser.*

emission noise, mechanical vibrations and temperature variations.

The frequency narrowness is improved by performing a frequency lock on a high finesse (F=3000) Fabry-Pérot (FP) cavity. The cavity itself is made in ultra-low expansion glass (ULE), a type of glass with a very low coefficient of thermal expansion with many applications ranging from laser cavities to the Hubble telescope's mirror. The FP cavity is under vacuum and mounted on viton[21] chocks to isolate the cavity from acoustic perturbations. To additionally isolate the FP cavity from environmental perturbations, it is sealed in a vacuum chamber at a pressure below 10^{-8} mbar and attached to a double layer stabilized in temperature at 30°C. The locking follows the Pound-Drever-Hall (PDH) stabilization approach (see original development ref. [149]) which corrects actively the laser frequency to match the minimum reflection condition of the FP cavity. Although the cavity is near perfect, two main sources of noise cannot be suppressed and limit the final linewidth of the laser: the thermal noise and the shot noise. Lately in [150], by means of PDH locking scheme, narrow linewidth below 40 mHz have been demonstrated where the cavity is a single piece of a silicon of zero thermal expansion coefficient. Recently in [151], this same single-piece cavity was used in the design of the sharpest laser built with the astounding linewidth of 10 mHz. Our laser does not require to operate

---

[21] A type of rubber band, use in extremely aggressive chemical and temperature conditions.

at such regime and under actual conditions has a width about 500 Hz and a daily variation below 10 kHz which is suitable to address the Γ_r=7.5 kHz wide $^1S_0 \rightarrow ^3P_1$ transition.

The laser spectrum has been narrowed to a satisfying level, however the FP cavity is subject itself to a slow thermal drift of approximately 10 Hz.s^{-1}. This long-term drift is followed and compensated by a saturated fluorescence spectroscopy on the $^1S_0, m = 0 \rightarrow ^3P_1, m = 0$ transition while applying a bias field of 10 G to repel the magnetic sub-levels. The probe beam is characterized by a beam waist of 10 mm and a power of 150 μW. The AOM 1 on figure IV.12 is on a double-pass configuration and allows one to scan the laser frequency. The atomic and laser beams for the spectroscopy are -as for the blue spectroscopy- in a Doppler-free configuration at 90° of each other. If however, the main component of the speed is not accounted for the Doppler broadening, the spectroscopy linewidth is increased due to the transit time of the atoms in the probe beam. The fluorescence photons are collected thank to two large numerical aperture lenses which collimate and guide the signal to a photodetector. The linewidth of the fluorescence spectrum is further increased by power broadening up to 140 kHz.

The error signal is generated by taking the difference with the photodetector signal while the frequency of the AOM 1 is swept back and forth with a 140 kHz frequency step. This error signal is digitalized and sent to a numerical PID controller before being interpreted in terms of frequency offset and sent as a feedback loop to compensate the drift of the FP cavity. Additionally, this frequency adjustment is broadcasted on the local network to several Direct Digital Synthesizers (DDS) which convert the digital signal into a radio-frequency (RF) signal used by the different AOMs to actively correct the slow FP cavity drift. The efficiency of the overall locking scheme is tested by absorption spectroscopy on the red MOT. The remaining frequency uncertainty is ± 5 kHz.

During the experiment, not only stabilizing the frequency is necessary. During the first phase of the red MOT (see Figure IV.2.5), the frequency of the red beam is swept over 2 MHz using the DDS box addressing the AOM 1. Double-pass configuration ensures a minimum of deviation of the beam while sweeping its frequency.

IV.3.3 Dipole trap laser

Two near infrared lasers are used for the 2D gravity experiment. The first one consists in a Ti:Sapphire[22] (TiSa) commercial laser used to trap horizontally the atoms in the correct geometry and is kept running during the collapse. This laser refers to the optical dipole trap (ODT) described in section IV.2.6. A second near infrared laser is used vertically to further compress the atoms at the center of the first trap. This laser is turned off at the beginning of the 2D gravity sequence.

---

[22] Titanium-sapphire lasers are tunable lasers between 650-1100 nm. They are of great interest for their ability to generate short pulses and being continuously tuned.

The ODT laser consists in a frequency doubled Nd:YAG[23] pump laser that delivers continuously 16W to the titanium-crystal sapphire which converts the green light (532 nm) into the desired wavelength (generally thank to a birefringent tuner in the laser resonator). The TiSa laser delivers 1.3 W at the magical wavelength of 925 nm. The beam profile is very clean ($M^2 < 1.1$) and is mode-matching well the fiber coupler (∼90% injection) that leads to the science chamber; However, to control the beam, we use an acousto-optic modulator (AOM) as shutter. The first order injects the fiber coupler up to 0.95 W and the zero order is sent to an optical beam dump.

Regarding the frequency tuning and locking of the Ti:Sa, the laser spreadsheet predicts a spectral linewidth of ≤50 kHz which is satisfying with regard to the magical wavelength configuration. Indeed, the additional light-shift generated is well below the Doppler broadening of the transition anyway.

IV.4 Imaging system

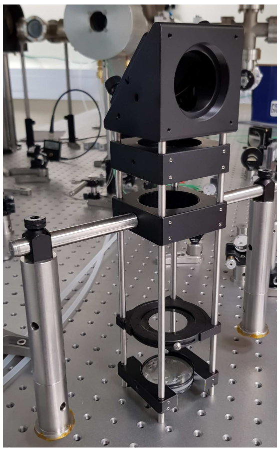

Fig. IV.13 *Staged telescope made of 2 aspheric lenses (f=100 mm, NA=0.20).*

The gravitational collapse was expected to give rise to unusually shaped stationary distributions (see [41]) and of small details that only a high resolution microscope objective may be allowed to see. We could not place the camera and objective directly that close from the science chamber. We thus had to design a large numerical aperture (NA) optical system to extract the fluorescence signal away from the science chamber up to our microscope objective and camera. We chose a set of two large numerical aperture (NA_{lens}= 0.20) aspherical lenses, being placed a

---

[23] Neodymium-doped yttrium aluminum garnet is a crystal which delivers 1064 nm IR and is frequency doubled in a doubling medium such as $LiNbO_3$, LBO or KTP.

centimeter away from the science chamber quartz window. The microscope objective (5x Mitutoyo Plan Apo Infinity Corrected) having a numerical aperture of $\mathrm{NA}_{obj} = 0.14$, we were ensured to take advantage of the diffraction limited resolution[24] $\approx 2\mu$m. Figure IV.13 shows the telescope fully mounted. Figure IV.14, on the left, shows a picture of the 1:1 telescope + mirror rectifying the fluorescence signal direction to send to our objective and camera. On the right side of the Figure, is shown CCD imaging of our 1951 USAF target resolution test, the last two groups of lines are shown. We verified that the maximum resolution of the objective is conserved throughout the telescope. We also added an iris to the telescope in order to reduce spherical aberration. The trade-off between spherical aberration and numerical aperture, changes in the end the resolution. The effect of the iris on the spherical aberration was determined also thank to the lens equation given by its manufacturer, calculation shows a loss of 0.5 μm in the resolution due to spherical aberration. However, the two methods (calculation from lens equation and direct measurement) always led to a resolution loss when closing the iris, indicating that the numerical aperture loss was stronger than the spherical aberration win. We thus kept the iris always open during the imaging sequence.

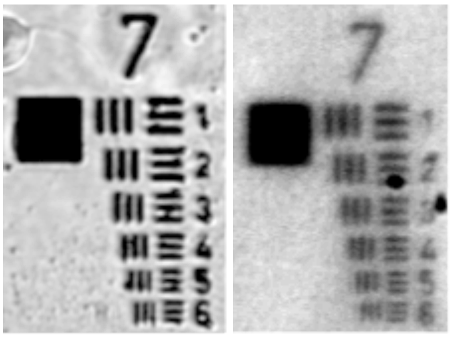

Fig. IV.14 *Resolution test of our objective, without (left) and with (right) the telescope. The resolution is maintained at $\approx 2\mu m$ either way.*

IV.5 Imaging method

The imaging consists in a vertical fluorescence as depicted in Figure IV.15, the blue probe addresses the 461 nm transition. Because this resonance is broad ($\Gamma_b \approx 32$ MHz), the fluorescence signal is strong and allows to image the atomic cloud on short time scales of typically 5-10 μs. The experiment followed by the fluorescence imaging can be separated in two different times: after loading the atoms in the ODT, the 2D gravity beams are turned on for an experiment time $t_{\text{exp}} \in [0, 100]$ ms, then turned off. After a time $t_{\text{delay}} \in [0, 300]$ ms, the blue probe is turned on,

---

[24] Equal to $\lambda/2\mathrm{NA}_{obj}$ with $\lambda = 461$ nm.

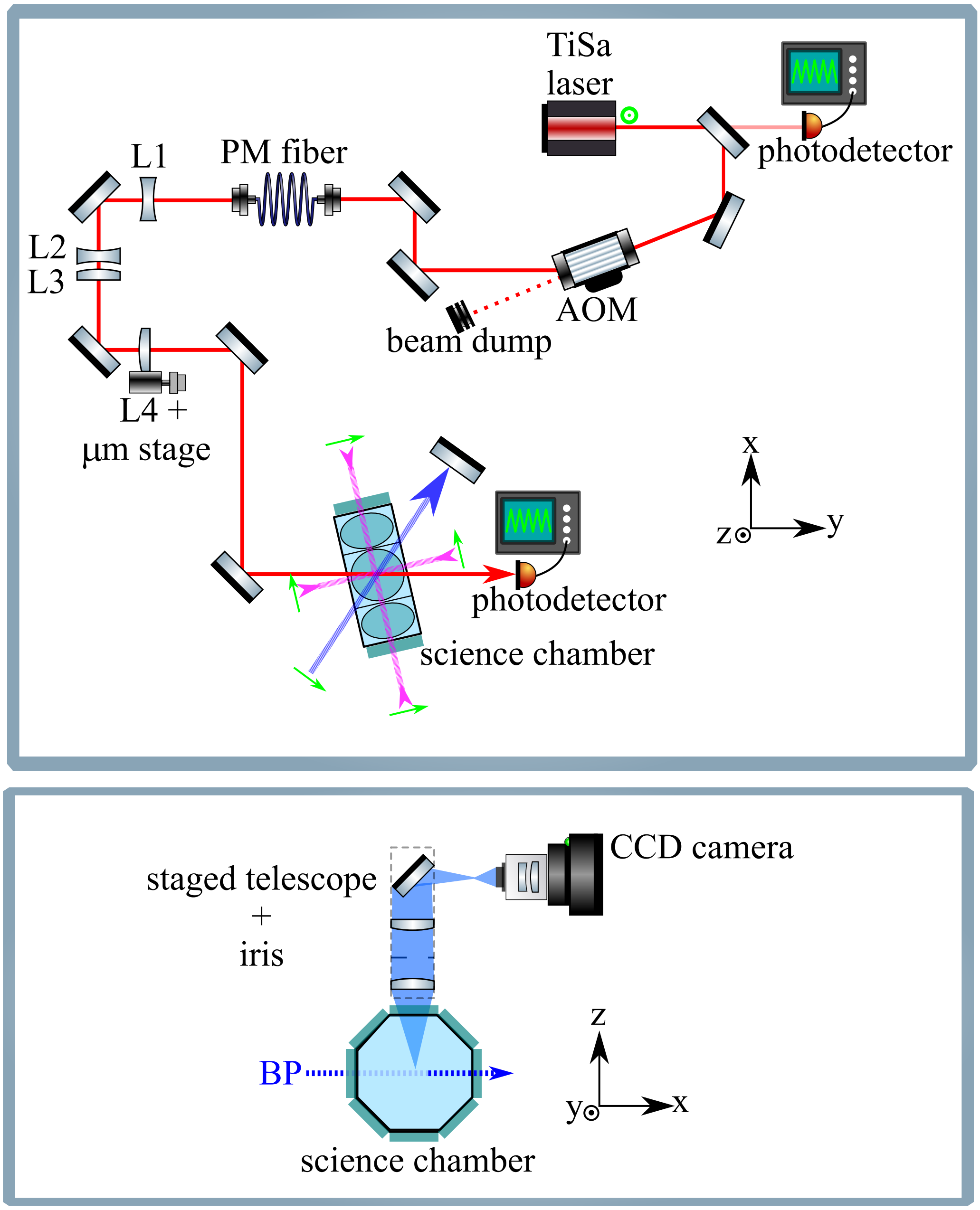

Fig. IV.15 *Schematic representation of the experiment (upper panel) and imaging system (lower panel). A cloud of cold strontium-88 is prepared in a magneto optical trap in the science chamber. The cloud is then loaded into a pancake shaped dipole trap (red). A set of 4 contra-propagating laser beams (pink) address the 7.5 kHz intercombination line and create a 2D gravity in the plan of the pancake. A blue probe (blue) is shined in-plane and the fluorescence signal is gathered from a vertical system of lenses and a high-resolution microscope objective. The closest lens is at the limit of the vacuum chamber to have the largest possible fluorescence signal. NB: (green) beam polarizations.*

making the atoms fluoresce which allows to take a picture of them using a high-resolution objective mounted on a CCD camera. Each measurement of this type is destructive since the fluorescence occurs everywhere in the cloud and ends up heating the system.

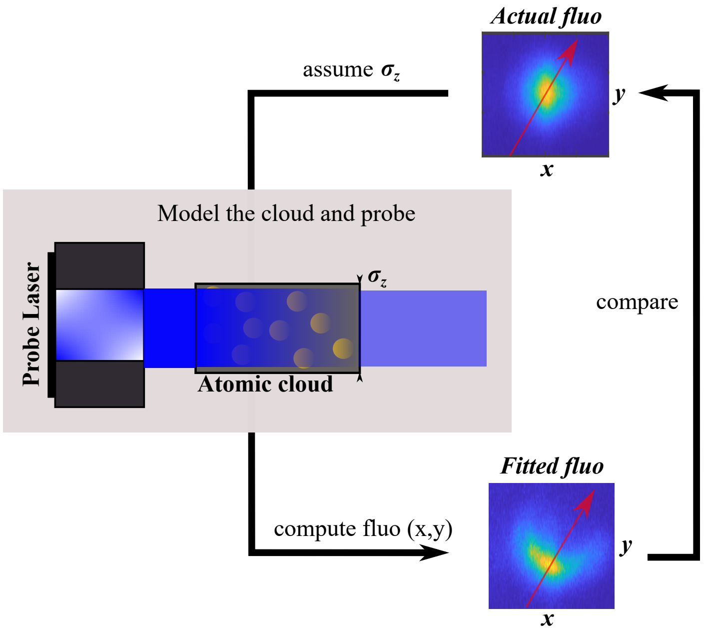

Fig. IV.16 *Fitting the cloud thickness σ_z. Probe direction of propagation given by the red arrow. The actual fluorescence is compared with a Fitted one deduced from a guess on the cloud thickness.*

Since we look from the top of the ODT most of the information in the xy plane can be recovered: total number of atoms N, in-plane cloud sizes σ_x, σ_y and temperature T. The number of atoms is obtained by previously calculating a conversion factor between the measured fluorescence and the number of atoms. This factor being obtained by comparing the results of an absorption imaging and a fluorescence imaging. The absorption imaging yields the atoms number and the fluorescence to a photon count on our CCD camera. Having this conversion rate allows us to avoid having to repeat an absorption imaging each time we are measuring the atom number.

Indirect measurement and numerical methods allow to recover information along $\hat{z}$ if a weaker ($s \ll 1$) probe is used. As shown in Figure IV.16, we can fit the cloud thickness σ_z using a weak blue probe. Thus in practice, each experimental run (given $\delta, s_0, t_{\mathrm{exp}}$ etc.) is repeated twice: once with a strong saturating blue probe that gives access to the total number of atoms N and the number of atoms integrated along $\hat{z}$: $\bar{N}(x, y)$ which is total number of atoms at a pixel location (x, y). The second measurement is realized with the non-saturating probe and gives a fluorescence signal that can be written as

$$\mathrm{fluo}(x, y, \sigma_z) \propto \int \mathrm{d}z \; I[\bar{N}(x, y, z, \sigma_z)] \; \bar{N}(x, y, z, \sigma_z), \tag{4.1}$$

where we assumed that each pixel that radiates vertically as the product of the intensity multiplied by the atom density. The integral is required to account for the vertical dimensions of the ODT. We further assume the cloud vertical dimension to be a Gaussian of RMS σ_z. Since we know $\bar{N}(x, y)$ and the probe properties, we vary σ_z numerically and fit the fluorescence signal with the one generated numerically with the help of Equation 4.1. When the two are matching, we retain the value of σ_z and use it for the calculation of the optical thickness.

Chapter V

2D gravity: Experimental results

This chapter is devoted to the results of the 2D gravity experiment plus alongside discussions. After modifying the initial setup by adding a vertical dimple to the atomic cloud in Section V.1, we will jump into the detailed results of the 4 beam configuration in Section V.2. Special attention is devoted in explaining the compression factor measurement in Section V.3. Other beam configurations were also studied in Section V.4.

V.1 Experiment parameters and addition of a dimple

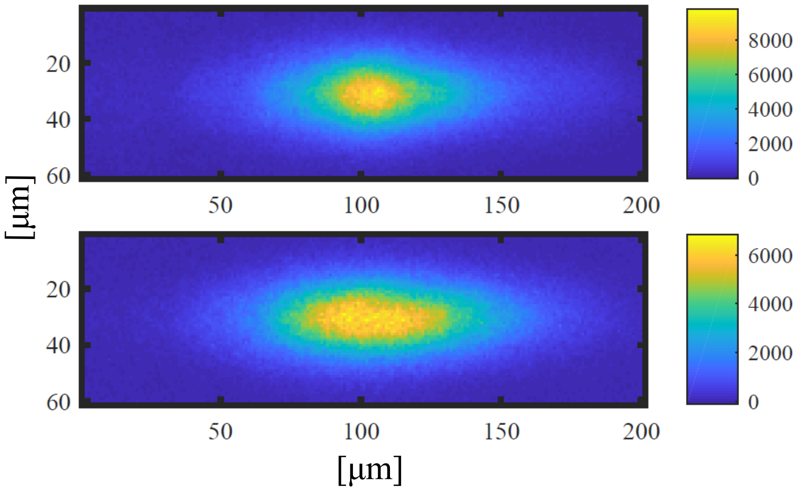

Fig. V.1 *Fluorescence images respectively with (top) and without (bottom) the presence of the dimple. The dynamical time is expected to be reduced with the dimple and overcome atom losses.*

Since the initial model discussed in Chapter II Section II.3 was neglecting multiple scattering, we decided to play around the experimental parameters determined in

Chapter III. Namely, we played around the experimental parameters: a number of atoms of few 10^5 atoms, a detuning about -4Γ and a saturation parameter about 1.

For those parameters, we observed a compression when turning on the 2D gravity: the fluorescence of the cloud center becoming stronger during the first milliseconds of the experiment. But we also suffered important atom losses, the integrated fluorescence signal decreases as soon as the 2D gravity is on. What happened is to be understood as follows: picture yourself handling a pack of snow and say you wish to make a snowball out of it. If you have very hot hands, the snow will melt rapidly before you even compress the snow but being fast and strong enough you may increase the density on the boundary of the pack of snow. To try to make it work, we thus decided to use a denser initial cloud: we started the experiment with more atoms located at the center of the trap. By doing so, we expect to need less time to compress fully the system. We subsequently tried to reduce the dynamical time by reducing the initial size of the atomic cloud, it was realized by adding an extra vertical ODT in the far infrared. Figure V.1 shows the effect on the atomic cloud of the addition of a vertical ODT, also called a *dimple*. This dimple beam was turned on at the same time as the ODT but turned off at the beginning of the 2D gravity experiment. As the size of the system was then initially smaller, we expected the collapse to occur quickly. The addition of the dimple allowed us to see larger compression when the 2D gravity is on, however the rapid "melting" of the cloud is still present as we will see in forthcoming Section V.2.2.

V.2 4 beam configuration

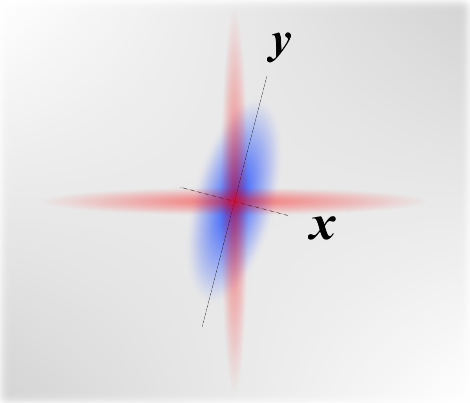

Fig. V.2 *4 beam configuration. (blue) ODT/atomic cloud position. (red) Artificial gravity incoming directions.*

The 4 beam configuration is represented Figure V.2. The ODT propagating along $\hat{x}$, we have the $\hat{x}$ and $\hat{y}$ axes defined as the proper axes of the ODT and therefore the proper axes of the atomic cloud. The $\hat{x}$ and $\hat{y}$ axes are at an angle of 14 degrees clockwise from the four beam creating the 2D gravity. It was the best that could be done in terms of setup constraint. Another important remark comes along with the previous one concerning the trap shape. Our trap is anisotropic, as schematically represented in Figure V.2 and mentioned in Chapter IV Section IV.2.6. We are thus not in the initial 2D depicted theoretically but we did not see any physical reason for this to impede the collapse.

V.2.1 Center of mass displacement: beam balance

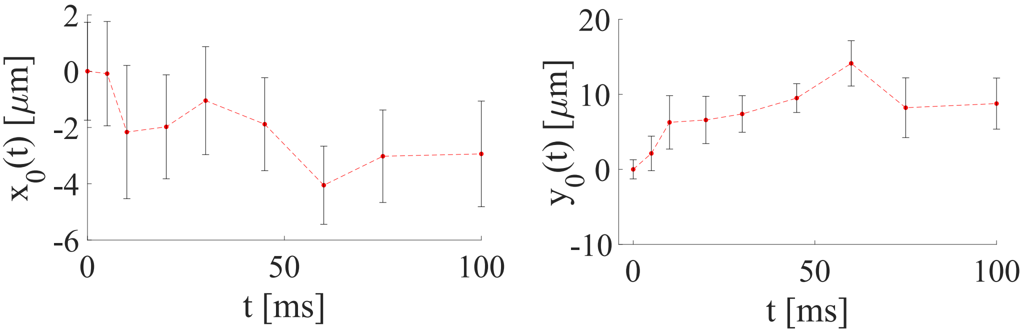

Fig. V.3 *Center of mass displacement along* $\hat{x}$ *and* $\hat{y}$ *during an experiment of* 100 *ms. Data are averaged over different intensities (error bars). [4 beam configuration]*

We need an intensity balance between each beam in order to have the highest critical reduced temperature (as seen in II SectionII.3.2). Also, to minimize the atoms losses, we need to have a perfect balance within *each pair* of contra-propagating lasers creating the 2D gravity. If not, for small imbalance, the cloud center of mass will not match the trap center, defined as the minima of the dipole potential. Higher imbalance would lead to push away the atomic cloud out of the trap and ultimately lead to atom losses. Figure V.3 shows the evolution of the cloud's center of mass position along respectively $\hat{s}$ and $\hat{y}$ for a 100 ms long experiment with the 2D gravity. The initial position fixes the zero of the ordinate axis. The bars are obtained by repeating the experiment for various saturation parameters between $s_0 = 0.1$ to $s_0 = 2$. All series are quite close to each other's, it means that the cloud center remains well localized even under the effect of the 2D gravity. If we compare the displacement of the center of mass with the RMS σ_x and σ_y given in Chapter III Section IV.2.6, we found negligible drifts of the cloud's center, about 8% in both directions in the plane, which is a good indicator of the intensity balance within each pair. Also, beam balance along the two different axes is realized by imaging the beams and measuring their power, they are under 10% giving the same saturation parameter.

V.2.2 Atoms number and lifetime

To maintain an important 2D gravity intensity for a time long enough to see the system collapsing, we need to minimize atoms losses. Our first concern was thence making the atoms characteristic lifetime long enough. We observed for various detuning and intensities, an exponential decay of the atoms number. The exponential decay is characteristic of single-particle losses [67] such as heating (spilling atoms out of the trap) or background collisions due to imperfect vacuum. We fitted $N(t)$ for a 100 ms measurement and extracted the characteristic lifetime τ of our atomic ensemble. Assuming an exponential decay of the number of atoms we have:

$$N(t) = N_0 e^{-t/\tau}. \tag{5.1}$$

We fitted the atoms number time evolution with the $N(t)$ function of Equation 5.1.

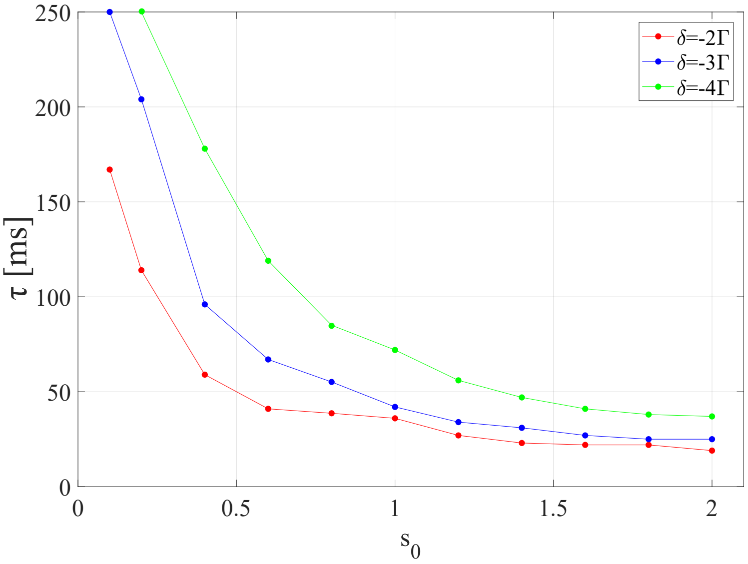

Fig. V.4 *Atom lifetime τ in the dipole trap under a given saturation parameter and detuning of the gravitational beams. Error bars (below 10 ms for $\tau \leq 100$ ms) not represented for more readability. $N_0 = 3 \times 10^5$ (top), $N_0 = 1 \times 10^5$ (bottom). [4 beam configuration]*

Figure V.4 gives the mean lifetime τ of our atomic cloud for $N_0 = 3 \times 10^5$ atoms. Each curve is the result of an averaging of 10 repetitions of the experiments. We varied the saturation parameter and detuning of the gravitational laser beams according to the axes and legend. Since the experiment duration t_{exp} was not longer than 100 ms, we should be careful regarding lifetimes exceeding this value, as a consequence data of saturation parameter above 0.5 have a statistical uncertainty of $|\Delta\tau| \approx 10$ ms and below have larger uncertainty. The dramatically short atom lifetime required investigation since without shining the 2D gravitational beams, the atoms in the ODT have a lifetime of several tens of seconds. This order of magnitude is mostly dictated by the background collisions due to the imperfect vacuum environment. The first idea that comes to mind is that, without any cooling in the vertical direction, the vertical heating due to spontaneous emission is the dominant mechanism at the origin of atoms losses. Since the 2D gravity is actually an optical molasses, we can consider the temperature to be close to zero in the xy plane. But along $\hat{z}$, nothing forbids the temperature to increase. If we consider a heating rate given by the transition scattering rate $\frac{\Gamma}{2}s_\delta$ and a simplified re-emission probability of 1/3 along $\hat{z}$. We then have the temperature increasing along $\hat{z}$ as:

$$\frac{\mathrm{d}T}{\mathrm{d}t} = T_r \frac{4}{3} \Gamma s_\delta, \tag{5.2}$$

with $T_r = \frac{(\hbar k)^2}{2mk_B} = 230$ nK the recoil temperature. Actually, an additional factor 2 comes from the fact that spontaneous emission is treated here as a random walk. Then for a trap depth $U(\mathbf{0})$, the characteristic atoms lifetime is about

$$\frac{U(\mathbf{0})}{k_B} \bigg/ \frac{\mathrm{d}T}{\mathrm{d}t}. \tag{5.3}$$

It turns out that the trap depth deduced from the atom lifetimes is of the same order of magnitude of the trap depth obtained by studying the trap frequencies and waists (see Chapter IV Section IV.2.6, b)). Both methods give consistent results.

The importance of atom losses on the dynamics of the collapse was not anticipated. Whether or not those losses are truly impeding its observation can be answered by evaluation of the collapse dynamical time and compare it with the atom lifetime. We recall that the dynamical time for self-gravitating systems is defined as the characteristic time for crossing the system, *i.e.* the characteristic size L of the system divided by the average atoms thermal velocity $\bar{v}$. Since the 2D gravity lasers are fixing the temperature T of the atomic cloud, we assume the mean velocity of an atom to be $\sqrt{k_B T/m}$. We found that the dynamical time is of several tens to 50 ms. Thus, the mean lifetimes τ given in Figure V.4 are comparable with the expected collapse characteristic time.

Due to those unwanted atoms losses, we cannot rely only on the cloud density to characterize the collapse transition. Indeed, as the atoms escape the trap, the optical thickness reduces and consequently the 2D gravity reduces. Only if $N(t)$ was constant, it would be useful to solely look at the RMS or density. We chose rather to characterize the system by looking at the optical thickness and compression factor that will be defined below. For the calculation of the optical thickness we are required to calculate the atom temperature.

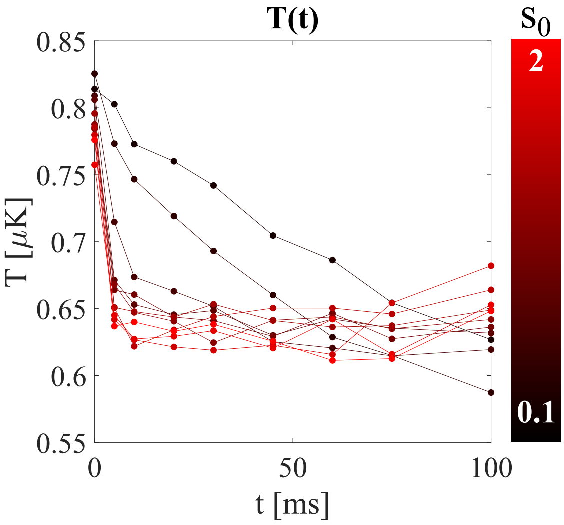

Fig. V.5 *In-plane temperature time evolution for* $\delta = -4\Gamma$ *and* $N_0 = 3 \times 10^5$. *[4 beam configuration]*

V.2.3 Temperature

Temperature in an ODT is linked to the trap frequencies by means of the equipartition theorem according to Equations 3.30. After turning on the gravitational beams for a given time and then switching them off, a simple way to obtain the temperature is to let the atoms relax in the trap for few periods and measure the size of the atomic cloud at equilibrium. We then deduce the temperature consistently with the frequency measured previously. For us the thermalization time was taken 300 ms. It is worth noticing that even if the trap is anisotropic for practical reason, the temperature is the same in any direction in-plane as the gravitational beams have the same saturation parameter and detuning.

We also could have perform the temperature measurement with a time-of-flight, which consists in imaging the cloud expansion after a short delay t_{delay} after turning off the gravitational beams. The cloud at a given temperature will undergo a certain expansion such that its size at a time t is related to the temperature. This technique is convenient if one can observe an atomic cloud at a constant distance from the objective. But since we observe from a vertical axis, the cloud is in free fall when we release it and will go away from the objective. It will follow the loss of focus from our camera, we will thus see the cloud expands faster than it should due to the defocus and consequently measure a hotter temperature than in reality. The time-of-flight could also be done in the harmonic trap created by the ODT. It is possible if the cloud is initially compressed, such that it does not influence[1] the ballistic expansion. In our case, the compression is not large enough to use this method.

---

[1] Actually, it is possible to remove the trap contribution, by modeling it by an inverted Gaussian.

The trap in our situation has determined frequencies and the usage of Equation 3.30 is reasonable. Figure V.5 shows the time evolution of the temperature. For saturation parameters larger than 0.3, the temperature reaches after few milliseconds, its equilibrium value at around ≈ 0.65 μK independently of the saturation parameter.

V.3 Collapse in 2D: characterization of the compression

With the parameters we chose, we expect a compression factor CF about 3 as discussed in Chapter III Section III.1. To characterize the compression, we have several options: looking at the central density, the optical thickness or the cloud size. Because of the unwanted atoms losses, it seems that those three options are going to follow the decrease of the number of atoms. In a lossless case, we guess that the optical thickness would saturate, indicating that the 2D gravity is compressing the atoms at a point where the light does not enter anymore the system and the momentum diffusion is counterbalanced by the long-range force. We also expect the cloud size to reduce under the effect of the 2D gravity and then increase back when it is stopped.

In our case, by taking into account atom losses, we expect rather the optical thickness to saturate after a finite time, reach a plateau and then decrease. Rather than looking at the cloud absolute size, we looked at the compression factors defined as the ratio of the cloud size at thermal equilibrium in the ODT *long after* ($t_{delay} \approx$ 300 ms) the experiment over the cloud size *immediately after* shutting off the 2D gravitational beams. Our attention was thus directed on the optical thickness and compression factors -related to the cloud size- whose expressions are given by:

$$b_i(t = t_{exp}) \propto \int \mathrm{d}x_i n(\mathbf{r}, t_{\mathrm{exp}}) \quad \text{and} \quad \mathrm{CF}_i = \frac{\sigma_i(t \gg t_{\mathrm{exp}})}{\sigma_i(t = t_{\mathrm{exp}})}, \tag{5.4}$$

within each direction $i = x, y$. We present in the next paragraphs the most illustrative curves which were obtained for $\delta = -3\Gamma$ and $\delta = -4\Gamma$. The saturation parameter s_0 was systematically varied between $[0.1, 2]$. For each of those parameters we compared the time evolution of the optical thickness and of the compression factors.

V.3.1 $\delta = -3\Gamma$ and $N_0 = 3 \times 10^5$

The optical thicknesses $b_i(t)$ *at a given detuning and temperature* and the compression factors $\mathrm{CF}_i(t)$ in a direction $i = x, y$ are represented respectively in Figures V.6 and V.7. We see that the optical thickness is decreasing for every intensity but faster for the highest, which is expected. We also see that, even though the initial

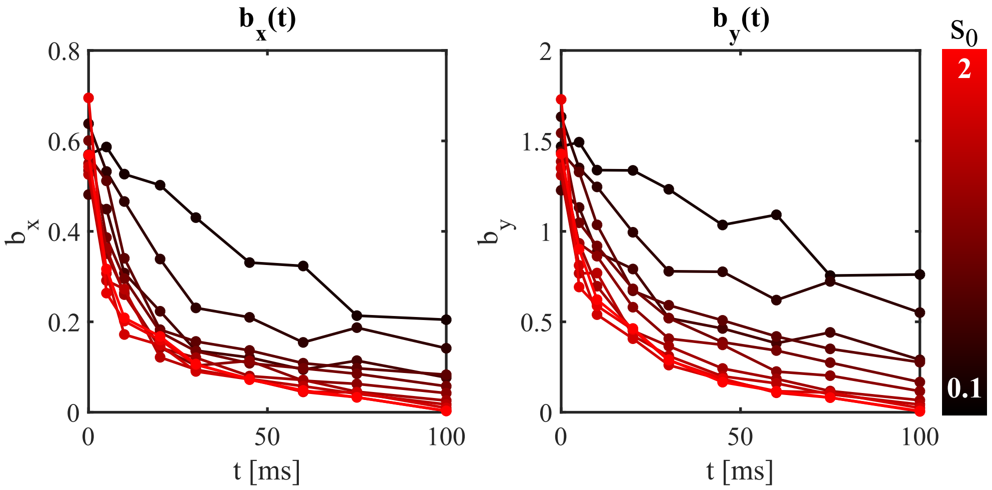

Fig. V.6 *Optical thicknesses time evolution for* $\delta = -3\Gamma$ *and* $N_0 = 3 \times 10^5$. *[4 beam configuration]*

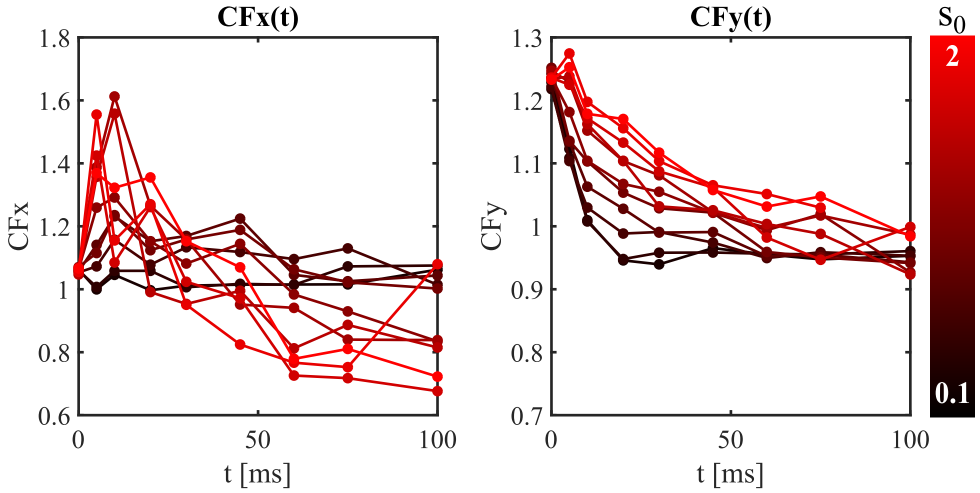

Fig. V.7 *Compression factors time evolution for* $\delta = -3\Gamma$ *and* $N_0 = 3 \times 10^5$. *[4 beam configuration]*

optical thicknesses at $t = 0$ are different along the two directions, they decrease with the same characteristic time, which is reminiscent of a one-particle type of losses. It also shows that the optical thickness does not saturate as we would expect in the collapsed phase. It means that the compression factors we obtain are not limited by the optical thickness.

The compression factor shows evidence of compression for $s_0 \geq 1$. We also see that the compression factor does not maintain itself at its maximum values ~ 1.55 along x and ~ 1.25 along y. This decrease is a signature of the gravitational force: the more atoms are lost, the more the force decreases and by incidence the more the compression reduces. One would note that the compression factor is non-zero even at the very beginning, even before the 2D gravity produces its effects. It is because of the presence of the dimple (see V.1) that is released at the beginning of the experiment, so that the atoms are initially in a compressed configuration. Although, even if along y we do not see any compression or a small bump at the beginning, we see a clear compression along x. The discrepancy between the two directions originates likely from the differences in optical thicknesses. Since this last one is below one along $\hat{x}$, the cloud is more likely to show compression than along $\hat{y}$ where it is above one.

V.3.2 $\delta = -4\Gamma$ and $N_0 = 3 \times 10^5$

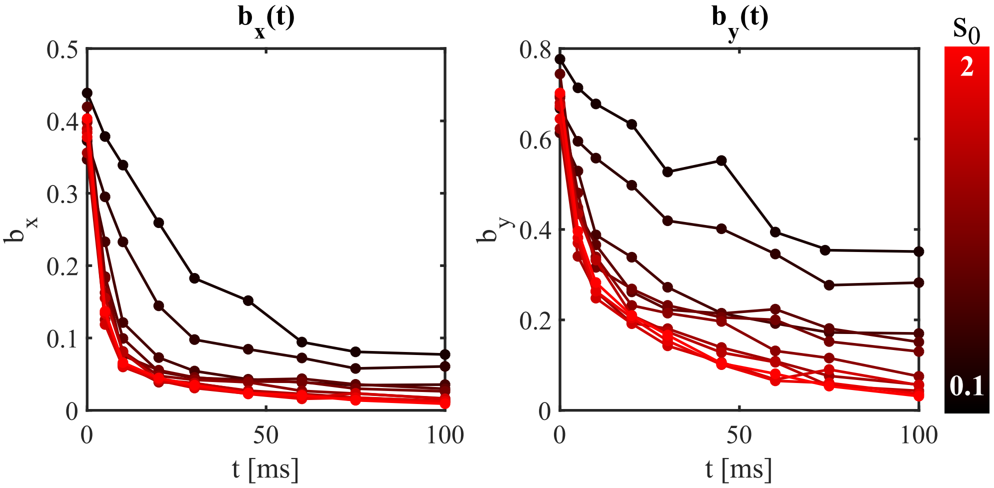

Fig. V.8 *Optical thicknesses for $\delta = -4\Gamma$ and $N_0 = 3 \times 10^5$. [4 beam configuration]*

Repeating the experiment with the 2D gravitational further red-detuned reinforces our certitude on the gravitational origin of the observed compression. First, the overall optical thickness is lower and the compression factors as well. Again, those two are correlated because the 2D gravitational force is directly proportional to the optical thickness. While along x, the compression remains, we have suppressed any chances of compressing along y.

V.3.3 Addition of a vertical cooling beam

In order to minimize the atoms losses, we repeated each of our measurement with a weak vertical cooling during the total duration of the experiment. The beam creating the cooling is simply the vertical axis of the MOT but used at a lower intensity ($s_0 = 0.1$ and $\delta = -4\Gamma$). The choice of intensity for this beam is critical, if it is too high it will compete with the 2D gravity and corrupt the experiment. Another intrinsic problem alongside the competition with the 2D gravity is the

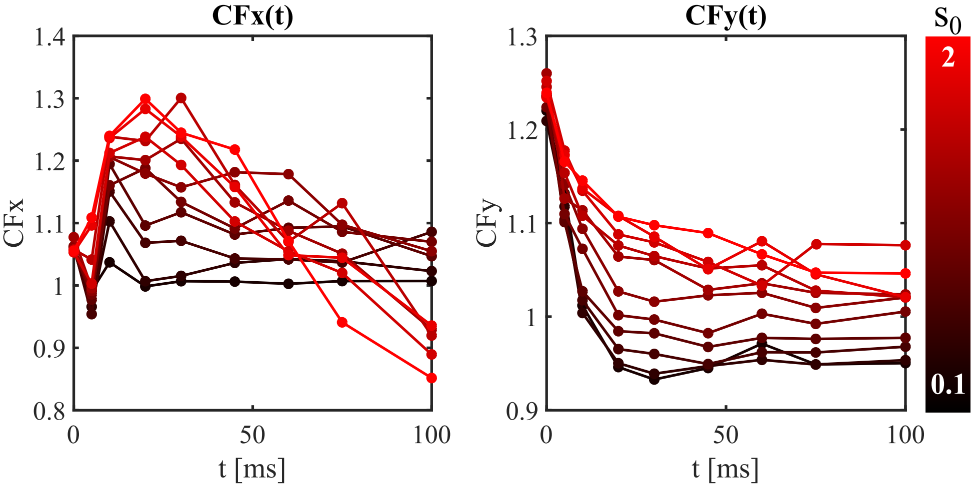

Fig. V.9 *Compression factors for $\delta = -4\Gamma$ and $N_0 = 3 \times 10^5$. [4 beam configuration]*

multiple scattering generated by the vertical cooling. For the MOT beam which is incident at 90 ° with the trap plan, the scattered photons re-emitted by spontaneous emission will be more likely emitted in plan and will increase the in-plane repulsion. We expect however the benefits from maintaining a high number of atoms will dominate over the disadvantages coming from the increase of the in-plane repulsion.

The effects of the vertical cooling are multiple. By adding the vertical cooling, we extended the atoms lifetime. We specifically tuned the power of the vertical cooling by looking for this result. In practice, we repeated the experiment over the maximum duration $\sim$ 100 ms and tuned the vertical power until we see a maximum fluorescence signal. We specifically aimed at improving the $\delta = -3\Gamma, -4\Gamma$ and the high number of atoms ($N_0 = 3 \times 10^5$) curves because they were the most promising in terms of compression.

We obtained an improvement of the optical thicknesses as compared to the same runs without the vertical cooling. We even see the optical thickness along y saturating over few tens of milliseconds. We thought it meant a stationary regime of 2D gravity but got disappointed when looking at the compression factors. We are even surprised at first to obtain compression factors that are for the majority less than one, which has to be explained in terms of balance between multiple scattering from the vertical cooling and the 2D gravity. This time indeed, the vertical cooling beam generates multiple scattering most likely in the plane and is a source of repulsion/heating.

Another problem arises from the addition of the vertical cooling. The trap shape is highly deteriorated compared to the vanilla case without the vertical cooling. While in the latter case, the cloud remained nicely elliptical, the former case -with cooling- seems to twist the cloud shape. As a result, the cloud is not anymore Gaussian, and it becomes harder to extract a clean RMS. The shape of the cloud seemed to react to the polarization of the vertical cooling beam, it suggests in the end, that the cooling was inhomogeneous and let probably to a complex force landscape. This last point was again not in favor of the vertical cooling. This is why we abandoned this idea.

V.3.4 Intermediate conclusion

The 4 beam configuration has showed evidence of the long-range force; However, we were limited by atoms losses. The compression factors with the 2D gravity are at most about 60% and are comparable with the compression factors obtained experimentally in the 1D case. This cannot be improved by adding a vertical cooling, because it modifies the system in a too complex way to be then simply described by a 2D gravity. If we want to stick to the initial experiment, a solution would be to use a deeper trap. This was the limiting factor due to technical issues on our TiSa laser.

The choice of parameters for the experiment were constrained by the power of the dipole trap. One could imagine taking a larger number of atoms, which we could not, or it would make us leave the low optical thickness regime that was assumed in the derivation of the artificial gravity. By no means, taking less atoms would improve the chances to see the collapse: it would require then a detuning closer to resonance and longer durations of experiments. The best option in our opinion would be to use deeper dipole traps. The realization of a 2D gravitational collapse is not out of reach but appears constrained technically.

We also repeated those measurements for different beam configurations with 3 and 6 beams. It is the object of the next section of this chapter.

V.4 Other configurations

It is suggested in [152] that the 2D gravitational collapse might depend on the number and angle of beams. In this theoretical paper, the Brownian diffusion of a particle is bounded in space by a wedge of angle α. When the particle collides with the wedge, it is deflected at a chosen fixed angle β. If α is more than 90° the particle never reaches the wedge's corner. If the result generalizes to our system, it would indicate that the 2D collapse is depending also on the number and angle of beams. The minimum number of beams required to observe the phase transition should be not less than 4 and they should be separated by angles of less than 90 °. If two beams in-plane are separated by a larger angle, the sector becomes an escape direction for the particles. We thus modified the beam configuration, by keeping the same saturation parameter per beam. The 3 beam configurations are represented Figure V.10, both configurations give the same results. The 6 beam configuration is represented Figure V.11.

Results from repeating the 2D gravity in different beam configurations strongly

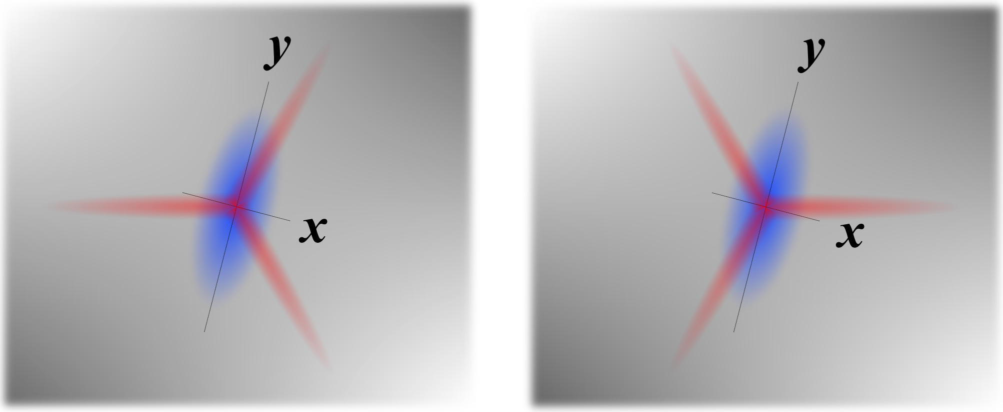

Fig. V.10 *3 beam configurations with positions of the different beams.*

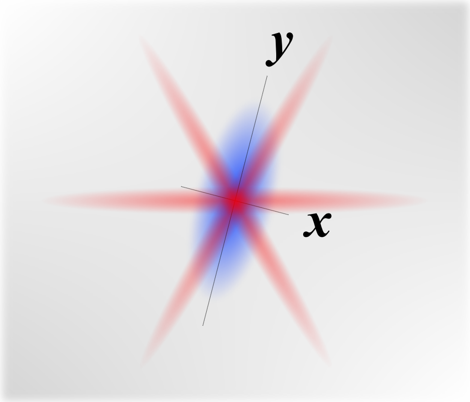

Fig. V.11 *6 beam configuration with positions of the different beams.*

indicate an additional unwanted detuning of the 2D gravity beams: the atoms lifetime is much longer in the 3 and 6 beam configurations, there is also no compression or very late. There is no such thing except if the 2D gravity beams are redder detuned than expected. The explanation we found was that the ODT laser was not anymore at its magical wavelength. Wavelength λ and power P are related by the $P(\lambda)$ manufacturer curve. If we follow this curve, the loss of power we experienced suggests that the wavelength we were working at, was above the magical wavelength. Above λ_M, the trap is further red detuned, leading likely to longer atom lifetimes. As shown schematically on Figure V.12, the red detuned 2D gravity beams are even more red detuned at the trap center. It is however difficult to verify quantitatively this hypothesis without a clear knowledge of the ODT spectrum. After sending the laser to the manufacturer for overhaul, it turned out the solid etalon was faulty. As such, the first stage of the laser locking was not working properly: the frequency of the laser was off and unstable.

Also comparing directly the atom lifetimes in the different configurations, sug-

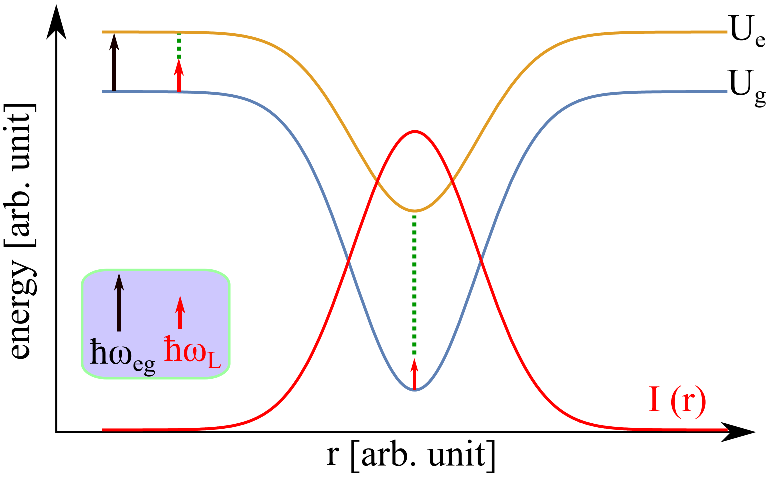

Fig. V.12 *Ground state and excited state potentials for a non-magical wavelength configuration. The detuning (green dotted) is larger in the trap center and photon absorption is more likely to occur at the edge of the trap. Overall, less photon absorption occur as the lasers are redder detuned.*

gests an approximate additional red detuning of about -2Γ for the 3 and 6 beam configurations. We cannot conclude further on the beam configuration dependence of the 2D collapse.

V.5 Conclusion

We saw in the 4 beam configuration a 60% compression along the small direction $\hat{x}$ and a compression of about 25% along $\hat{y}$. The compression observed takes values close to that of the 1D collapse [28]. However, our maximum compression does not come from a saturation of the optical thickness as we always see this one reducing. We have no way to conclude on the maximum compression we could get. However, recent simulations realized by Alain Olivetti, taking into account multiple scattering and evaporation give compression factors very close to those obtained experimentally. The question of the feasibility of a true collapsed phase in 2D remain thus open.

While the experiment led to think that the 2D collapse is possible with the 4 beam configuration, we were limited technically by the faulty ODT laser. Despite the technical issues, we identified the different regimes and nature of compressions we observed. We hope it will encourage other teams to reproduce the experiment. The two crucial elements that would guarantee the success of the experiment are the following. First, the atoms lifetime that needs to be longer than the dynamical time of the collapse. The trap depth must thus be larger than in our experiment. Secondly, the trap must have a disk shape to ensure that the atoms are not tempted to align along the loose direction and recreate a 1D configuration.

Chapter VI

A minimal two-dimensional Brownian motor

The experiment on the 2D gravitational collapse has led us to another very general question, such as the importance of the intensity imbalance between the different axes. Since the temperature along one axis is given by the laser intensity and detuning, it is natural to wonder the effects of an intensity/temperature mismatch between the x and y axes. Alongside this difference in temperature, we recall that for technical needs we had also a mismatch between the 2D gravity axes and the trap proper axes. Those two broken symmetries recalled us the minimal conditions to obtain a Feynman-Smoluchowski ratchet [153]: a perpetual motion device that converts microscopic fluctuations into a macroscopic work. Of course, the initial ratchet -imagined by Smoluchowski- is not realistic because it breaks fundamental laws of thermodynamics. However, the conversion of fluctuations to work describes simply a motor and is legitimate. The fundamental idea of a motor is to take advantage of a flux of particles originating from a difference in temperature or in chemical potential for instance and introduce an asymmetry which will direct this flux into a precise direction (see *e.g.* [154, 155]). It is an example of voluntary symmetry breaking: from isotropic fluctuations to work. Figure VI.1 shows how a simple beam/trap configuration from the previous experiment can lead to work. For configurations with 4 beams, they are equivalent to two thermal baths in contact with the x and y directions independently. If additionally, the beams have the same waist, detuning and polarization, they lead to thermal baths with the same temperature. In this case, the two axes in green are mirror symmetry axes of the N particles stationary state: there is thus no net flux of particles through those axes and the mean angular momentum is zero:

$$\langle \mathbf{r} \times \mathbf{v} \rangle = \sum_{i=1}^{N} \mathbf{r_i} \times \mathbf{v_i} = 0. \tag{6.1}$$

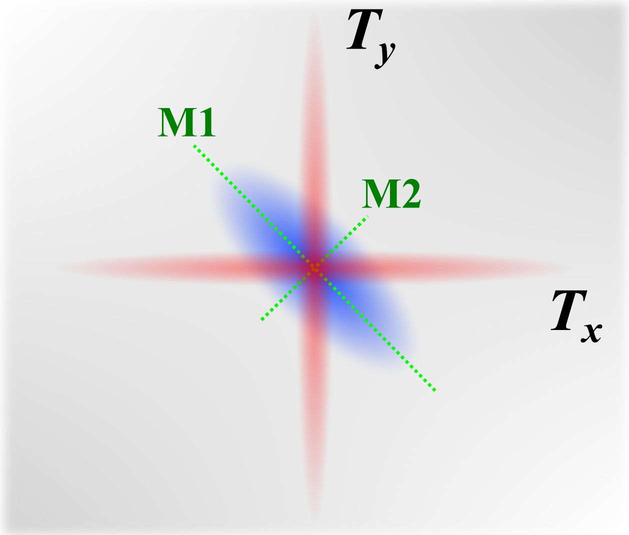

Fig. VI.1 *4 beam (red) configuration with a tilted trap (blue). Axes M1 and M2 are mirror symmetry axes for $T_x = T_y$ and anti-symmetry mirror axes for $T_x \neq T_y$.*

On the other hand, when the beams along x and y have different properties, they lead to different temperatures. The green axes become anti-symmetric mirror axes and it may lead to a non-zero angular momentum. It is a necessary condition to have this anti-symmetry but not sufficient to show that $\langle \mathbf{r} \times \mathbf{v} \rangle \neq 0$.

A simple theoretical description is possible for this problem, in terms of a Langevin dynamics with two different temperatures and a parabolic potential. An overdamped version of this model has been already studied by [156]. Their main result is, this simple system exhibits the properties of a Brownian motor: there is conversion of heat flows into directive work, under the condition that $T_x \neq T_y$ and that the potential is anisotropic out of the temperature axes. The latest condition signifying that the M1 and M2 axes are not matching the temperature axes in Figure VI.1, it is ensuring that the two heat baths are coupled and can exchange energy. The importance of this non-vanishing coupling has been studied by [157]. The work proposed here completes the initial idea of [155] to use this simple model as a Brownian motor. This model generalizes the 1D model of [158] where a rod has its extremities in contact with two reservoirs at different temperatures. It was shown in [159] that the validity of fluctuations relations of this system depends on the its initial conditions. This 1D model was generalized to the harmonically bound particle by [160] and for many heat baths by [161]. The more general, underdamped version of the Derrida and Brunet model was studied in [154] shows that variations of this model, including or not Maxwell's demons, requires always a temperature difference in order to have conversion of fluctuations into work. Recently, the multiple heat baths model was generalized to the underdamped regime from which the overdamped limit can be properly taken, as opposed to a direct overdamped approach which does not account for the time separations between the multiple baths and does not lead to the non-equilibrium current.

While, up to the last decade most works on two-temperature dynamics were theoretical, recent experiments have been conducted and confirm the predictions. Two conductors kept at different temperatures and coupled by electric thermal noise have been recently studied and realized experimentally (see respectively [162] and [163]). A similar overdamped system of RC circuits has been studied in [164], where the link between a non-equilibrium current due to the temperature difference and the second principle of thermodynamics is clearly demonstrated. In another experiment (see [165, 166]), two micron-sized particles trapped in water by optical tweezers and of different effective temperatures, show a heat flow proportional to the particle temperature difference. They also accessed the correlation functions and probability distribution of the system and found precise agreement between their model and experiment. A recent review of experimental realizations and theoretical tools characterizing Brownian motors can be found in [167]. This review also discusses perspectives of stochastic thermodynamics on both theoretical and experimental point of views. The standard tools characterizing classical Brownian motors has also been generalized to quantum systems in [168]. It however seems that quantum motors are not of any advantage or superior efficiency as compared to classical ones. More recently, the diffusion of a particle in a 2D periodic asymmetric potential has been studied in [169, 170] where direct transport appears under the condition of a detailed balance breaking that yields to a preferred direction of diffusion.

The work presented here is based on a model proposed by [171] where a particle trapped in an elliptical potential is in contact with two heat baths. Recent works only focused on the overdamped regime and elliptical potentials, see the recent [164] for the theory and [172] for an experimental realization. We recall the exact analytical results in the case of an elliptical potential in Section VI.1 for the overdamped dynamics. We consequently address the underdamped dynamics in Section VI.1.2. The general case of a confining potential is addressed in Section VI.2 by a perturbative approach. The realization of a Brownian motor is shown to be universal in the sense that independent of the details of the confining potential and for any value of the viscosity. It is also universal if considered as depending only on a double symmetry breaking. The numerical simulations that were realized, are in excellent agreement with the previous sections results and presented in Section VI.3. Finally, an experimental realization with cold atoms is proposed in Section VI.4.

This recently published work can be found in [173].

VI.1 Exact analytical case: Harmonic potential

VI.1.1 Langevin and Fokker-Planck equations

We consider a particle of mass m moving in a plane. This particle is subjected to a conservative force deriving from a confining potential $U(x, y)$, a viscous linear force $-\eta\mathbf{v}$ and two stochastic forces $\sqrt{2T_i\eta}\xi_i(t)$. Here, η is the constant friction coefficient, T_i are the temperatures (expressed in energy unit for which $k_B = 1$) along the i axis with $i = x, y$, and $\xi_i(t)$ are uncorrelated Gaussian white noises: $\langle\xi_i(t)\rangle = 0$ and $\langle\xi_i(t')\xi_j(t)\rangle = \delta(t-t')\delta_{ij}$. Where $\delta(t)$ is the Dirac distribution and δ_{ij} is the Kronecker symbol.

The correct way to take into account a thermal bath is through the Langevin equations. Which in our two-dimensional case are written:

$$\begin{aligned}
m\frac{dv_x}{dt} &= -\frac{\partial U(x,y)}{\partial x} - \eta v_x + \sqrt{2\eta T_x}\xi_x(t),\\
m\frac{dv_y}{dt} &= -\frac{\partial U(x,y)}{\partial y} - \eta v_y + \sqrt{2\eta T_y}\xi_y(t),\\
\frac{dx}{dt} &= v_x,\\
\frac{dy}{dt} &= v_y.
\end{aligned} \tag{6.2}$$

Within this set of equations, things are more complex than it seems. It is unlikely for us to remain within the Langevin frame, except for for numerical simulations purposes. Indeed, the stochastic forces $\xi_i(t)$ are highly discontinuous if treated over time, only integrals or statistical averages of those forces are tractable. For our practical purposes, the trajectory of the particle is not directly useful, but rather the distribution function f of the particle. As the particle evolves erratically through the Langevin dynamics, the distribution function does not keep trace of this discontinuous evolution and is a smooth function of its variables. Reference [32] gives details on how to derive the Fokker-Planck (FP) equation on $f(x, y, v_x, v_y, t)$ starting from the Langevin equations 6.2. We find that the particle distribution function follows the following FP equation:

$$\frac{\partial f(x,y,p_x,p_y,t)}{\partial t} = -\boldsymbol{\nabla}\cdot\mathbf{J}, \tag{6.3}$$

where $\boldsymbol{\nabla} = (\partial_x, \partial_y, \partial_{v_x}\partial_{v_y})$ and

$$\mathbf{J} = \begin{cases} J_x &= v_x f\\ J_y &= v_y f\\ J_{v_x} &= \left(-\frac{1}{m}\frac{\partial U(x,y)}{\partial x} - \eta\frac{v_x}{m}\right)f - \frac{\partial}{\partial v_x}(\frac{\eta T_x}{m^2}f)\\ J_{v_y} &= \left(-\frac{1}{m}\frac{\partial U(x,y)}{\partial y} - \eta\frac{v_y}{m}\right)f - \frac{\partial}{\partial v_y}((\frac{\eta T_y}{m^2}f). \end{cases} \tag{6.4}$$

Under this form the FP equation is said to be in its Kramers form. Written this way, it can be seen as a conservation equation of probability in phase-space. Of course, the first two equations are trivial, they nevertheless allow a useful compact notation. We note that Equation 6.3 is very general, it is exact for white Gaussian noises and for any analytical potential U. We will perform a series of approximations in the next sections, starting from this equation. Our objective is to determine, thank to this FP equation, the conditions of appearance of a non-zero angular momentum $\langle \mathbf{r} \times \mathbf{v} \rangle$. Since we have access to the particle distribution function by solving the FP equation, the angular momentum will be then straightforward to compute.

a) Overdamped solution: model 1

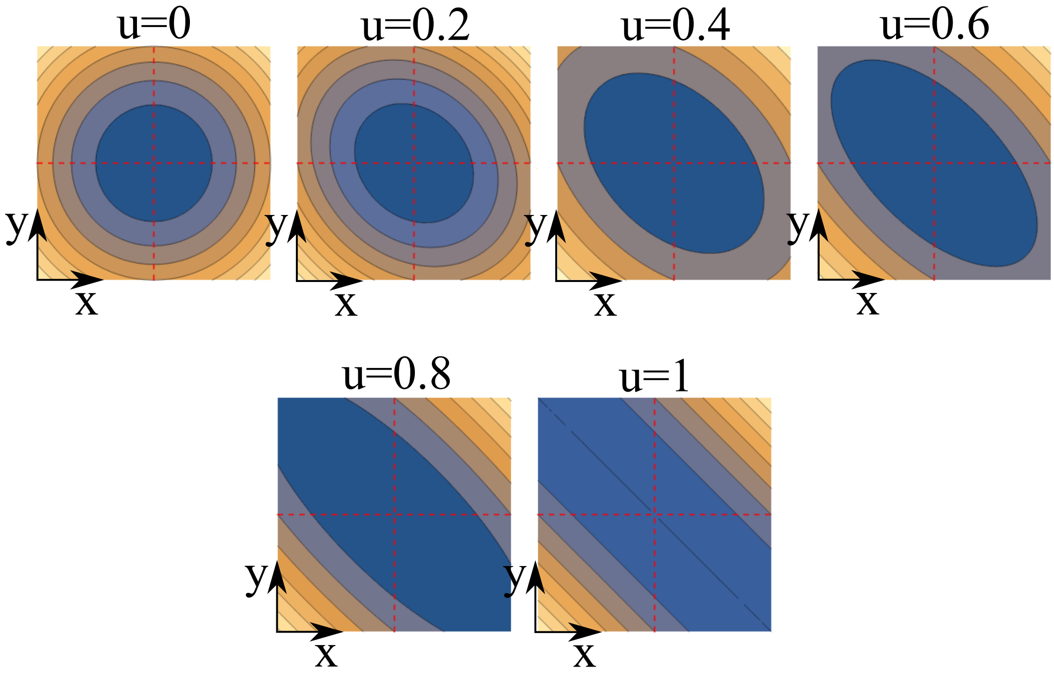

Fig. VI.2 *Iso-potential lines for $k = 1$ and various asymmetry u. As observed $|u| < 1$ is required for confinement.*

We start by assuming a potential such that $U(x, y) = k(\frac{x^2+y^2}{2} + uxy)$ (with $|u| < 1$ for having a confining potential), where k is the elasticity constant and u a dimensionless parameter characterizing the anisotropy of the potential. Figure VI.2 depicts the iso-potential lines for $k = 1$ and u varying from 0 to 1. More precisely, the principal axes of the potential are rotated by $\pi/4$ with respect to $\hat{x}$ and $\hat{y}$, the temperature axes, and $\sqrt{2u/(1-u)}$ is the eccentricity of the iso-potentials lines. We introduce the general method we followed by considering first the overdamped limit in the harmonic case, a case already studied in [156]. This limit is taken by factorizing the particle distribution function in velocity and position. Then the overdamped limit is given by $\eta/\sqrt{km} \to \infty$, which means that $\dot{v}_x = \dot{v}_y = 0$ at any time in Equations 6.2. The Langevin equations may thus be recast as only functions of the particle position:

$$\begin{aligned} \frac{dx}{dt} &= -\frac{k}{\eta}(x+uy) + \sqrt{\frac{2T_x}{\eta}}\xi_x(t), \\ \frac{dy}{dt} &= -\frac{k}{\eta}(y+ux) + \sqrt{\frac{2T_y}{\eta}}\xi_y(t). \end{aligned} \tag{6.5}$$

The associated FP Kramers equation is thus only acting on the particle position distribution $n(x, y, t)$:

$$\frac{\partial n(x,y,t)}{\partial t} = -\boldsymbol{\nabla}\cdot\mathbf{J} \tag{6.6}$$

where $\boldsymbol{\nabla} = (\partial_x, \partial_y)$ and

$$\mathbf{J} = \begin{cases} J_x &= -\frac{k}{\eta}(x+uy)n - \frac{T_x}{\eta}\frac{\partial n}{\partial x} \\ J_y &= -\frac{k}{\eta}(y+ux)n - \frac{T_y}{\eta}\frac{\partial n}{\partial y}. \end{cases} \tag{6.7}$$

To access the stationary position partial distribution function (position PDF) $n(x, y, t)$, we follow the method detailed in Appendix B. To this end, we introduce the 2×2 matrices A, B and covariances matrix Ξ

$$A = -\frac{k}{\eta}\begin{pmatrix} 1 & u \\ u & 1 \end{pmatrix}, B = \frac{2}{\eta}\begin{pmatrix} T_x & 0 \\ 0 & T_y \end{pmatrix}. \tag{6.8}$$

$$\Xi = \frac{1}{2k(1-u^2)}\begin{pmatrix} 2T_x + (T_y - T_x)u^2 & -(T_x+T_y)u \\ -(T_x+T_y)u & 2T_y + (T_x - T_y)u^2 \end{pmatrix}. \tag{6.9}$$

The solution to Eq. (6.6) is the multivariate Gaussian distribution

$$n(\mathbf{r}) = \frac{1}{2\pi\sqrt{\mathrm{Det}(\Xi)}}\exp\left(-\frac{1}{2}(\mathbf{r}-\langle\mathbf{r}\rangle)^T\Xi^{-1}(\mathbf{r}-\langle\mathbf{r}\rangle)\right), \tag{6.10}$$

where $\mathbf{r}$ denotes the two-dimensional vector of components (x, y), $\mathbf{r}^T$ the transpose vector of $\mathbf{r}$ and $\langle\mathbf{r}\rangle$ the statistical average of $\mathbf{r}$. Finally, the stationary PDF reads

$$n(\mathbf{r}) = \frac{k\sqrt{1-u^2}e^{-(\gamma_1 x^2 + \gamma_2 y^2 + \gamma_3 xy)}}{\pi\sqrt{4T_xT_y + u^2(T_y - T_x)^2}}, \tag{6.11}$$

with factors given by

$$\gamma_1 = k\frac{2T_y + u^2(T_x - T_y)}{4T_xT_y + u^2(T_x - T_y)^2}, \tag{6.12}$$

$$\gamma_2 = k\frac{2T_x + u^2(T_y - T_x)}{4T_xT_y + u^2(T_x - T_y)^2}, \tag{6.13}$$

$$\gamma_3 = k\frac{2u(T_x + T_y)}{4T_xT_y + u^2(T_x - T_y)^2}. \tag{6.14}$$

In virtue of the equipartition theorem, for $u = 0$ one obtains $n(\mathbf{r}) \sim e^{-\frac{kx^2}{2T_x} - \frac{ky^2}{2T_y}}$, which indeed corresponds to two decoupled oscillators at equilibrium. To access the marginal distributions $n(x)$ and $n(y)$ respectively, we integrate coincidently Eq. (6.11) over x or y. The marginal distributions have a Gaussian profile. We can also access the variances $\langle x^2 \rangle$ and $\langle y^2 \rangle$. They are given by

$$\langle x^2 \rangle = \frac{T_x + \frac{u^2}{2}(T_y - T_x)}{k(1 - u^2)}, \tag{6.15}$$

$$\langle y^2 \rangle = \frac{T_y + \frac{u^2}{2}(T_x - T_y)}{k(1 - u^2)}, \tag{6.16}$$

together with the cross-correlation average

$$\langle xy \rangle = -\frac{u(T_x + T_y)}{2k(1 - u^2)}. \tag{6.17}$$

This last term is non-zero only if $u \neq 0$ and remains the same if the temperature axes are exchanged $T_x \leftrightarrow T_y$. This quantity is only depending on the position distribution and does not account for non-equilibrium properties such as particle transport.

On the other hand, the stationary state shows non-equilibrium properties: it is characterized by a non-zero current probability $\mathbf{J} = \mathbf{v}n$ [174]. The angular velocity is defined as

$$\omega(t) = \frac{1}{r^2}(\mathbf{r} \times \mathbf{v}). \tag{6.18}$$

The mean angular velocity is given by the long-time limit

$$\langle \omega \rangle = \lim_{t \to \infty} \frac{1}{t} \int_0^t dt' \omega(t'). \tag{6.19}$$

Assuming ergodicity of the system, the time average is equivalent to the ensemble average, one has

$$\langle \omega \rangle = \int d^2\mathbf{r} \frac{1}{r^2}(\mathbf{r} \times \mathbf{v}) n(\mathbf{r}). \tag{6.20}$$

which is more conveniently expressed using polar coordinates

$$\langle\omega\rangle = \int_0^{2\pi} d\theta \int_0^{\infty} dr J_\theta(r,\theta), \tag{6.21}$$

with

$$\begin{aligned} J_\theta(r,\theta) = &-\frac{kur\cos(2\theta)n}{\eta} - \frac{1}{2\eta r}(T_x+T_y)\frac{\partial n}{\partial\theta} \\ &-\frac{T_y-T_x}{2\eta}\left[\frac{\cos(2\theta)}{r}\frac{\partial n}{\partial\theta} + \sin(2\theta)\frac{\partial n}{\partial r}\right]. \end{aligned} \tag{6.22}$$

In polar coordinates, the stationary probability distribution is given by

$$n(r,\theta) = \frac{k\sqrt{1-u^2}e^{-(\gamma_+ + \gamma_- \cos(2\theta) + u\gamma_+ \sin(2\theta))r^2}}{\pi\sqrt{4T_xT_y + u^2(T_y-T_x)^2}}, \tag{6.23}$$

with

$$\gamma_+ = k\frac{T_x+T_y}{4T_xT_y + u^2(T_x-T_y)^2}, \tag{6.24}$$

$$\gamma_- = k\frac{(1-u^2)(T_y-T_x)}{4T_xT_y + u^2(T_x-T_y)^2}. \tag{6.25}$$

Where more clearly than in Cartesian coordinates, the term γ_- is sensitive to the exchange of temperature axes $T_x \leftrightarrow T_y$. Inserting Eq.(6.23) in Eq.(6.22), one obtains the current distribution

$$J_\theta(r,\theta) = \frac{u(T_y-T_x)r}{\eta}[\gamma_+ + \gamma_- \cos(2\theta) + u\gamma_+ \sin(2\theta)]n(r,\theta). \tag{6.26}$$

Consequently, the mean angular velocity is given by

$$\langle\omega\rangle = \frac{k}{\eta}u(T_y-T_x)\sqrt{\frac{1-u^2}{4T_xT_y + u^2(T_x-T_y)^2}}. \tag{6.27}$$

Higher moments of ω can be also obtained analytically

$$\begin{aligned} \langle\omega^n\rangle = k\left(\frac{u(T_y-T_x)}{\eta}\right)^n &\sqrt{\frac{1-u^2}{4T_xT_y + u^2(T_x-T_y)^2}} \\ &\int_0^{2\pi}\frac{d\theta}{2\pi}(\gamma_+ + \gamma_- \cos(2\theta) + u\gamma_+ \sin(2\theta)))^{n-1} \end{aligned} \tag{6.28}$$

which gives a variance

$$\begin{aligned} \langle\omega^2\rangle - \langle\omega\rangle^2 = k\left(\frac{u(T_y-T_x)}{\eta}\right)^2 &\frac{1-u^2}{4T_xT_y + u^2(T_x-T_y)^2} \\ &\left[\frac{T_x+T_y}{\sqrt{4T_xT_y + u^2(T_x-T_y)^2}} - 1\right]. \end{aligned} \tag{6.29}$$

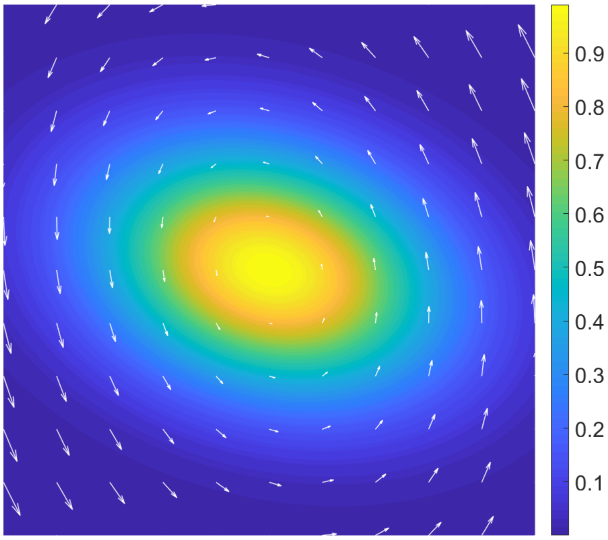

Fig. VI.3 *Density plot of $n(x, y)$ and white arrows representing the vector field of the velocity for a harmonic potential with $u = 0.2$ and $T_y = 2T_x = 1$. Color scale darkens toward low density.*

We see that the variance and all moments vanish when $u = 0$ or $T_y - T_x = 0$, which means a total disappearance of the macroscopic current as soon as one of the two symmetries are not broken.

Figure VI.3 shows a density plot of $n(x, y)$ and the white arrows the vector field of the velocity for a harmonic potential with $u = 0.2$ and $T_y = 2T_x = 1$. The particle density has a maximum in the center whereas the velocity increases linearly with the distance from the center.

We see that, contrary to the cross correlations $\langle xy \rangle$ that requires only $u \neq 0$ to be non-zero, a non-zero current J_θ requires two broken symmetries: two different temperatures ($T_x \neq T_y$), along the orthogonal axes which do not match the principal axes of the potential ($u \neq 0$). The system's chirality thus allows work.

b) Overdamped solution: model 2

One could object that the non-zero current is solely originating from the anisotropy of the potential, but not from the mismatch between the principal axes of the potential and the temperature axes. We thus consider a variant of the previous model where the particle evolves in a modified harmonic potential $U(x, y) = k(\frac{x^2+a^2y^2}{2} + uxy)$. A stable potential requires $|a| > |u|$. By using the same method as presented in Appendix B, we obtain an exact solution of the stationary PDF $n(x, y)$, which reads

$$n(x, y) = \frac{k(1 + a^2)\sqrt{a^2 - u^2}e^{-(\gamma_1' x^2 + \gamma_2' y^2 + \gamma_3' xy)}}{\pi\sqrt{(1 + a^2)^2 T_x T_y + u^2(T_y - T_x)^2}}, \tag{6.30}$$

where

$$\gamma_1' = k\frac{(1+a^2)(T_y(1+a^2)+u^2(T_x-T_y))}{2((1+a^2)^2T_xT_y+u^2(T_x-T_y)^2)} \tag{6.31}$$

$$\gamma_2' = k\frac{(1+a^2)(2T_x+u^2(T_y-T_x))}{2((1+a^2)^2T_xT_y+u^2(T_x-T_y)^2)} \tag{6.32}$$

$$\gamma_3' = k\frac{(1+a^2)u(a^2T_x+T_y)}{(1+a^2)^2T_xT_y+u^2(T_x-T_y)^2}. \tag{6.33}$$

Inserting Eq. (6.30) in Eq. (6.21), one obtains the mean angular velocity:

$$\langle\omega\rangle = \frac{k}{\eta}u(T_y-T_x)\sqrt{\frac{a^2-u^2}{(1+a^2)^2T_xT_y+u^2(T_x-T_y)^2}}. \tag{6.34}$$

For an anisotropic potential where the confinement is different along the two temperature axes, it is noticeable that a non-zero mean angular velocity is proportional to the product $u(T_y-T_x)$, which means that only the temperature difference and the part of the anisotropy of the potential outside of the temperature axes are relevant. As Eq. (6.34) displays it prominently, the effect of the anisotropy along the y-axis modifies slightly the amplitude of angular velocity. Nevertheless, this trap anisotropy only dresses the effect arising from the double symmetry breaking.

This joint symmetry breaking requirement is redundant with the argument presented in the chapter's introduction: in Figure VI.1, if the temperature axes match the M1 and M2 mirror-symmetry axes, there is no possible current.

VI.1.2 Underdamped motion

We go back to the situation of an anisotropic potential $U(x,y)=k(\frac{x^2+y^2}{2}+uxy)$ and consider an underdamped motion (see also [175]). The first guess is that at zero viscosity (homogeneous temperature along $\hat{x}$ and $\hat{x}$) the non-zero current will vanish. However, the transition between two regimes is unknown and especially one can question if the effect remains at any finite viscosity or is there a discontinuous transition. For a finite viscosity, the velocity and position distributions have now comparable dynamical times *i.e.* we need to treat position and velocity altogether. There is thus 4 Langevin equations to consider:

$$\begin{aligned}
\frac{dv_x}{dt} &= -\frac{1}{m}\frac{\partial U(x,y)}{\partial x} - \frac{\eta}{m}v_x + \sqrt{\frac{2\eta T_x}{m^2}}\xi_x(t), \\
\frac{dv_y}{dt} &= -\frac{1}{m}\frac{\partial U(x,y)}{\partial y} - \frac{\eta}{m}v_y + \sqrt{\frac{2\eta T_y}{m^2}}\xi_y(t), \\
\frac{dx}{dt} &= v_x, \\
\frac{dy}{dt} &= v_y.
\end{aligned} \tag{6.35}$$

The corresponding Fokker-Planck equation in Kramers form is:

$$\frac{\partial f(x,y,v_x,v_y,t)}{\partial t} = -\boldsymbol{\nabla}\cdot\mathbf{J}, \tag{6.36}$$

where $\boldsymbol{\nabla} = (\partial_x, \partial_y, \partial_{v_x}\partial_{v_y})$ generalizes the gradient to velocities. We also have the four dimensional current

$$\mathbf{J} = \begin{cases} J_x & = v_x P \\ J_y & = v_y P \\ J_{v_x} & = \left(-\frac{1}{m}\frac{\partial U(x,y)}{\partial x} - \eta\frac{v_x}{m}\right) f - \frac{\partial}{\partial v_x}(\frac{\eta T_x}{m^2} f) \\ J_{v_y} & = \left(-\frac{1}{m}\frac{\partial U(x,y)}{\partial y} - \eta\frac{v_y}{m}\right) f - \frac{\partial}{\partial v_y}(\frac{\eta T_y}{m^2} f). \end{cases} \tag{6.37}$$

The stationary PDFs depends now on the variables x, y, v_x and v_y which are defined as components of a 4-component vector $(\mathbf{r},\mathbf{v})$. The associated matrices A and B (Appendix B) are given by

$$A = \frac{1}{m}\begin{pmatrix} 0 & 0 & m & 0 \\ 0 & 0 & 0 & m \\ -k & -ku & -\eta & 0 \\ -ku & -k & 0 & -\eta \end{pmatrix}, B = \frac{\eta}{m^2}\begin{pmatrix} 0 & 0 & 0 & 0 \\ 0 & 0 & 0 & 0 \\ 0 & 0 & 2T_x & 0 \\ 0 & 0 & 0 & 2T_y \end{pmatrix}. \tag{6.38}$$

We also introduce the dimensionless viscosity $\eta' = \eta/\sqrt{km}$ whom value[1], pilots the dynamics between overdamped and underdamped dynamics. The covariances matrix Ξ is obtained by solving Eq. (2.3) in Appendix B:

$$\Xi = \begin{pmatrix} \frac{2\eta'^2 T_x + u^2(T_x+T_y) + \eta'^2(T_y-T_x)}{2k(\eta'^2+u^2)(1-u^2)} & -\frac{u(T_x+T_y)}{2k(1-u^2)} & 0 & -\frac{\eta'(T_x-T_y)u}{2\sqrt{km}(\eta'^2+u^2)} \\ \frac{-u(T_x+T_y)}{2k(1-u^2)} & \frac{2\eta'^2 T_y + u^2(T_x+T_y) + \eta'^2(T_x-T_y)}{2k(\eta'^2+u^2)(1-u^2)} & \frac{\eta'(T_x-T_y)u}{2\sqrt{km}(\eta'^2+u^2)} & 0 \\ 0 & \frac{\eta'(T_x-T_y)u}{2\sqrt{km}(\eta'^2+u^2)} & \frac{2T_x\eta'^2+(T_x+T_y)u^2}{2m(\eta'^2+u^2)} & 0 \\ -\frac{\eta'(T_x-T_y)u}{2\sqrt{km}(\eta'^2+u^2)} & 0 & 0 & \frac{2T_y\eta'^2+(T_x+T_y)u^2}{2m(\eta'^2+u^2)} \end{pmatrix}. \tag{6.39}$$

We again, obtain the probability distribution $f(x,y,v_x,v_y,t)$ by inverting Ξ. The marginal probability distributions, namely the position PDFs, $n(x), n(y)$ and velocity PDFs $g(v_x), g(v_y)$ can be calculated by partial integration. We obtain for the position PDFs along $\hat{x}$:

$$n(x) = \frac{1}{\sqrt{2\pi T_{xe}}}\exp(-\frac{x^2}{2T_{xe}}) \tag{6.40}$$

---

[1] It is also the ratio between the characteristic time of the harmonic potential over the viscous damping time *i.e.* the quality factor of the oscillator.

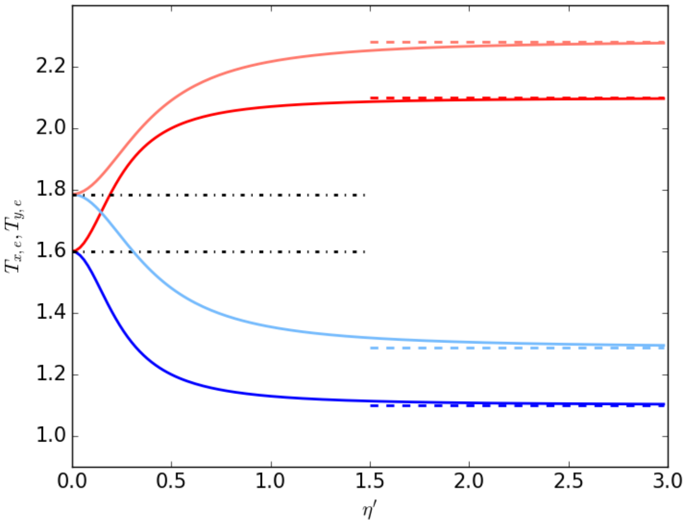

Fig. VI.4 *Effective temperatures T_{xe} and T_{ye} of the position PDFs versus the viscosity η for $T_x = 1$, $T_y = 2$ and $u = 0.25$ (lower curves) and $u = 0.4$ (upper curves). The plain lines correspond to the temperatures along the directions Ox (blue) and Oy (red). The dashed lines give the high friction limit, where the two effective temperatures are larger and smaller than T_x and T_y. The dashed-dotted lines indicate the zero-friction limit, respectively.*

where T_{xe} is an effective temperature and similarly for $n(y)$ by swapping $x \leftrightarrow y$ for indices and variables.

The situation is as if the temperature was given by an effective T_{xe} defined by:

$$T_{xe} = \frac{\eta'^2 T_x + \frac{u^2}{2}\left(\eta'^2(T_y - T_x) + (T_x + T_y)\right)}{(1-u^2)\left(\eta'^2 + u^2\right)}. \tag{6.41}$$

Similarly, along y, the effective temperature T_{ye} is given by

$$T_{ye} = \frac{\eta'^2 T_y + \frac{u^2}{2}\left(\eta'^2(T_x - T_y) + (T_x + T_y)\right)}{(1-u^2)\left(\eta'^2 + u^2\right)}. \tag{6.42}$$

Taking $\eta' \gg 1$, Equations (6.41) and (6.42) we recover the overdamped limit given by Equation (6.15). Also, when $\eta' \to 0$, we obtain $T_{xe} = T_{ye} = \frac{T_x + T_y}{2(1-u^2)}$. In this limit, the trap frequency is much larger than the damping rate. Due to its large frequency, the trap "stirs" the two dimensions together and they end up having the same mean temperature. The extreme scenario of this limit is an infinitely deep trap where particles end up falling regardless of the details of its initial conditions: all the initial conditions are quickly erased. The opposite limit would consist in a flat potential where the two directions remain independent and their information remain well separated.

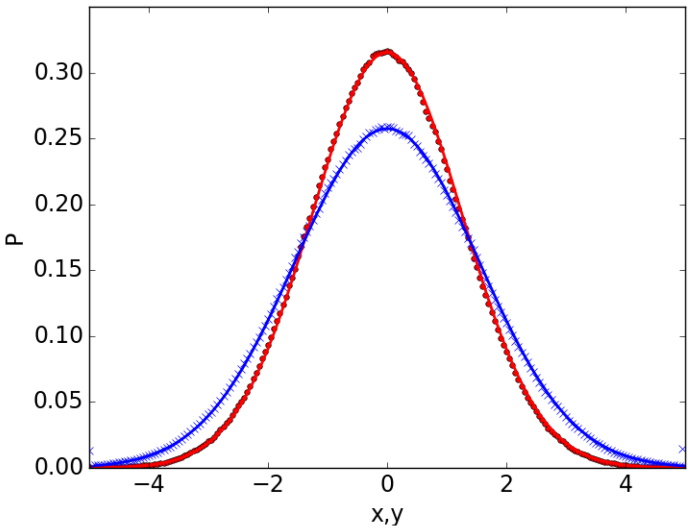

Fig. VI.5 *Stationary position PDFs $n(x)$ (red) and $n(y)$ (blue) for an asymmetric harmonic potential ($u = 0.5$), a dimensionless viscosity $\eta' = 1$, with $T_x = 1$ and $T_y = 2$.*

Figure VI.4 shows how T_{xe} and T_{ye} depend on the dimensionless viscosity η' for $T_x = 1$ and $T_y = 2$ (full lines). Note that effective temperatures T_{xe} and T_{ye}, which start from the same value $(T_x + T_y)/2(1 - u^2)$, respectively decreases and increases rapidly towards their asymptotic values, $T_{xe}(\infty)$ and $T_{ye}(\infty)$. In other words, at low viscosity, the width of the position PDF is given by the mean temperature of both directions (up to a $(1 - u^2)^{-1}$ factor), whereas when the dimensionless viscosity increases, the effective temperatures go rapidly towards the asymptotic values (which are independent of the viscosity). It can be re-expressed in terms of the competition between damping characteristic time and the trap period $\sqrt{k/m}$. The two dimensions x and y starts acting independently as soon as the trap period is long enough, which corresponds to moving towards the overdamped regime or similarly corresponds to increasing η'. We note that the effective temperatures along each direction are different from the reservoir temperatures T_x and T_y, which is the direct consequence of the non-zero transport of particles. The relative importance of u and η' is shown in Figure VI.4. It can be shown analytically that the inflection point marking the crossover between overdamped and underdamped regimes is located at $\eta' \approx u/\sqrt{3}$.

Figure VI.5 shows the position PDFs, $n(x)$ and $n(y)$ for two temperatures T_x and T_y and a reduced viscosity $\eta' = 1$ (full curves). The dashes curves correspond to the simulations of the Langevin equations in the underdamped regime (refer to upcoming Section VI.3 for more details) and show excellent agreement with the analytical expression given in Equation (6.40).

In the harmonic case, we obtain exact expressions also for the velocity PDFs. Integrating the total PDF $f(x, y, v_x, v_y)$ over the positions, it is straightforward to show that the velocity PDF are Gaussian with an effective temperature T_{v_xe} and T_{v_ye} given by

$$T_{v_xe} = \frac{2T_x\eta'^2 + u^2(T_x + T_y)}{2(u^2 + \eta'^2)}, \tag{6.43}$$

$$T_{v_ye} = \frac{2T_y\eta'^2 + u^2(T_x + T_y)}{2(u^2 + \eta'^2)}. \tag{6.44}$$

It is as expected that when $\eta' \to \infty$, one recovers that $T_{v_xe} = T_x$ and $T_{v_ye} = T_y$ irrespective of the value of u. In this overdamped limit, the velocity distribution is independent of the potential: the two dimensions are completely decoupled, and each component of the velocity thermalizes according to its corresponding reservoir temperature. Conversely, when $\eta' \to 0$, the two effective temperatures, T_{v_xe} and $T_{v_y,e}$ go to the same limit $(T_x + T_y)/2$.

Figure VI.6 shows the effective temperatures $T_{v_x,e}$ and $T_{v_y,e}$ as a function of viscosity for two values of the asymmetry parameter $u = 0.25, 0.4$. As it has been observed for the effective temperatures $T_{x,e}$ and $T_{y,e}$ of the position PDFs, the asymptotic values of the high friction limit are rapidly reached (at around $\eta' > 2$). However, although the "position temperatures" $T_{x,e}$ and $T_{y,e}$ go to asymptotic values which depend on the asymmetry parameter u and on the two temperatures T_x and T_y, the "velocity temperatures" $T_{v_x,e}$ and $T_{v_y,e}$ go to T_x and T_y, respectively.

Remarkably, whereas the stationary positions and velocities PDFs are symmetric and are Gaussian, the particle motion exhibits a mean rotation velocity. Similarly to what has been said on the cross-correlations $\langle xy \rangle$ which is non-zero necessarily but not sufficiently to lead to a non-zero current, the transport properties do not appear immediately in the PDFs but only while investing specific dynamical quantities coupling position and velocities. We recall that such a quantity, the mean angular velocity is given by

$$\langle \omega \rangle = \int d^2\mathbf{r} \int d^2\mathbf{v} \frac{1}{r^2}(\mathbf{r} \times \mathbf{v}) f(\mathbf{r}, \mathbf{v}). \tag{6.45}$$

This quantity is more suitably recast in terms of polar coordinates

$$\langle \omega \rangle = \int dv_r \int dv_\theta \int d\theta \int dr\, v_\theta f(r, \theta, v_r, v_\theta), \tag{6.46}$$

which after calculation, yields:

$$\langle \omega \rangle = \frac{\sqrt{k/m}u(T_y - T_x)\sqrt{1 - u^2}}{\eta'\sqrt{[4T_x T_y + u^2(T_x - T_y)^2] + \left(\frac{u^4}{\eta'^4} + 2\frac{u^2}{\eta'^2}\right)(T_y + T_x)^2}}. \tag{6.47}$$

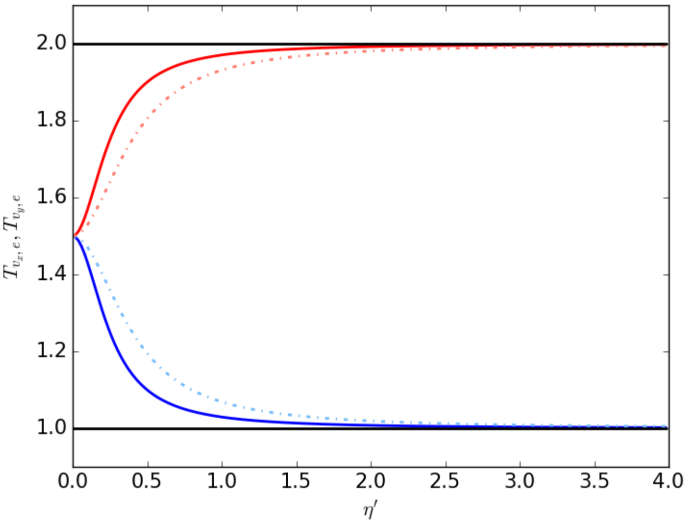

Fig. VI.6 *Effective temperatures $T_{v_x,e}$ and $T_{v_y,e}$ of the velocity PDFs for an asymmetric harmonic potential with a viscosity $\eta = 1$, $T_x = 1$, $T_y = 2$ and for two values of the asymmetry parameter $u = 0.25$ (full curves) and $u = 0.4$ (dot-dashed curves). The magenta lines give the $\eta' \to +\infty$ limit.*

In the overdamped limit ($\eta' \to \infty$) one recovers Eq. (6.27). In the underdamped limit $\eta' \to 0$, the mean angular velocity decreases to zero as the inverse of the particle mass. Indeed, the underdamped limit corresponds as well to an infinitely massive particle which high inertia forbids rapid changes in its velocity: the particle is just rolling in the potential without experiencing of the effect of the reservoirs before many oscillations.

The evolution of $\langle \omega \rangle$ as a function of the asymmetry parameter u for two values $\eta' = 1, 5$ is displayed in Figure VI.7. The full curves correspond to Eq. 6.47. As previously observed with other quantities, for $\eta' > 3$, the mean angular velocity matches the exact expression corresponding to the high-friction limit.

We have shown that the two-temperature model has a stationary solution with a non-zero current when both the potential is asymmetric, and the temperatures are different. One notes that the current is maximum in the overdamped situation.

VI.2 Weak asymmetric potential

The previous section has shown that an analytical approach is possible for the harmonic potential, however higher order potentials may not have a so straightforward resolution. Since, the previous non-zero current is proportional to the difference in temperature $T_y - T_x$ and asymmetry parameter u, it suggests that we can study

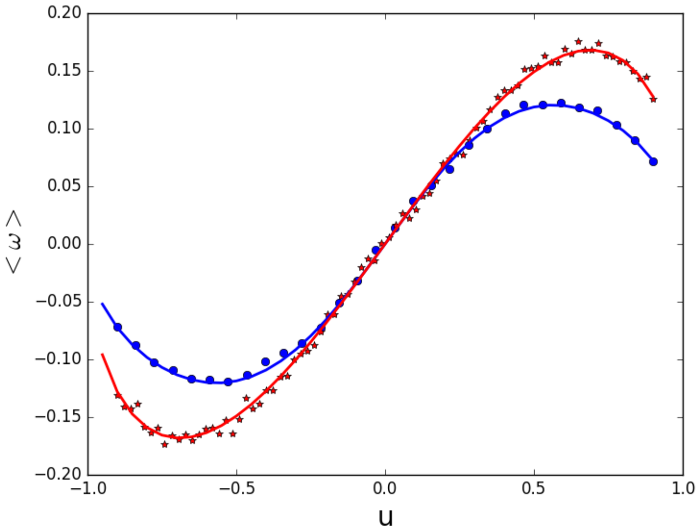

Fig. VI.7 *Numerical simulations of the mean angular velocity* $\langle\omega\rangle$ *(in rad.s*$^{-1}$*) as function of the asymmetry parameter* u *for two different viscosities* $\eta' = 1, 5$*, when* $T_x = 1$*,* $T_y = 2$ *(circles and stars). The full curves correspond to the exact expression in the high friction limit.*

perturbatively the phenomenon. We thus consider an overdamped motion of a particle of mass m in a weakly asymmetric potential $U(r,\theta) = U_0(r) + uU_1(r,\theta)$, where $u \ll 1$ is a small dimensionless parameter and $U_1(r) \leq U_0(r)$ when r is large. Moreover, we consider that the two temperatures are also close, in order to perform the perturbative expansion of the Fokker-Planck equation. The mean temperature is $T = (T_x + T_y)/2$ and the two temperatures along the x and y axes are $T_x = T(1 - \alpha/2)$ and $T_y = T(1 + \alpha/2)$, and $\alpha \ll 1$ is a small dimensionless parameter. Using Eq. (6.6) and expressing the current in polar coordinates, the stationary solution $n(r,\theta)$ satisfies

$$\frac{1}{r}\frac{\partial(rJ_r)}{\partial r} + \frac{1}{r}\frac{\partial J_\theta}{\partial\theta} = 0, \tag{6.48}$$

where the radial and orthoradial currents J_r and J_θ, are the sum of the two contributions

$$J_r = J_r^{(1)} + J_r^{(2)} \quad \text{and} \quad J_\theta = J_\theta^{(1)} + J_\theta^{(2)} \tag{6.49}$$

where

$$J_r^{(1)}(r,\theta) = -\frac{n}{\eta}\frac{\partial U}{\partial r} - \frac{T}{\eta}\frac{\partial n}{\partial r}, \tag{6.50}$$

$$J_\theta^{(1)}(r,\theta) = -\frac{n}{\eta r}\frac{\partial U}{\partial\theta} - \frac{T}{\eta r}\frac{\partial n}{\partial\theta} \tag{6.51}$$

and

$$J_r^{(2)}(r,\theta) = -\frac{\alpha T}{2\eta}\left(-\cos(2\theta)\frac{\partial n}{\partial r} + \frac{\sin(2\theta)}{r}\frac{\partial n}{\partial \theta}\right), \tag{6.52}$$

$$J_\theta^{(2)}(r,\theta) = -\frac{\alpha T}{2\eta}\left(\sin(2\theta)\frac{\partial n}{\partial r} + \frac{\cos(2\theta)}{r}\frac{\partial n}{\partial \theta}\right). \tag{6.53}$$

$\mathbf{J}^{(1)}$ and $\mathbf{J}^{(2)}$ are the currents associated with the mean temperature and with the temperature difference along the two axes, respectively. When $\alpha = 0$, the stationary solution of the Fokker-Planck equation is the equilibrium distribution $n_0^u(r,\theta) \propto e^{-(U_0(r)+uU_1(r,\theta))/T}$, where the associated current vanishes.

In order to perform a perturbative expansion, we propose the following ansatz for the stationary distribution

$$n(r,\theta) = n_0^u(r,\theta)n_1(r,\theta), \tag{6.54}$$

which gives

$$\begin{aligned} J_r^{(1)}(r,\theta) &= -\frac{Tn_0^u(r,\theta)}{\eta}\frac{\partial n_1(r,\theta)}{\partial r}, \\ J_\theta^{(1)}(r,\theta) &= -\frac{Tn_0^u(r,\theta)}{\eta r}\frac{\partial n_1(r,\theta)}{\partial \theta}. \end{aligned} \tag{6.55}$$

Inserting Eq.(6.55) in Eq.(6.48), one finally obtains

$$n_0^u(r,\theta)\Delta n_1(r,\theta) + \nabla n_0^u(r,\theta).\nabla n_1(r,\theta) = -\frac{\eta}{T}\nabla\cdot\mathbf{J}^{(2)}. \tag{6.56}$$

Assuming that $n_1(r) \propto \exp(-\alpha h(r,\theta,u,\alpha))$, and performing a first-order expansion in α (and a zero-order expansion in u), one has

$$\Delta n_1(r,\theta) = -\alpha n_1(r,\theta)\Delta h(r,\theta) + \mathcal{O}(\alpha^2), \tag{6.57}$$

$$\nabla n_0^u(r,\theta).\nabla n_1(r,\theta) = \frac{\alpha}{T}n_0^0(r)n_1(r,\theta)\frac{\partial U_0(r)}{\partial r}\frac{\partial h(r,\theta)}{\partial r} + \mathcal{O}(\alpha^2), \tag{6.58}$$

and

$$\begin{aligned} \nabla\cdot J^{(2)} = \frac{\alpha\cos(2\theta)}{2\eta}n_0^0(r)n_1(r,\theta)&\left[\frac{1}{r}\frac{\partial}{\partial r}\left(r\frac{\partial U_0(r)}{\partial r}\right)\right. \\ &\left.-\frac{1}{T}\left(\frac{\partial U_0(r)}{\partial r}\right)^2 - \frac{2}{r}\frac{\partial U_0(r)}{\partial r}\right] + \mathcal{O}(\alpha^2). \end{aligned} \tag{6.59}$$

Therefore, the function $h(r,\theta)$ satisfies the partial differential equation

$$\begin{aligned} \Delta h(r,\theta) - \frac{1}{T}\frac{\partial U_0(r)}{\partial r}.\frac{\partial h(r,\theta)}{\partial r} = \frac{\cos(2\theta)}{2T}&\left[\frac{1}{r}\frac{\partial}{\partial r}\left(r\frac{\partial U_0(r)}{\partial r}\right)\right. \\ &\left.-\frac{1}{T}\left(\frac{\partial U_0(r)}{\partial r}\right)^2 - \frac{2}{r}\frac{\partial U_0(r)}{\partial r}\right]. \end{aligned} \tag{6.60}$$

Inserting that $h(r,\theta) = \cos(2\theta)g(r)$, on obtains a differential equation for $g(r)$.

$$\frac{d^2g(r)}{dr^2} + \frac{1}{r}\frac{dg(r)}{dr} - 4\frac{g(r)}{r^2} - \frac{1}{T}\frac{\partial U_0(r)}{\partial r}.\frac{dg(r)}{dr} =$$
$$\frac{1}{2T}\left[\frac{1}{r}\frac{\partial}{\partial r}\left(r\frac{\partial U_0(r)}{\partial r}\right) - \frac{1}{T}\left(\frac{\partial U_0(r)}{\partial r}\right)^2 - \frac{2}{r}\frac{\partial U_0(r)}{\partial r}\right]. \tag{6.61}$$

The analytic solution of the differential cannot be obtained in general. However, assuming that $U_0(r) \sim r^\alpha$ (with $\alpha \geq 2$) when $r \to \infty$, one obtains that the asymptotic behavior of $g(r)$ is $g(r) \sim U_0(r)/(2T)$. A solution exists for the harmonic potential where $g(r) = kr^2/(4T)$. The probability distribution is then given by

$$n(r,\theta) \propto \exp(-\frac{kr^2}{2T}(1 + u\sin(2\theta) + \frac{\alpha}{2}\cos(2\theta)), \tag{6.62}$$

which corresponds to the lowest order expansion in u and α of Eq. (6.23) and a mean angular velocity given $\langle\omega\rangle \propto \alpha ukT/\eta$.

Similarly, we now show that the ansatz gives the leading behavior of the mean angular velocity. Using that $n(r,\theta) \propto \exp(-(U_0(r)+uU_1(r,\theta))/T - \alpha\cos(2\theta)g(r)))$ Eq. (6.51) becomes

$$J_\theta^{(1)}(r,\theta) = -\frac{2T\alpha}{\eta r}g(r)\sin(2\theta)n(r,\theta). \tag{6.63}$$

The Fourier series of the potential's anisotropic part is:

$$U_1(r,\theta) = \sum_{k\geq 2} a_k(r)\cos(k\theta) + b_k(r)\sin(k\theta). \tag{6.64}$$

Because the principal axes of the potential mismatch the temperature axes, this implies that $b_2(r)$ is nonzero (or at least a single $b_k(r)$, $k \geq 2$, is nonzero). Performing an expansion in u and α of Eq. (6.62), one obtains that the integral of $J^{(1)}(r,\theta)$ over θ is proportional to αuT.

Similarly, inserting the ansatz of $n(r\theta)$ in Eq. (6.53), the leading term of the current is given by

$$J_\theta^{(2)}(r,\theta) = +\frac{\alpha}{2\eta}\left(\sin(2\theta)\frac{\partial U_0(r,\theta)}{\partial r}\right)n(r,\theta). \tag{6.65}$$

The integration of $J_\theta^{(2)}(r,\theta)$ provides a second contribution of $\langle\omega\rangle$ which is also proportional to αuT. Note that when $g(r) = \frac{r}{4T}\frac{\partial U_0(r)}{\partial r}$ the two contributions vanish. For this case which corresponds to the harmonic potential, the orthogonal current must be calculated to the next order, which is proportional to $u\alpha$ and one recovers the result obtained in section II, which leads a mean angular velocity proportional to $u\alpha T$. Finally, in all cases, we have shown that the mean angular velocity is proportional to αuT, (for $u, \alpha \ll 1$) which confirms the fact that the existence of the mean current is associated with the double symmetry breaking.

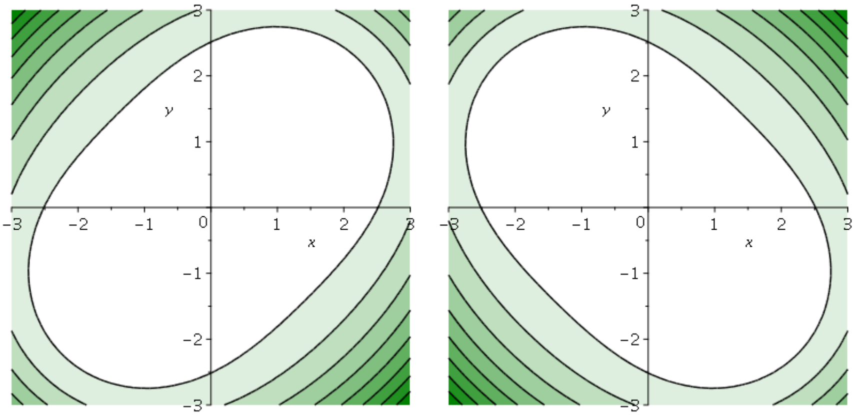

Fig. VI.8 *Contourplot of the potential* $U(x, y) = (x^2 + y^2)^2/4 + uxy$ *for* $u = 3$ *(left) and* $u = -3$ *(right).*

VI.3 Simulation

We performed stochastic simulation of a particle in the underdamped and overdamped situations to test the results obtained analytically. To solve the stochastic differential equation in the underdamped situation, we implement a Verlet-like algorithm which has the property of using one random number per time step [176]. Each run is performed with a total reduced elapsed time 3000. Several quantities are monitored in the stationary state: the position probability distributions, the velocity probability distributions. In order to obtain reliable statistics, one considers the probability distribution along each axis instead of two-dimensional probability distribution.

We first consider the harmonic potential and all observables (position and velocity PDF) mean angular velocity match the exact results for any value of the viscosity. In particular, we recover the overdamped limit very rapidly when $\eta' > 3$.

As seen above, no exact expression is obtained even for a spherical potential except the harmonic potential. We first simulate the model for $U(x, y) = (x^2+y^2)^2/4+uxy$. Figure VI.8 displays the asymmetry of the potential for $u = 5$ and $u = -5$. The mean angular velocity is plotted as a function of the asymmetry parameter u (see FigureVI.9) for different values of $T_y = 2, 1.5, 1.2, 0.8, 0.5$ and $T_x = 1$. These values correspond to $\alpha = 1, 0.5, 0.2, -0.2, -0.5$ and $T = 1.5, 1.1, 0.9, 0.75$, respectively. The perturbative analysis of section VI.2 predicts that the mean angular velocity is proportional to αuT when $u, \alpha \ll 1$. Figure VI.10 displays the reduces mean angular velocity $\omega/\alpha T$ as a function of u, and we observe that all the curves collapse for small values of u. For $u = 0$, no mean current exists. For $u > 1.5$, a nonlinear dependence on u appears and two extreme values of the mean angular velocity exists for $u \simeq \pm 2$. In addition, the intensity of the mean angular velocity is increased compared to the harmonic case.

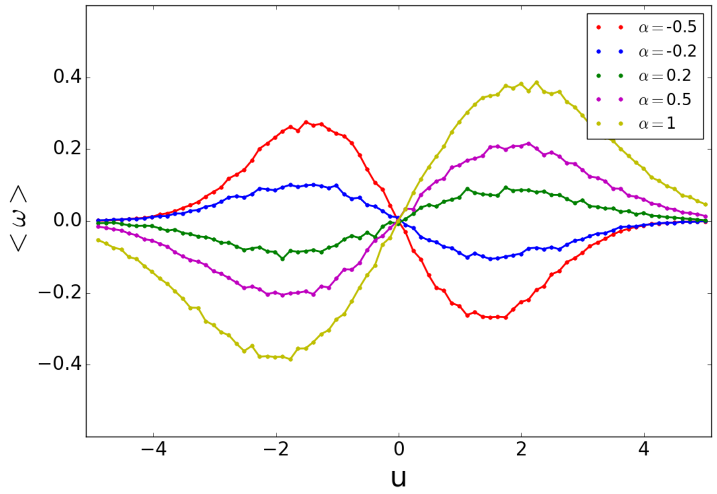

Fig. VI.9 *Mean angular velocity versus the asymmetry parameter u for the potential $U(x,y) = (x^2 + y^2)^2/4 + uxy$ for $T_x = 1$ and $T_y = 2$.*

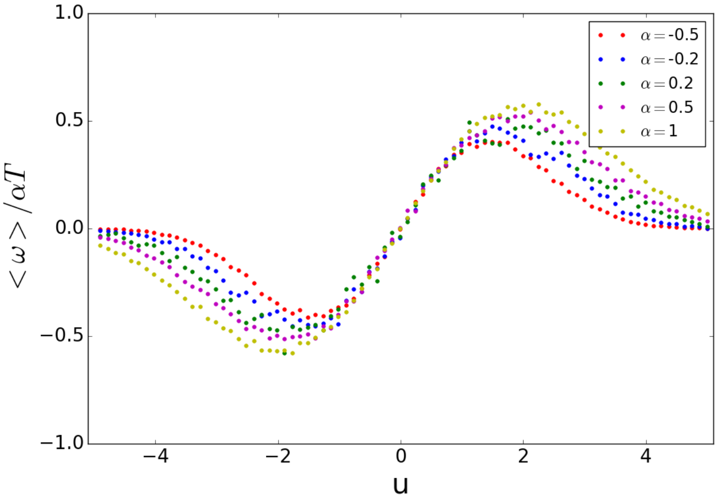

Fig. VI.10 *Rescaled mean angular velocity $\omega/(\alpha T)$ versus the asymmetry parameter u for the potential $U(x,y) = (x^2 + y^2)^2/4 + uxy$ and $\alpha = 1, 0.5, 0.2, -0.2, -0.5$.*

VI.4 Observation on cold atoms

Cold atoms experiments can deal with intensity or laser detuning imbalance during the cooling phase, leading to different temperatures along the different cooling axis. By adding a two-dimensional optical dipole trap, one can as well tailor the asymmetric parameter u at will. Breaking the two symmetries in this case, we wonder to

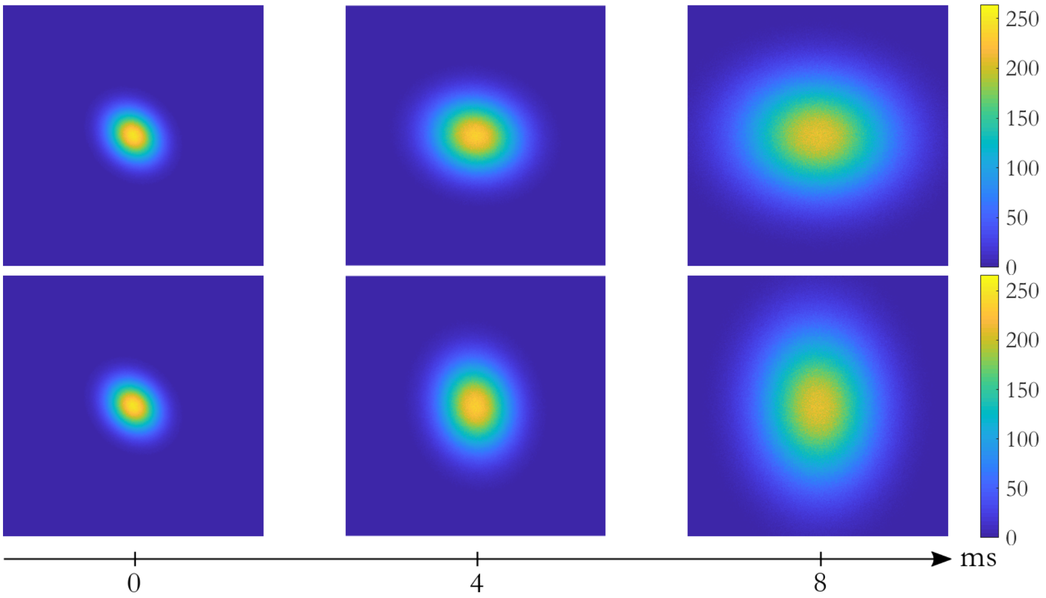

Fig. VI.11 *Time of flight simulations (TOF) emphasizing the difference of behavior when reversing the rotation. The spatial density is plotted after different times of TOF for both clockwise rotation (upper) and counter-clockwise rotation (lower).*

what extent this thermal rotation can be observed. Rotation of atomic clouds have been previously reported in the context of a beam-misaligned vortex trap [59, 177] and more recently using synthetic Lorentz forces [178, 179, 180]. As opposed to those previous studies where the rotation is due to a net mean radiation pressure force, our proposal is based on a stochastic force with zero mean value.

We compute $\langle\omega\rangle$ for optical molasses, in the presence of an optical dipole trap using a semi-classical approach of laser cooling (see for example [181]). For simple experimental implementation, we consider a two-dimensional laser cooling where all laser beams have the same frequency detuning δ with respect to an atomic transition but with different laser intensities I_x and I_y, respectively along the x-axis and y-axis. We can then define the saturation parameter $s_i = (I_i/I_s)/(1+4\delta^2/\Gamma^2)$, where I_s is the saturation intensity of the atomic transition, Γ the atomic linewidth and $i = x, y$. In what follows, we consider the low saturation limit, namely $s_i \ll 1$, so we can sum up the individual contributions of each laser beams to the total radiation pressure force (mean and fluctuating parts). The expansion for the viscous force (mean component) along the i-axis reads:

$$\mathbf{F}_i = -\eta_i \mathbf{v} \qquad \eta_i = -4\hbar k^2 s_i \frac{2\delta/\Gamma}{1+(2\delta/\Gamma)^2}, \tag{6.66}$$

where k is the wave-vector of the laser beams and $\hbar$ the Planck constant.

The diffusion constant (fluctuating component), along the x-axis reads

$$D_x = \frac{1}{4}\hbar^2 k^2 \Gamma(s_x + s_y) + \frac{1}{2}\hbar^2 k^2 \Gamma s_x. \tag{6.67}$$

The first term on the right side, comes from the photon spontaneous emission events (isotopic radiation pattern), whereas the second term is due to the laser photon absorption events. A similar expression is found along the y-axis swapping subscripts x and y in Eq. (6.67). Additionally, we assume $\eta = (\eta_x + \eta_y)/2$, to simplify the calculation. More precisely, we could set $\eta_x = \eta_y$ and $D_x \neq D_y$ choosing different frequency detunings and different intensities.

The temperatures along one direction $i = x, y$ are given by the Einstein relation

$$T_i = \frac{D_i}{\eta}. \tag{6.68}$$

The presence of an asymmetric optical dipole trap $U(x, y) = \frac{m\omega_T^2}{2}(x^2 + y^2 + 2uxy)$, leads to the second broken symmetry. According to Eq. 6.47 the mean angular frequency reads

$$\langle\omega\rangle = \frac{m(\hbar k \omega_T)^2}{2\eta^2} u(s_y - s_x)\sqrt{\frac{1 - u^2}{4T_xT_y + u^2(T_x - T_y)^2}}. \tag{6.69}$$

The scheme could not be implemented on standard alkaline atoms where broad transitions lead to Doppler temperatures usually higher than the potential depth. In contrast, narrow inter combination lines of Alkaline-earth atoms are favorable to such experiments. For instance, cooling of bosonic Strontium 88 on the inter combination line ${}^1S_0 \rightarrow {}^3P_1$ of linewidth $\Gamma/2\pi = 7.5$kHz, leads to temperatures in the μK range compatible with usual dipole trap depth [56, 40]. For an illustrative and realistic example, we take a dipole trap frequency of $\omega_T = 250$ Hz, saturation parameters $\{\frac{I_x}{I_s}, \frac{I_y}{I_s}\} = 1, 4$ and a detuning $\delta = -3$. We choose as a trap anisotropy $u = 0.4$. Our model gives $T_x = 0.39$ μK, $T_y = 0.72$ μK and a mean angular velocity of 15 Hz. Additionally, the inverse quality factor (dimensionless viscosity) η' is close to 2, leading to an overdamped dynamic. Figure VI.11 displays a simple time-of-flight (TOF) experiment to visualize the effect. After stirring the atoms, we release them from the trap and following their ballistic expansion along x and y. The clockwise (upper) and counter-clockwise (lower) cases clearly show a net mean rotation. Those figures were realized using a Cholesky decomposition of the covariance matrix Ξ, which gives access to (x, y, v_x, v_y) for an arbitrary number of independent particles. Here this number of atoms is chosen reasonably high ($\sim 2 \times 10^7$) for a clear reading of the figures. Initially small, the cloud will expand and maintain an asymmetric shape, as if the rotation was rigid. Nevertheless, we keep in mind two important facts: first the rotation is not strictly rigid due to the θ-dependence in Eq. 6.26. Second, our model is for independent particles and thus, the optical depth has to be low such that multiple scattering, which couple atoms, can be disregarded. Finally, we note that the rotation is done in the strong overdamped limit. Indeed, the characteristic decay time of the velocity is given by m/η which is in the millisecond range, namely much shorter than $|\langle\omega\rangle|^{-1}$.

VI.5 Conclusion

It has been shown in this section that, while considering the motion of a confined particle in presence of two heat reservoirs, the appearance of a non-zero current of particle is the consequence of a double symmetry breaking. The first symmetry is the non-zero temperature difference between the two heat baths, allowing a transfer of energy between them. The second symmetry is the trap asymmetry out of the temperature axes, which enables an actual coupling between the two baths. In presence of this double symmetry breaking, the system undergoes a global rotation whose mean angular velocity sign depends on the temperature difference between the heat baths. This system is then known under several names: temperature ratchet, gyrator, Brownian motor but its principle is easy to characterize and universal. The only constraints are the correct temperature symmetry breaking and the particle asymmetric confinement.

It could be objected that no apparent favored direction seems to be present in the Langevin equations 6.2, at least from the point of view of the microscopic dynamics and the temperature asymmetry. But the result is a non-zero macroscopic current of particles. The phenomenon would appear to break the Curie principle if the second symmetry -the spatial symmetry- was not broken. It illustrates how primitive and simple a Brownian motor can be: a characteristic that allowed fundamental life forms to appear (e.g. [182]). The problem addressed in this section is fundamental from many perspectives: in quantum information where information has to be written and erased on nano-scaled systems extremely sensitive to noise. The experimental demonstration of the minimum entropy generated (Landauer entropy) by the erasure of a single quantum bit has been reported in [183]. On the side of life sciences, understanding how microscopic life forms handle the interplay between keeping information and consuming energy, is also of major interest. The latest point being addressed in the recent articles [184, 185].

Chapter VII

Conclusion

Throughout the first chapters of the manuscript we have generalized and refined a model of cold atoms interacting with an attractive long-range force in 2D. A setup of cold atoms of strontium was at our disposal to perform the experiment. The design of the imaging system and of the 2D optical dipole trap for the atoms was part of the thesis original and initial work. We found evidence of a measurable effect arising from the long-range force, albeit unable to quantitatively characterize it because of technical limitations. The choice of ^{88}Sr for the experiment is justified by its very low Doppler temperature on the intercombination line and low inter-particles scattering length, it is however a more demanding species to control in laboratory than others. It was possible to control the temperature in the plan thanks to a magical wavelength configuration, however the absence of vertical strong confinement or cooling led to atom losses, limiting our experiment to only glimpses of the full gravitational collapse. The regimes of compression we observed surely can be made stronger if the atom lifetime is made longer than the collapse dynamical time.

Realizations of self-gravitating systems is often limited to numerical simulations, we encourage other teams to attempt the experiment with a tighter trapping. The success of such experiment would likely lead to new collaborations between atomic and statistical physicists. One use of long-range forces in atomic physics already known is the Rydberg blockade that has applications such as collective excitations [186], entanglement [23, 187], CNOT gates [188]. The dynamics of a superfluid is also sensitive to long-range dipole interactions [189]. But the interplay between degeneracy and long-range forces is difficult to control [190]. Collisions can also be tuned thanks to large magnetic moment atoms such as chromium and used to reduce atom losses due to inelastic collisions. Using gravitational-like forces with Fermionic cold atoms would pave the study of new phases of matter. It is reasonable to imagine reach regimes of compression -due to the long-range force- close to degeneracy and form a table-top white dwarf. Also, as compared to Coulombian or Dipolar interactions in cold atoms, the effective gravity is only attractive. It makes it simpler for testing general properties of long-range forces that are still an active field of research for theorists [13] and challenging for experimentalists [191].

Atom diffusion has been studied in the presence of three different beam configurations in two dimensions. We found no anomalous momentum diffusion that could explain the lower temperatures obtained in the 3/6 beam configurations. This study has been limited by time and will be continued in the next weeks, we wish indeed to explore more parameters for our numerical simulations and put a final answer on the commensurable values of the lattice step and mean distance traveled by the excited state. Many "hot" topics of the cold atom community concern many body effects. Diffusion in optical lattices is modified by localization [192]. The link between diffusion and thermalization is also a subject of research, as efforts are made to realize many body localization in higher dimensions [193, 194]. Localization in cold atoms is indeed associated with an ergodicity breaking: the relaxation time can be made extremely long in presence of many body effects. Thanks to the controllability of interactions within cold atoms experiments, experimentalists can nowadays access those strongly interacting regimes even with few millions of particles. This advantage over solid state physics experiments -which deals with much larger number of particles- is however highly dependent on the stability of the experimental setups. One important parameter being maintaining a high number of atoms or a low enough temperature during a cold atom experiment. Controlling the temperature thank to those many body localizations has been proposed recently in the context of quantum gases [195] to reduce losses in dynamical optical lattices. Another recent realization (see [196]) of a condensed matter effect by a cold atoms experiment consists in the so-called Thouless pump. By controlling adiabatically the parameters -such as a laser phase $\phi_i(t)$- of an optical lattice where atoms are evolving, a direct transport of particles can be obtained. Even if the transformation is periodic $\phi(t+T) = \phi(t)$, the particle transport is non-zero because of the topological properties of the transformation. Cold atoms are useful as one can control the optical lattice potential parameters in which they are evolving, a control one cannot have over a crystalline potential for instance. The direction toward which the transport is made is dictated by the direction of the -periodic- transformation.

In the third and final year of the thesis, we worked on the minimal conditions of appearance of a Brownian motor in 2D. A Brownian motor is a realistic example of Feynman ratchet. The idea of a Brownian motor is that it requires two thermal baths and a spatial asymmetry to obtain direct transport of particles. The asymmetry is required to give a direction, almost in the same way it is required for the Thouless pump. The difference however, is that the transport is obtained deterministically with the Thouless pump, while we focused on a transport obtained from thermal fluctuations. The system we considered was made of a classical particle confined by an asymmetric potential. We found that it requires two minimal conditions to obtain a direct transport of particles: two thermal baths to exchange energy and a spatial asymmetry to give a preferred direction for the system to work. This phenomenon is believed to be observable in cold atomic systems and leads to a stirring of the system. This phenomenon is also very general and fundamental to understand the competition between energy and information for small systems. It is known that no physical law is fundamentally irreversible. What makes our world irreversible is the unlikeliness of some peculiar occurrences. Irreversibility is important for the future of quantum computing and biology. As reducing the number and size of physical systems leads likely to bring back reversibility, those subjects of statistical physics are fundamental to understand how to engineer reliable quantum computing devices as well as understanding how evolution led to this level of efficiency in inheriting and preserving genetic and neuronal information.

Appendix A

Effect of optical lattices on temperature

Temperature is known to be modified in the presence of an optical lattice [197, 198, 199]. We will address in the following paragraphs this question in the presence of different 2D beam configurations. We are interested into laser beams driving the intercombination line of strontium, we take thus a simplified level structure $J_g = 0 \rightarrow J_e = 1$. In absence of magnetic field, there is a single atomic frequency ω_0.

For only beams with in-plane polarization, interferences modify the light intensity and resulting force. While for 4 beams at 90° no interferences occur between the two orthogonal directions, it is not the case for other laser configurations addressed experimentally, like 3 and 6 beams. We wish to simulate the effect of those geometries on the velocity diffusion and predict the temperature with a simple numerical simulation.

We write the i-th electric field lying in the x, y plan $\mathbf{E}_i = \cos(\mathbf{k}_i \cdot \mathbf{r} - \omega_L t + \phi_i)\boldsymbol{\epsilon}_i$ with $\boldsymbol{\epsilon}_i = R_z(\pi/2)\hat{\mathbf{k}}_i$. Where $R_z(\alpha)$ is the 2×2 matrix of rotation of angle α around the $\hat{z} = \hat{x} \wedge \hat{y}$ axis.

In the 3 beam configuration we have $\mathbf{k}_i = R_z(2\pi/3)\mathbf{k}_{i-1}$ where the matrix of rotation between each beam can be written as:

$$\begin{pmatrix} \cos(2\pi/3) & -\sin(2\pi/3) \\ \sin(2\pi/3) & \cos(2\pi/3) \end{pmatrix} = \begin{pmatrix} -\cos(\pi/3) & -\sin(\pi/3) \\ \sin(\pi/3) & -\cos(\pi/3) \end{pmatrix} = \begin{pmatrix} -c & -s \\ s & -c \end{pmatrix}. \tag{1.1}$$

Then the three wave vectors are

$$\hat{\mathbf{k}}_1 = (1, 0) \qquad \hat{\mathbf{k}}_2 = (-c, s) \qquad \hat{\mathbf{k}}_3 = (-c, -s), \tag{1.2}$$

and their polarization,

$$\boldsymbol{\epsilon}_1 = (0, 1) \qquad \boldsymbol{\epsilon}_2 = (-s, -c) \qquad \boldsymbol{\epsilon}_3 = (s, -c). \tag{1.3}$$

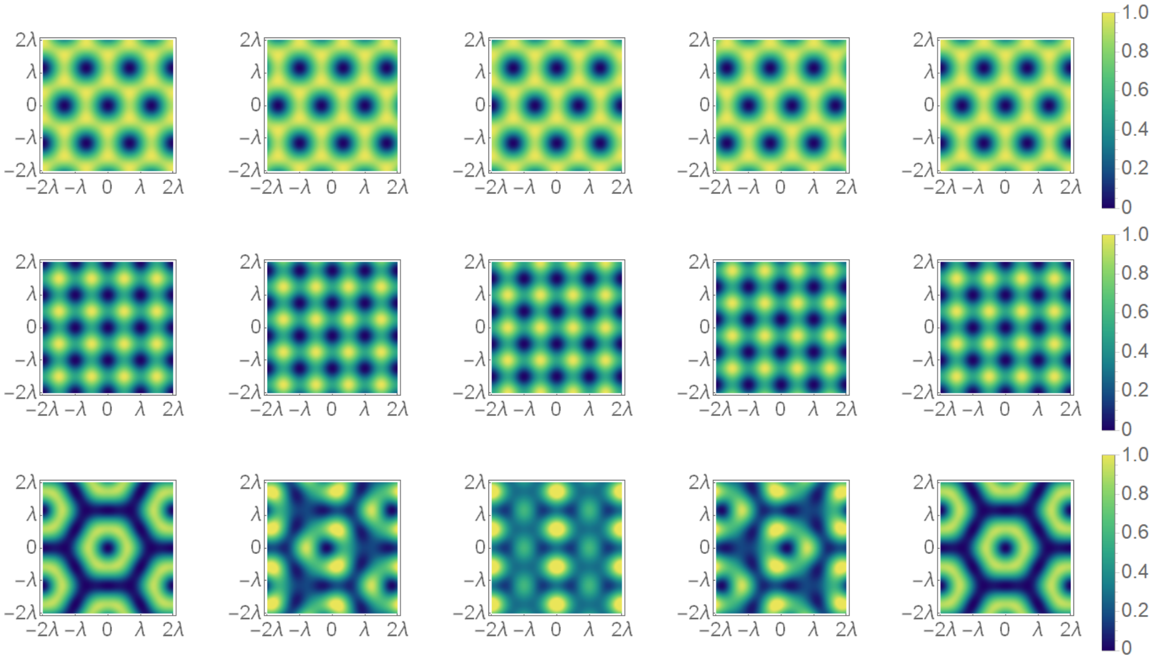

Fig. A.1 *Lattices intensities for the 3,4 and 6 beam configurations (top to bottom). The phase of one laser is increased of $\pi/2$ at each step (left to right). Space in λ units and intensities normalized by their maximum value per configuration.*

Obtaining the intensity is then done by computing the modulus square of the total electric field.

$$I_3(\mathbf{r}) = \frac{\omega}{2\pi}\int_0^{2\pi/\omega} dt \left|\sum_{i=1}^{3}\mathbf{E}_i(\mathbf{r},t)\right|^2 . \tag{1.4}$$

For 6 beams, we take the previous total electric field and add the contribution to their counter-propagating components by reversing the wave vector.

$$I_6(\mathbf{r}) = \frac{\omega}{2\pi}\int_0^{2\pi/\omega} dt \left(\sum_{i=1}^{3}\sum_{\pm\mathbf{k}_i}\mathbf{E}_i(\mathbf{r},t)\right)^2 . \tag{1.5}$$

The 4 beam case is easy because the two directions $\hat{x}$ and $\hat{y}$ don't interfere with each other and the total electric field is the sum of independent stationary waves. The wave-vectors and polarizations are

$$\hat{\mathbf{k}}_1 = (1,0) \qquad \hat{\mathbf{k}}_2 = (0,1), \tag{1.6}$$

and

$$\boldsymbol{\epsilon}_1 = (0,1) \qquad \boldsymbol{\epsilon}_2 = (-1,0), \tag{1.7}$$

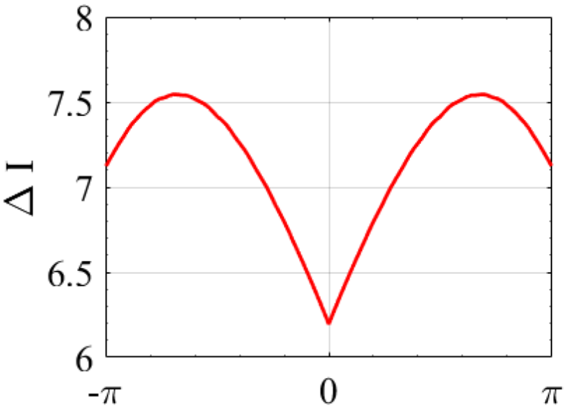

Fig. A.2 *Change in the max-min of intensity in the 6 beam configuration for a $[-\pi, \pi]$ phase shift of one laser.*

The intensity is given by a similar expression as for 6 beams

$$I_4(\mathbf{r}) = \frac{\omega}{2\pi} \int_0^{2\pi/\omega} dt \left(\sum_{i=1}^{2} \sum_{\pm \mathbf{k}_i} \mathbf{E}_i(\mathbf{r}, t) \right)^2 . \tag{1.8}$$

From those different intensities, we can already visualize roughly what the atom will experience if the phase of one of the laser drifts. Figure A.1, shows the previous intensity patterns. We pick randomly one laser in each configuration and observe the effect on the intensity for a phase shift of $\phi_n = n\pi/2$. The two first lines corresponding to 3 and 4 beam configurations are topologically invariant under a phase shift. The 6 beam configuration, corresponding to the third line is not and is subject to important variations. We can as well quantify the maximum intensity fluctuations from a complete frequency shift of one laser from 0 to 2π. We thus calculate the dipole force for an atom evolving in a low saturation $|\Omega| \ll |\delta|$ according to what follow. First, we place ourselves in the spherical base:

$$\boldsymbol{\epsilon}_0 = \mathbf{e}_z \quad \boldsymbol{\epsilon}_\pm = \mp \frac{\mathbf{e}_x \pm i\mathbf{e}_y}{\sqrt{2}} \quad \text{with} \quad \boldsymbol{\epsilon}_\pm \cdot \boldsymbol{\epsilon}_\pm^* = 1. \tag{1.9}$$

In this base, the scalar product of two vectors $\mathbf{A}$ and $\mathbf{B}$ is defined as:

$$\mathbf{A} \cdot \mathbf{B} = (\sum_q A_q \boldsymbol{\epsilon}_q^*) \cdot (\sum_{q'} (-)^{q'} B_q \boldsymbol{\epsilon}_{-q'}) = \sum_q (-)^q A_q B_{-q}, \tag{1.10}$$

where $q, q' \in \{-1, 0, +1\}$. As such the interaction Hamiltonian must be written:

$$\hat{H}_I = - \sum_{q=0,\pm} (-)^q \hat{d}_q E_{-q}. \tag{1.11}$$

The transition addressed by the 2D force is a $J_g = 0$ to $J_e = 1$ transition. The light is chosen polarized in the xy plane, if the quantization axis is chosen along $\hat{z}$

then two excited states $m_e = \pm 1$ are now involved in the problem. We generalize the operators $\hat{\sigma}_+ = |e\rangle\langle g|$ and $\hat{\sigma}_- = |e\rangle\langle g|$ for the two-level atom into operators including the fine structure [58]:

$$\hat{\sigma}(m_e, 0) = \hat{\sigma}^\dagger(0, me) = |J_e = 1, m_e = \pm 1\rangle\langle Jg = 0, m_g = 0| \,. \tag{1.12}$$

To calculate the dipole matrix elements from the dipole operator component $\hat{d}_q$, we multiply it by the closure relation on the left and on the right:

$$\begin{aligned} \hat{\mathbb{1}}\hat{d}_q\hat{\mathbb{1}} &= \sum_{m_e, m_g} \langle J_e, m_e|\, \hat{d}_q \,|J_g, m_g\rangle\, \hat{\sigma}(m_e, m_g) + \langle J_g, m_g|\, \hat{d}_q \,|J_e, m_e\rangle\, \hat{\sigma}(m_g, m_e) && (1.13)\\ &= \langle J_g|\, |\hat{\mathbf{d}}|\, |J_e\rangle \sum_{m_e, m_g} \langle J_g, m_g|J_e, m_e; 1, q\rangle\, \hat{\sigma}(m_g, m_e) && (1.14)\\ &\qquad + (-)^q \langle J_g, m_g|J_e, m_e; 1, q\rangle\, \hat{\sigma}^\dagger(m_g, m_e) && (1.15)\\ &= \hat{d}_q^{(+)} + \hat{d}_q^{(-)}, && (1.16) \end{aligned}$$

where the $(+)$(resp. $(-)$) exponent accounts for the atomic evolution of the average value of $\langle\hat{\sigma}(m_g, m_e)\rangle \propto e^{-i\omega_0 t}$ (resp. $\langle\hat{\sigma}(m_e, m_g)\rangle \propto e^{+i\omega_0 t}$). We also have made use of the Wigner-Eckart theorem [72] and made appear the reduced dipole element $\langle J_g|\, |\hat{\mathbf{d}}|\, |J_e\rangle$, a real quantity that does not depend on the Zeeman structure and thus is not modified by changing the quantization axis. Also appear terms depending on the Zeeman structure and thus on the geometry. Those terms $\langle J_g, m_g|J_e, m_e; 1, q\rangle$ are Clebsch-Gordan coefficients, they are responsible for the constraints on the allowed transitions for a given configuration of the electric field because of the constraint on the angular momentum conservation.

The spontaneous emission rate from a chosen excited state is linked to the total spontaneous emission rate Γ by:

$$\Gamma_{J_g, m_g; J_e, m_e} = |\langle J_e, m_e|J_g, mg; 1, m_e - m_g\rangle|^2\Gamma. \tag{1.17}$$

Knowing that the Weisskopf-Wigner decay rate Γ is modified due to the levels degeneracy as

$$\Gamma = \frac{\omega_0^3}{3\pi\epsilon_0\hbar c^3}\frac{2J_g + 1}{2J_e + 1}|\langle J_g|\, |\hat{\mathbf{d}}|\, |J_e\rangle|^2. \tag{1.18}$$

We also introduce the notation for the Rabi frequencies in the spherical basis. They include the spatial dependence of the electric field:

$$\Omega_q(\mathbf{r}) = -\frac{2}{\hbar}\langle J_g|\, |\hat{\mathbf{d}}|\, |J_e\rangle\, E_q^{(+)}(\mathbf{r}) \;\text{ and }\; \Omega_q^*(\mathbf{r}) = -(-)^q\frac{2}{\hbar}\langle J_g|\, |\hat{\mathbf{d}}|\, |J_e\rangle\, E_{-q}^{(-)}(\mathbf{r}). \tag{1.19}$$

Thus going back to the interaction Hamiltonian, we perform the rotating wave approximation (RWA) by associating the terms rotating at opposite frequency between the dipole operator and the electric field. We thus only keep the resonant terms, which is a good approximation for small detunings compare to the atomic and laser frequencies. We have then:

$$\begin{aligned} \hat{H}_I &= -\textstyle\sum_{q=0,\pm}(-)^q \hat{d}_q E_{-q} \\ \xrightarrow{RWA} H_I^{RWA} &= -\textstyle\sum_{q=0,\pm}(-)^q(\hat{d}_q^{(+)}E_{-q}^{(-)} + \hat{d}_q^{(-)}E_{-q}^{(+)}). \end{aligned}$$

Since we decided to put away the Clebsch-Gordan coefficients from the Rabi frequency we have to include them in the definition of the *geometrical* jump operators $\hat{\mathcal{S}}_q$:

$$\hat{\mathcal{S}}_q = \sum_{m_e,m_g} \langle J_g, m_g | J_e, m_e; 1, q\rangle \, \hat{\sigma}(m_g, m_e). \tag{1.20}$$

Finally, the Hamiltonian in the RWA becomes:

$$\hat{H}_I^{RWA} = \frac{\hbar}{2}\sum_q \Omega_q^* \hat{\mathcal{S}}_q + \Omega_q \hat{\mathcal{S}}_q^\dagger. \tag{1.21}$$

a) 4 beam configuration

In the 4 beam configuration, the total electric field is the superposition of two contra-propagating waves along $\hat{x}$ and $\hat{y}$, with a spatial phase chosen to have a minimum of intensity at the origin:

$$\mathbf{E}(\mathbf{r}, t) = E_0 \mathrm{Re}\left[-e^{-i(wt-ky)} + e^{-i(wt+ky)}\right]\mathbf{e}_x - \{x \leftrightarrow y\}. \tag{1.22}$$

The positive and negative components in frequency (and energy) of the electric field are written $\mathbf{E}^{(\pm)}$, where we recall they are respectively proportional to $\exp \mp i\omega t$. We then decompose those vectors in the spherical basis:

$$E_+^+ = -(E_-^-)^* = (E_-^+)^* = -E_+^- = \frac{E_0}{\sqrt{2}}[i\sin(ky) - \sin(kx)]. \tag{1.23}$$

In terms of Rabi frequencies, we have:

$$\Omega_+(\mathbf{r}) = -(\Omega_-(\mathbf{r}))^* = -\frac{E_0\sqrt{2}}{\hbar}\sqrt{\frac{3^2\Gamma\pi\epsilon_0\hbar c^3}{\omega_0^3}}[i\sin(ky) - \sin(kx)] \tag{1.24}$$

$$\Omega_0(\mathbf{r}) = 0. \tag{1.25}$$

It follows from the natural linewidth Γ, the expression of the modulus of the relevant Rabi frequencies:

$$|\Omega_\pm(\mathbf{r})|^2 = 3\Gamma^2 s_0[\sin^2(kx) + \sin^2(ky)], \tag{1.26}$$

and the jump operators:

$$\hat{\mathcal{S}}_{\pm} = \frac{1}{\sqrt{3}}\hat{\sigma}(0, \mp 1), \tag{1.27}$$

because

$$\langle 0, 0 | J, m; J', m' \rangle = \delta_{J,J'}\delta_{m,-m'}\frac{(-)^{J-m}}{\sqrt{2J+1}}. \tag{1.28}$$

The total Hamiltonian after the rotating-wave approximation in the $\{|0,0\rangle, |1,1\rangle, |1,-1\rangle\}$ basis is:

$$\hat{H}_I^{RWA} = \frac{\hbar}{2}\mathrm{diag}(\delta, -\delta, -\delta) + \frac{\hbar}{2\sqrt{3}}\begin{pmatrix} 0 & \Omega_-^* & \Omega_+^* \\ \Omega_- & 0 & 0 \\ \Omega_+ & 0 & 0 \end{pmatrix}. \tag{1.29}$$

Due to the symmetry of the problem (flip of the plane upside down) the two excited states are still degenerated, in and out the optical lattice: they always appear in a coherent superposition even in the diagonalized basis. To simplify we re-define also $\Omega_{\pm}(\mathbf{r})/\sqrt{3} \to \Omega_{\pm}(\mathbf{r})$. The eigen-energies are:

$$\begin{aligned} E_\alpha &= -\frac{\hbar\delta}{2}, \\ E_\beta &= -\frac{\hbar}{2}\sqrt{\delta^2 + |\Omega_+|^2 + |\Omega_-|^2}, \\ E_\gamma &= \frac{\hbar}{2}\sqrt{\delta^2 + |\Omega_+|^2 + |\Omega_-|^2}, \end{aligned} \tag{1.30}$$

with the *to be normalized* eigenstates:

$$\begin{aligned} |\alpha\rangle &= -\Omega_+^* |1,1\rangle + \Omega_-^* |1,-1\rangle, \\ |\beta\rangle &= (\delta - \sqrt{\delta^2 + |\Omega_+|^2 + |\Omega_-|^2}) |0,0\rangle + \Omega_- |1,1\rangle + \Omega_+ |1,-1\rangle, \\ |\gamma\rangle &= (\delta + \sqrt{\delta^2 + |\Omega_+|^2 + |\Omega_-|^2}) |0,0\rangle + \Omega_- |1,1\rangle + \Omega_+ |1,-1\rangle. \end{aligned} \tag{1.31}$$

The first eigenstates $|\alpha\rangle$, is not coupled to the ground state, and can be ignored because not populated. The system is two-level alike due to the symmetry of the situation. At large negative detuning and low intensity, the ground state is mainly connected to $|\beta\rangle$ while the excited states are connected to a coherent superposition of $|\alpha\rangle$ and $|\gamma\rangle$. The average dipole force that will experience an atom in the ground state will be $\mathbf{F}_g \approx -\nabla E_\beta$ while an atom in either one of the excited states will experience a force $\mathbf{F}_e = -\mathbf{F}_g \approx -\nabla E_\gamma$. We are almost back to the result of a two-level atom in a far-detuned dipole potential that experiences a force related to the gradient of its potential energy, the forces being opposite in the ground and the excited state [37]. The expression of the force is then:

$$\mathbf{F}_g(\mathbf{r}) = -\mathbf{F}_e(\mathbf{r}) = \frac{\hbar k \Gamma^2 s_0}{2} \frac{\sin(2kx)\mathbf{e}_x + \sin(2ky)\mathbf{e}_y}{\sqrt{\delta^2 + 2\Gamma^2 s_0(\sin^2(kx) + \sin^2(ky))}}. \tag{1.32}$$

b) 3 beam configuration

The spherical basis components for the electric field are:

$$\begin{aligned} E_+^+(\mathbf{r}) = -E_-^-(\mathbf{r})^* = E_0 \frac{e^{-i\frac{k}{2}\left(x+\sqrt{3}y\right)} \left(2ie^{i\frac{k}{2}\left(3x+\sqrt{3}y\right)} + \left(\sqrt{3}-i\right) e^{ik\sqrt{3}y} - i - \sqrt{3}\right)}{4\sqrt{2}}, \\ E_-^+(\mathbf{r}) = -E_+^-(\mathbf{r})^* = E_0 \frac{e^{-i\frac{k}{2}\left(x+\sqrt{3}y\right)} \left(2ie^{i\frac{k}{2}\left(3x+\sqrt{3}y\right)} - \left(\sqrt{3}+i\right) e^{ik\sqrt{3}y} - i + \sqrt{3}\right)}{4\sqrt{2}}. \end{aligned} \tag{1.33}$$

The associated Rabi frequencies are thus unequal in modulus:

$$\begin{aligned} |\Omega_\pm(\mathbf{r})|^2 = \frac{3\Gamma^2 s_0}{4} \Bigg[& 3 - \cos ky\sqrt{3} \\ & \pm 2\cos\frac{3kx}{2}\left[\sqrt{3}\sin\frac{ky\sqrt{3}}{2} \mp \cos\frac{ky\sqrt{3}}{2}\right] \mp \sqrt{3}\sin ky\sqrt{3}\Bigg]. \end{aligned} \tag{1.34}$$

However, the Hamiltonian structure is the same, we simply separate the two different Rabi frequencies when writing the eigen-energies, and we remove the factors 3, just as before thank to the following change: $\Omega_\pm(\mathbf{r})/\sqrt{3} \to \Omega_\pm(\mathbf{r})$. The two-level atom picture holds again because of the symmetry: an atom absorbing a photon in this optical lattice, will be put in a coherent superposition of the two excited states. Even if the weight of those states depends on the position (different Rabi frequencies), the force is proportional to the summed squares of the two frequencies. We thus take advantage again of this simplified model to summarize everything as a two-level atom. The forces are then:

$$\begin{aligned} \mathbf{F}_g(\mathbf{r}) &= -\mathbf{F}_e(\mathbf{r}) = -\nabla E_\beta \\ &= \frac{\hbar k \Gamma^2 s_0}{8} \frac{3\cos\frac{ky\sqrt{3}}{2}\sin\frac{3kx}{2}\mathbf{e}_x + \sqrt{3}\left(\cos\frac{3kx}{2} + 2\cos\frac{ky\sqrt{3}}{2}\right)\sin\frac{ky\sqrt{3}}{2}\mathbf{e}_y}{\sqrt{\delta^2 + \frac{\Gamma^2 s_0}{2}(3 - 2\cos\frac{3kx}{2}\cos\frac{ky\sqrt{3}}{2} - \cos ky\sqrt{3})}}. \end{aligned} \tag{1.35}$$

c) 6 beam configuration

The spherical basis components for the electric field are:

$$\begin{aligned} E^+_+(\mathbf{r}) &= -E^-_-(\mathbf{r})^* = \frac{E_0}{\sqrt{2}}\left(-\cos\frac{ky\sqrt{3}}{2}\sin\frac{kx}{2} - \sin kx + i\sqrt{3}\cos\frac{kx}{2}\sin\frac{ky\sqrt{3}}{2}\right), \\ E^+_-(\mathbf{r}) &= -E^-_+(\mathbf{r})^* = E^+_+(\mathbf{r})^*. \end{aligned} \tag{1.36}$$

The associated Rabi frequencies are this time equal in modulus:

$$|\Omega_+(\mathbf{r})|^2 = |\Omega_-(\mathbf{r})|^2 = 3\Gamma^2 s_0\left[\left(\cos\frac{ky\sqrt{3}}{2}\sin\frac{kx}{2} + \sin kx\right)^2 + 3\cos^2\frac{kx}{2}\sin^2\frac{ky\sqrt{3}}{2}\right]. \tag{1.37}$$

Also, the Hamiltonian structure is the same, we simply separate the two different Rabi frequencies when writing the eigen-energies, and we get rid once more of the factors 3 as for the two previous configurations. The force expression is too long to be displayed here.

d) Method

The single atom dynamic is solved using a velocity Verlet algorithm:

$$\mathbf{r}(t+\Delta t) = \mathbf{r}(t) + \mathbf{v}(t)\Delta t + \frac{\mathbf{F}(t)}{2m}\Delta t^2, \tag{1.38}$$

$$\mathbf{v}(t+\Delta t) = \mathbf{v}(t) + \frac{\mathbf{f}(t) + \mathbf{F}(t+\Delta t)}{2m}\Delta t. \tag{1.39}$$

Where $\mathbf{F}_{e/g}(t)$ is the dipole force in either the ground or excited state. We rescale space variables $\{x_i\} = \{x, y\}$ and time t as:

$$x_i \to \frac{\tilde{x}_i}{k} \qquad t \to \frac{\tilde{t}}{\Gamma}. \tag{1.40}$$

It comes that the new velocity unit is Γk^{-1} and the consequent rescaling for the force is then:

$$\mathbf{F}_{e/g}(\mathbf{r}(t)) \to \tilde{\mathbf{F}}_{e/g}(\mathbf{r}(\mathbf{t})) = \frac{k}{\Gamma^2}\mathbf{F}_{e/g}(\mathbf{r}(\mathbf{t})), \tag{1.41}$$

which for example, gives for the ground state within the 4 beam configuration:

$$\tilde{\mathbf{F}}_g(\tilde{\mathbf{r}}(\tilde{t})) = \frac{\hbar k^2 s_0}{2}\frac{\sin(2\tilde{x})\mathbf{e}_x + \sin(2\tilde{y})\mathbf{e}_y}{\sqrt{\delta^2 + 2\Gamma^2 s_0(\sin^2(\tilde{x}) + \sin^2(\tilde{y}))}}. \tag{1.42}$$

The simulation is based on the general principle of a Monte Carlo scheme: one atom evolves deterministically in the optical lattice under the effect of dipole forces until (here the probabilistic part) it absorbs instantaneously a photon (radiation pressure) or spontaneously emit a previously absorbed one. The recoil due to those events is known in direction and amplitude since we known the radiation pattern. The velocity distribution is sampled in order to access the probability distribution function $g(v)$ for a given detuning and saturation parameter of the light field.

e) Results

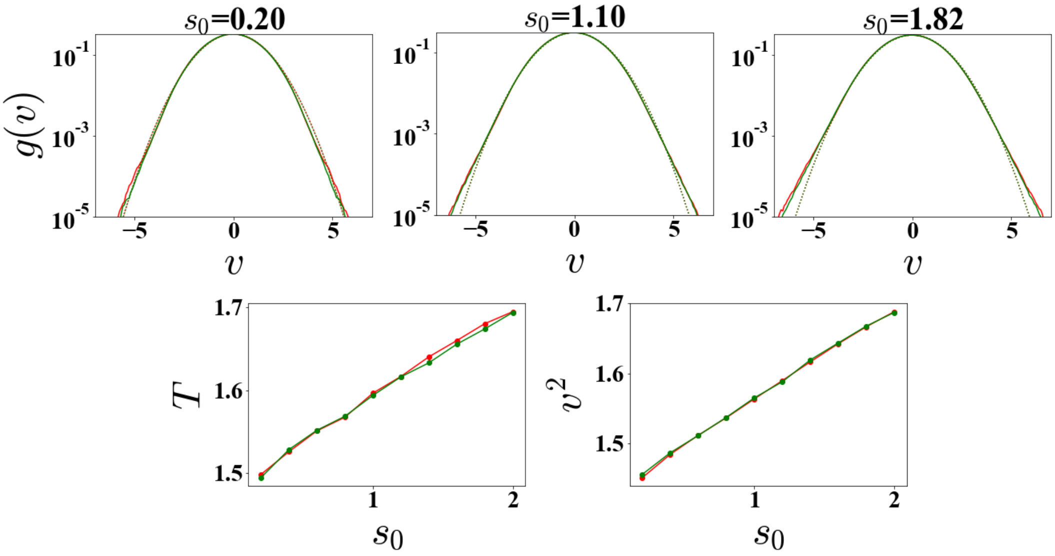

Fig. A.3 *(top) Velocity distributions in absence of the dipole force in the 3 beam configuration. (bottom left) Gaussian RMS. (bottom right) Distribution RMS. Plots in rescaled units.*

We repeated the simulations in absence and in presence of the dipole force, but always with the radiation pressure to ensure the thermalization. The detuning of the laser beams is fixed to -4Γ. Each of the three beam configurations (3 beams, 4 beams and 6 beams) were simulated. The top Figures A.3 show the evolution -for the 3 beam configuration- of the velocity probability distribution function $g(v)$ in absence of the dipole force and for different values of the saturation parameter s_0. Although we assumed a low saturation, we display curves up to a saturation parameter of almost 2: we are allowed to increase s_0 because we work with a large detuning here.

The green (respectively red) continuous curve is representing the distribution along $\hat{x}$ (respectively $\hat{y}$). They are fitted by Gaussian functions, represented by the dotted curves. We see deviation from the Gaussian fits when the saturation parameter is increasing. Globally the distribution becomes wider as we increase the saturation parameter, which indicates an increase of the temperature. The bottom Figures A.3 show respectively the Gaussian fit second moment "T" (bottom left) and the sampled distribution second moment "v^2" (bottom right). They barely differ in absence of the dipole force. The same curves in presence of the dipole force are plotted in Figures A.4. We notice a global heating in presence of the dipole force. We also notice discrepancies between the velocity RMS along $\hat{x}$ and $\hat{y}$. The discrepancies are larger when calculated from the Gaussian fit. In the 3 beam configuration, the inequivalence between those two directions of the optical lattice may explain -at first sight- this difference; However, the discrepancy seemingly disappears when increasing s_0, which suggests rather that it originates from a statistical reason. Indeed, the tail deviations from the Gaussian, appear to smoothen for larger s_0.

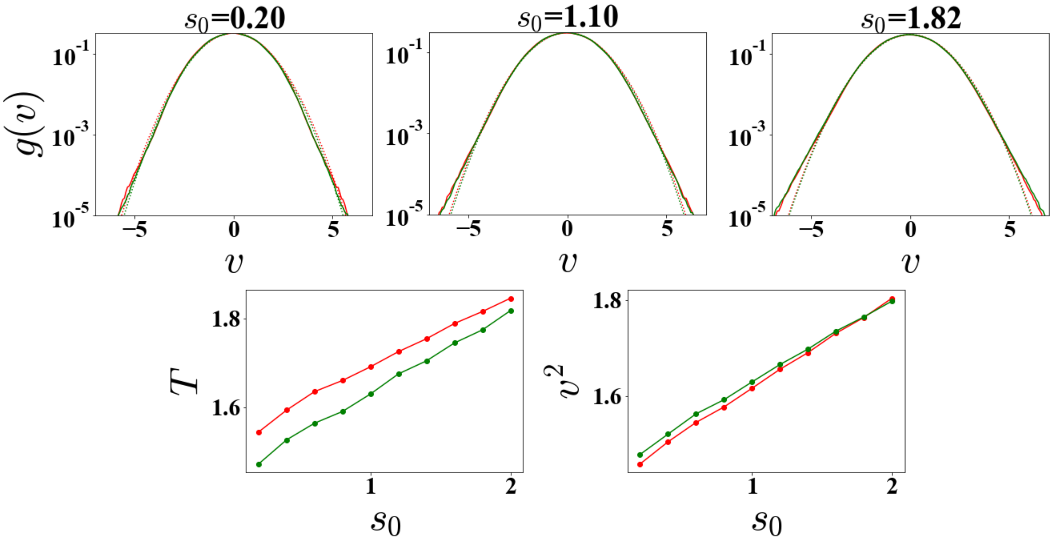

Fig. A.4 *(top) Velocity distributions in presence of the dipole force. (bottom left) Gaussian RMS. (bottom right) Distribution RMS. Plots in rescaled units.*

The curves giving the temperatures in the different beam configurations after rescaling to the physical variables are given in Figure A.5. The top two figures give the real temperature T, in microkelvins, in the different configurations when varying the intensity per beam. Without dipole force (blue data), temperatures are on average lower than with forces (red date). When the dipole force is taken into account, the $T(s_0)$ data seem to have a slope scaling as the number of beams. It is confirmed by looking at the temperatures versus the total intensity Σs_0 per configuration: *cf.* the two bottom figures in Figure A.5. Without dipoles forces, the three beam configurations give the same linear behavior as a function of the total intensity. On the other hand, when the dipole forces are added, one find small discrepancies in the 6 beam configuration with respect to the 3/4 beam configurations. Again, the addition of the dipole force results in a slight increase of the temperature.

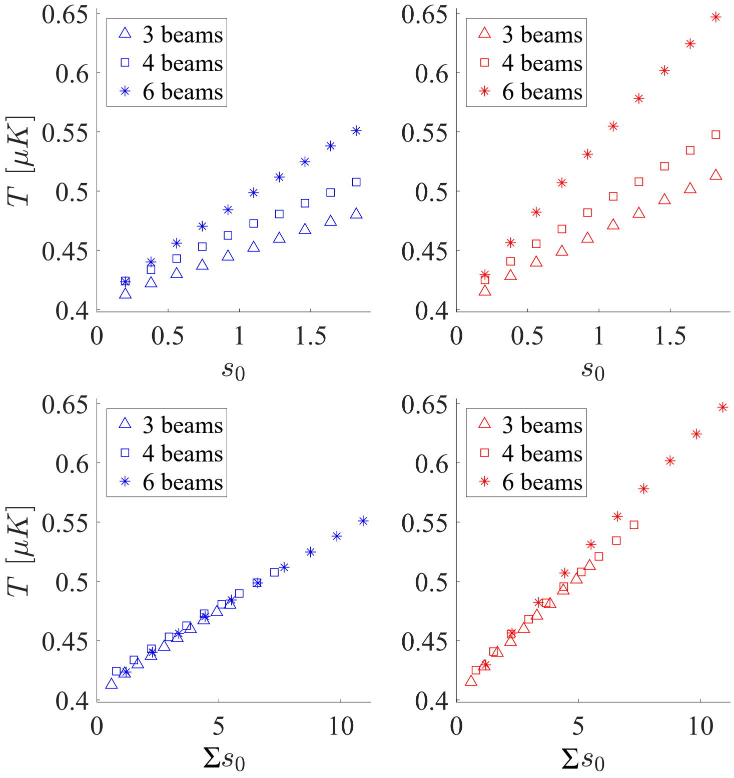

Fig. A.5 *Real temperature* T *in absence (blue curves) and in presence (red curves) of dipole forces. Represented respectively versus the intensity per beam* s_0 *(Top) and total intensity* Σs_0 *(bottom).*

We found thus no quantitative evidence at a fixed detuning of -4Γ, that any beam configuration gives deviations from the semi-classical theory [38] nor from the full quantum treatment [39]. Those two are known to be close from each others for large enough detuning or saturation parameter.

Appendix B

Covariance matrix

We first introduce the method allowing to obtain the complete solution of the two above models. Indeed, the models belong to the class of linear multivariate Fokker-Planck equations[200, 201]. Let us denote $\mathbf{x}$ a d-dimensional vector, the linear Fokker-Planck equation is given by

$$\frac{\partial f(\mathbf{x},t)}{\partial t} = -\sum_{i,j} A_{ij} \frac{\partial x_j f(\mathbf{x},t)}{\partial x_i} + \frac{1}{2} B_{ij} \frac{\partial^2}{\partial x_i \partial x_j} f(\mathbf{x},t). \tag{2.1}$$

The solutions of this linear Fokker-Planck equation are Gaussian distributions:

$$f(\mathbf{x},t) = \frac{1}{\sqrt{(2\pi)^d \mathrm{Det}(\Xi)}} \exp\left(-\frac{1}{2}(\mathbf{x} - \langle \mathbf{x} \rangle)^T \Xi^{-1} (\mathbf{x} - \langle \mathbf{x} \rangle)\right) \tag{2.2}$$

where $\langle \quad \rangle$ denote the statistical average over the variable, $\mathbf{x}^T$ the transpose of $\mathbf{x}$ and $\Xi \equiv \Xi(t)$ is a time dependent $d \times d$ covariance matrix. By taking the first and the second moment of the Fokker-equation, the covariance matrix satisfies the differential equation

$$\frac{d\Xi}{dt} = A\Xi + \Xi A^T + B \tag{2.3}$$

where A and B are $r \times r$ matrices with coefficients A_{ij} and B_{ij}, respectively.

Note that for the two models defined above, the matrices A and B are symmetric. Moreover, for the sake of simplicity, one first considers the stationary solution, where the stationary covariance matrix is denoted as Ξ_s obeying to the algebraic equation

$$A\Xi + \Xi^T A = -B. \tag{2.4}$$

Appendix C

Langevin algorithm

The 1D Langevin equations for a linear friction coefficient α and an associated Gaussian white noise $\xi(t)$ are:

$$\begin{aligned} \dot{x}(t) &= v(t), \\ m\dot{v}(t) &= F(t) - \eta v(t) + \xi(t) \end{aligned} \tag{3.1}$$

which -using the notation $x^n = x(t)$, $x^{n+1} = x(t + \mathrm{d}t)$ etc.- can be integrated over a small time interval $[t, t + \mathrm{d}t]$ to give[1]:

$$x^{n+1} - x^n = \frac{1}{2}(v^{n+1} + v^n), \tag{3.2}$$

$$m(v^{n+1} - v^n) = -\eta(x^{n+1} - x^n) + \xi^{n+1} + \int_t^{t+\mathrm{d}t} \mathrm{d}t' f(t'), \tag{3.3}$$

where $\xi^{n+1} = \int_t^{t+\mathrm{d}t} dt' \xi(t')$ is also a random number obeying:

$$\langle \xi^n \rangle = 0 \quad \text{and} \quad \langle \xi^n \xi^m \rangle = 2\alpha k_B T \, \mathrm{d}t \delta_{nm}, \tag{3.4}$$

in virtue of the properties of $\xi(t)$. Substituting v^{n+1} from Equation 3.3 into Equation 3.2 yields:

$$x^{n+1} = x^n + b \, \mathrm{d}t v^n + \frac{b \, \mathrm{d}t}{2m} \xi^{n+1} + \frac{b \, \mathrm{d}t}{2m} \int_t^{t+\mathrm{d}t} \mathrm{d}t' f(t'), \tag{3.5}$$

where $b = (1 + \frac{\eta \, \mathrm{d}t}{2m})$. Expanding the deterministic force integral of Equations 3.5 and 3.3 gives:

---

[1] First equation given by Riemann midpoint sum and second by straight integration.

$$
\begin{aligned}
x^{n+1} &= x^n + b\,\mathrm{d}t v^n + \frac{b\,\mathrm{d}t}{2m}\xi^{n+1} + \frac{b\,\mathrm{d}t^2}{2m} f^n,\\
v^{n+1} &= v^n - \frac{\eta}{m}(x^{n+1} - x^n) + \frac{1}{m}\xi^{n+1} + \frac{\mathrm{d}t}{2m}(f^{n+1} + f^n).
\end{aligned} \tag{3.6}
$$

This first algorithm uses only one random generator per time-step and gives access to the velocity. One can eliminate the velocity from 3.6 and obtains:

$$
x^{n+1} = 2bx^n - ax^{n-1} + \frac{b\,\mathrm{d}t^2}{m} f^n + \frac{b\,\mathrm{d}t}{2m}(\xi^{n+1} + \xi^n), \tag{3.7}
$$

where $a = (1 - \frac{\eta\,\mathrm{d}t}{2m})/(1 + \frac{\eta\,\mathrm{d}t}{2m})$. This formulation of the algorithm trades the intermediate velocity for an additional random number per time-step.

Bibliography

[1] A. A. Vlasov; «The vibrational properties of an electron gas»; Soviet Physics Uspekhi **10**, p. 721–733 (1968). 4

[2] M. Kac, G. E. Uhlenbeck & P. C. Hemmer; «On the van der Waals Theory of the Vapor-Liquid Equilibrium. I. Discussion of a One-Dimensional Model»; J. Math. Phys. **4**, p. 216–228 (1963). 4

[3] H. Touchette; «Equivalence and Nonequivalence of Ensembles: Thermodynamic, Macrostate, and Measure Levels»; J. Stat. Phys. **159**, p. 987–1016 (2015). 6

[4] M. Blume; «Theory of the First-Order Magnetic Phase Change in UO_2»; Phys. Rev. **141**, p. 517–524 (1966). 6

[5] H. Capel; «On the possibility of first-order phase transitions in Ising systems of triplet ions with zero-field splitting»; Physica **32**, p. 966–988 (1966). 6

[6] J. Barré, D. Mukamel & S. Ruffo; «Inequivalence of Ensembles in a System with Long-Range Interactions»; Phys. Rev. Lett. **87** (2001). 7

[7] H. Touchette, R. S. Ellis & B. Turkington; «An introduction to the thermodynamic and macrostate levels of nonequivalent ensembles»; Physica A **340**, p. 138–146 (2004). 7

[8] F. Bouchet & J. Barré; «Classification of Phase Transitions and Ensemble Inequivalence, in Systems with Long Range Interactions»; J. Stat. Phys. **118**, p. 1073–1105 (2005). 8

[9] P. de Buyl, G. D. Ninno, D. Fanelli *et al.*; «Absence of thermalization for systems with long-range interactions coupled to a thermal bath»; Phys. Rev. E **87** (2013). 8

[10] D. Mukamel, S. Ruffo & N. Schreiber; «Breaking of Ergodicity and Long Relaxation Times in Systems with Long-Range Interactions»; Phys. Rev. Lett. **95** (2005). 9

[11] G. Venkataraman, D. Sahoo & V. Balakrishnan; *Beyond the Crystalline State* (Springer Berlin Heidelberg) (1989). 8

[12] F. P. da C. Benetti, T. N. Teles, R. Pakter *et al.*; «Ergodicity Breaking and Parametric Resonances in Systems with Long-Range Interactions»; Phys. Rev. Lett. **108** (2012). 10

[13] A. Campa, T. Dauxois, D. Fanelli *et al.*; *Physics of Long-Range Interacting Systems* (Oxford University Press) (2014). 10, 114

[14] A. Fioretti, D. Comparat, C. Drag *et al.*; «Long-Range Forces between Cold Atoms»; Phys. Rev. Lett. **82**, p. 1839–1842 (1999). 11

[15] N. Saquet, A. Cournol, J. Beugnon *et al.*; «Landau-Zener Transitions in Frozen Pairs of Rydberg Atoms»; Phys. Rev. Lett. **104** (2010). 11

[16] E. Altiere, D. P. Fahey, M. W. Noel *et al.*; «Dipole-dipole interaction between rubidium Rydberg atoms»; Phys. Rev. A **84** (2011). 11

[17] D. O'Dell, S. Giovanazzi, G. Kurizki *et al.*; «Bose-Einstein Condensates with $1/r$ Attraction: Electromagnetically Induced "Gravity"»; Phys. Rev. Lett. **84**, p. 5687–5690 (2000). 11

[18] I. Waki, S. Kassner, G. Birkl *et al.*; «Observation of ordered structures of laser-cooled ions in a quadrupole storage ring»; Physical Review Letters **68**, p. 2007–2010 (1992). 11

[19] M. G. Raizen, J. M. Gilligan, J. C. Bergquist *et al.*; «Ionic crystals in a linear Paul trap»; Physical Review A **45**, p. 6493–6501 (1992). 11

[20] R. C. Thompson; «Ion Coulomb crystals»; Contemporary Physics p. 1–17 (2015). 11

[21] D. Jaksch, J. I. Cirac, P. Zoller *et al.*; «Fast Quantum Gates for Neutral Atoms»; Phys. Rev. Lett. **85**, p. 2208–2211 (2000). 11

[22] E. Urban, T. A. Johnson, T. Henage *et al.*; «Observation of Rydberg blockade between two atoms»; Nat. Phys. **5**, p. 110–114 (2009). 11

[23] T. Wilk, A. Gaëtan, C. Evellin *et al.*; «Entanglement of Two Individual Neutral Atoms Using Rydberg Blockade»; Phys. Rev. Lett. **104** (2010). 11, 113

[24] Y. Zeng, P. Xu, X. He *et al.*; «Entangling Two Individual Atoms of Different Isotopes via Rydberg Blockade»; Phys. Rev. Lett. **119** (2017). 11

[25] S. Möbius, M. Genkin, A. Eisfeld *et al.*; «Entangling distant atom clouds through Rydberg dressing»; Phys. Rev. A **87** (2013). 11

[26] A. Dominguez, M. Oettel & S. Dietrich; «Dynamics of colloidal particles with capillary interactions»; Phys. Rev. E **82** (2010). 11

[27] R. Golestanian; «Collective Behavior of Thermally Active Colloids»; Phys. Rev. Lett. **108** (2012). 11

[28] M. Chalony, J. Barré, B. Marcos *et al.*; «Long-range one-dimensional gravitational-like interaction in a neutral atomic cold gas»; Phys. Rev. A **87** (2013). 11, 19, 21, 34, 87

[29] G. L. Camm; «Self-gravitating star systems»; Mon. Not. R. Astron. Soc. **110**, p. 305 (1950). 11, 19

[30] K. R. Yawn & B. N. Miller; «Incomplete relaxation in a two-mass one-dimensional self-gravitating system»; Phys. Rev. E **68** (2003). 11

[31] C. Cohen-Tannoudji, J. Dupont-Roc & G. Grynberg (rédacteurs); *Photons and Atoms* (Wiley-VCH Verlag GmbH) (1997). 14, 34, 35

[32] N. V. Kampen; *Stochastic Processes in Physics and Chemistry, Third Edition* (North Holland) (2007); ISBN 978-0-444-52965-7. 15, 92

[33] J. Dalibard & C. Cohen-Tannoudji; «Atomic motion in laser light: connection between semiclassical and quantum descriptions»; J. Phys. B: At. Mol. Phys. **18**, p. 1661 (1985). 15

[34] M. Joyce & T. Worrakitpoonpon; «Relaxation to thermal equilibrium in the self-gravitating sheet model»; J. Stat. Mech: Theory Exp. **2010**, p. P10 012 (2010). 16

[35] F. Baldovin, P.-H. Chavanis & E. Orlandini; «Microcanonical quasistationarity of long-range interacting systems in contact with a heat bath»; Phys. Rev. E **79** (2009). 16

[36] Y. L. Klimontovich; «Nonlinear Brownian motion»; Phys. Usp. **37**, p. 737–766 (1994). 16, 17

[37] B. Bransden & C. Joachain; *Physics of Atoms and Molecules (2nd Edition)* (Pearson) (2003); ISBN 058235692X. 16, 40, 50, 122

[38] P. D. Lett, W. D. Phillips, S. L. Rolston *et al.*; «Optical molasses»; J. Opt. Soc. Am. B **6**, p. 2084 (1989). 16, 127

[39] Y. Castin, H. Wallis & J. Dalibard; «Limit of Doppler cooling»; J. Opt. Soc. Am. B **6**, p. 2046 (1989). 16, 36, 127

[40] M. Chalony, A. Kastberg, B. Klappauf *et al.*; «Doppler Cooling to the Quantum Limit»; Phys. Rev. Lett. **107** (2011). 16, 110

[41] J. Barré, B. Marcos & D. Wilkowski; «Nonequilibrium Phase Transition with Gravitational-like Interaction in a Cloud of Cold Atoms»; Phys. Rev. Lett. **112** (2014). 17, 22, 23, 24, 30, 31, 70

[42] C. Sire & P.-H. Chavanis; «Thermodynamics and collapse of self-gravitating Brownian particles in D dimensions»; Phys. Rev. E **66** (2002). 19, 21

[43] T. Padmanabhan; «Statistical mechanics of gravitating systems»; Phys. Rep. **188**, p. 285–362 (1990). 19

[44] A. Olivetti, J. Barré, B. Marcos *et al.*; «Breathing Mode for Systems of Interacting Particles»; Phys. Rev. Lett. **103** (2009). 21

[45] P.-H. Chavanis, C. Rosier & C. Sire; «Thermodynamics of self-gravitating systems»; Phys. Rev. E **66** (2002). 21, 23

[46] R. H. Miller; «On the "thermodynamics" of Self-Gravitating N-Body Systems»; The Astrophysical Journal **180**, p. 759 (1973). 24

[47] M. C. Sormani & G. Bertin; «Gravothermal catastrophe: The dynamical stability of a fluid model»; Astronomy & Astrophysics **552**, p. A37 (2013). 24

[48] E. T. Jaynes; «Gibbs vs Boltzmann Entropies»; Am. J. Phys **33**, p. 391–398 (1965). 24

[49] V. A. Antonov; «Solution of the problem of stability of stellar system Emden's density law and the spherical distribution of velocitie s»; in Vest. Leningrad Univ. 7 135 (in Russian). English translation in Dynamics of star clusters, eds. J. Goodman, & P. Hut (Dordrecht: Reidel), IAU Symp. 113, 525 (1962). 24

[50] V. Springel; «The cosmological simulation code gadget-2»; Mon. Not. R. Astron. Soc. **364**, p. 1105–1134 (2005). 24

[51] J. A. Izaguirre, C. R. Sweet & V. S. Pande; «Multiscale dynamics of macromolecules using normal mode Langevin»; dans «Biocomputing 2010», p. 240–251 (WORLD SCIENTIFIC) (2009). 25

[52] D. E. Knuth; *The Art of Computer Programming* (Pearson Education (US)) (2008); ISBN 0321534964. 25

[53] E. F. Keller & L. A. Segel; «Initiation of slime mold aggregation viewed as an instability»; J. Theor. Biol. **26**, p. 399–415 (1970). 30

[54] P. M. Lushnikov; «Critical chemotactic collapse»; Phys. Lett. A **374**, p. 1678–1685 (2010). 30

[55] I. S. Milton Abramowitz; *Handbook of Mathematical Functions: with Formulas, Graphs, and Mathematical Tables* (Dover Publications) (1965); ISBN 0-486-61272-4. 32

[56] H. Katori, T. Ido, Y. Isoya *et al.*; «Magneto-Optical Trapping and Cooling of Strontium Atoms down to the Photon Recoil Temperature»; Phys. Rev. Lett. **82**, p. 1116–1119 (1999). 34, 60, 110

[57] J. D. Jackson; *Classical Electrodynamics Third Edition* (Wiley) (1998); ISBN 0-471-30932-X. 34

[58] D. A. Steck; *Quantum and Atom Optics* (available online at http://steck.us/teaching) (2018). 34, 40, 120

[59] D. W. Sesko, T. G. Walker & C. E. Wieman; «Behavior of neutral atoms in a spontaneous force trap»; J. Opt. Soc. Am. B **8**, p. 946 (1991). 35, 109

[60] J. Dalibard & C. Cohen-Tannoudji; «Dressed-atom approach to atomic motion in laser light: the dipole force revisited»; J. Opt. Soc. Am. B **2**, p. 1707 (1985). 36

[61] D. M. Stamper-Kurn, M. R. Andrews, A. P. Chikkatur *et al.*; «Optical Confinement of a Bose-Einstein Condensate»; Phys. Rev. Lett. **80**, p. 2027–2030 (1998). 38

[62] P. D. Lett, P. S. Julienne & W. D. Phillips; «Photoassociative Spectroscopy of Laser-Cooled Atoms»; Annu. Rev. Phys. Chem. **46**, p. 423–452 (1995). 38

[63] T. Zelevinsky, M. M. Boyd, A. D. Ludlow *et al.*; «Narrow Line Photoassociation in an Optical Lattice»; Phys. Rev. Lett. **96** (2006). 38

[64] Y. N. M. de Escobar, P. G. Mickelson, P. Pellegrini *et al.*; «Two-photon photoassociative spectroscopy of ultracold ^{88}Sr»; Phys. Rev. A **78** (2008). 38

[65] R. Ciuryło, E. Tiesinga, S. Kotochigova *et al.*; «Photoassociation spectroscopy of cold alkaline-earth-metal atoms near the intercombination line»; Phys. Rev. A **70** (2004). 38

[66] W. Skomorowski, R. Moszynski & C. P. Koch; «Formation of deeply bound ultracold Sr$_2$molecules by photoassociation near the1S+3P1intercombination line»; Phys. Rev. A **85** (2012). 38

[67] R. Grimm, M. Weidemüller & Y. B. Ovchinnikov; «Optical Dipole Traps for Neutral Atoms»; dans «Advances In Atomic, Molecular, and Optical Physics», p. 95–170 (Elsevier) (2000). 38, 78

[68] H. Katori, T. Ido & M. Kuwata-Gonokami; «Optimal Design of Dipole Potentials for Efficient Loading of Sr Atoms»; J. Phys. Soc. Jpn. **68**, p. 2479–2482 (1999). 38, 41

[69] M. Boyd; *High Precision Spectroscopy of Strontium in an Optical Lattice: Towards a New.*; Thèse de doctorat; University of Washington (2002). 38, 53

[70] R. C. Hilborn; «Einstein coefficients, cross sections, f values, dipole moments, and all that»; Am. J. Phys **50**, p. 982–986 (1982). 40

[71] V. Weisskopf & E. Wigner; «Berechnung der natürlichen Linienbreite auf Grund der Diracschen Lichttheorie»; Zeitschrift für Physik **63**, p. 54–73 (1930). 40

[72] C. Cohen-Tannoudji, B. Diu & F. Laloe; *Quantum Mechanics* (Wiley) (1991); ISBN 047116433X. 40, 120

[73] O. Svelto; *Principles of Lasers* (Springer US) (2010). 42

[74] H. J. Andrä, H.-J. Plöhn, W. Wittmann *et al.*; «Lifetimes of levels in neutral strontium (Sr I)»; J. Opt. Soc. Am. **65**, p. 1410 (1975). 45

[75] W. H. Parkinson, E. M. Reeves & F. S. Tomkins; «Neutral calcium, strontium and barium: determination of f values of the principal series by the hook method»; J. Phys. B: At. Mol. Phys. **9**, p. 157–165 (1976). 45

[76] D. A. Miller, L. You, J. Cooper *et al.*; «Collisional energy transfer between excited-state strontium and noble-gas atoms»; Phys. Rev. A **46**, p. 1303–1309 (1992). 45

[77] H. G. C. Werij, C. H. Greene, C. E. Theodosiou *et al.*; «Oscillator strengths and radiative branching ratios in atomic Sr»; Phys. Rev. A **46**, p. 1248–1260 (1992). 45

[78] T. Ido & H. Katori; «Recoil-Free Spectroscopy of Neutral Sr Atoms in the Lamb-Dicke Regime»; Phys. Rev. Lett. **91** (2003). 45

[79] P. G. Mickelson, Y. N. Martinez, A. D. Saenz *et al.*; «Spectroscopic Determination of thes-Wave Scattering Lengths of ^{86}Sr and ^{88}Sr»; Phys. Rev. Lett. **95** (2005). 45, 51

[80] I. Ushijima, M. Takamoto, M. Das *et al.*; «Cryogenic optical lattice clocks»; Nat. Photonics **9**, p. 185–189 (2015). 47

[81] S. Häfner, S. Falke, C. Grebing *et al.*; «8×10^{-17} fractional laser frequency instability with a long room-temperature cavity»; Opt. Lett. **40**, p. 2112 (2015). 47

[82] C. Lisdat, G. Grosche, N. Quintin *et al.*; «A clock network for geodesy and fundamental science»; Nat. Commun. **7**, p. 12 443 (2016). 47

[83] T. Yang, K. Pandey, M. S. Pramod *et al.*; «A high flux source of cold strontium atoms»; Eur. Phys. J. D **69** (2015). 47, 54

[84] F. Leroux, K. Pandey, R. Rebhi *et al.*; «Non-Abelian adiabatic geometric transformations in a cold Strontium gas»; to be published (2018)`1802.08418v1`. 47, 54

[85] H. Davy; *Elements of chemical philosophy* (London: Johnson and Co.) (1812). 48

[86] R. Veness, S. Karppinen, J. Knaster *et al.*; «Design of beampipes for LHC experiments»; Vacuum **64**, p. 467–473 (2002). 48

[87] A. N. Goncharov, A. E. Bonert, D. V. Brazhnikov *et al.*; «An optical frequency standard based on ultracold magnesium atoms»; J. Phys. Conf. Ser. **793**, p. 012 008 (2017). 49

[88] S. Kraft, F. Vogt, O. Appel *et al.*; «Bose-Einstein Condensation of Alkaline Earth Atoms: ^{40}Ca»; Phys. Rev. Lett. **103** (2009). 49

[89] A. D. Ludlow, M. M. Boyd, J. Ye *et al.*; «Optical atomic clocks»; Rev. Mod. Phys. **87**, p. 637–701 (2015). 49

[90] M. Mills, P. Puri, Y. Yu *et al.*; «Efficient repumping of a Ca magneto-optical trap»; Phys. Rev. A **96** (2017). 49

[91] W. Paul & H. Steinwedel; «Notizen: Ein neues Massenspektrometer ohne Magnetfeld»; Zeitschrift für Naturforschung A **8** (1953). 50

[92] W. W. Smith, D. S. Goodman, I. Sivarajah *et al.*; «Experiments with an ion-neutral hybrid trap: cold charge-exchange collisions»; Appl. Phys. B **114**, p. 75–80 (2013). 50

[93] J. M. Schurer, P. Schmelcher & A. Negretti; «Ground-state properties of ultracold trapped bosons with an immersed ionic impurity»; Phys. Rev. A **90** (2014). 50

[94] H. da Silva Jr, M. Raoult, M. Aymar *et al.*; «Formation of molecular ions by radiative association of cold trapped atoms and ions»; New J. Phys. **17**, p. 045 015 (2015). 50

[95] J. Joger, H. Fürst, N. Ewald *et al.*; «Observation of collisions between cold Li atoms and Yb^{+} ions»; Phys. Rev. A **96** (2017). 50

[96] R. Parker, M. Dietrich, M. Kalita *et al.*; «First Measurement of the Atomic Electric Dipole Moment of ^{225}Ra»; Phys. Rev. Lett. **114** (2015). 50

[97] E. Braaten & H.-W. Hammer; «Universality in few-body systems with large scattering length»; Phys. Rep. **428**, p. 259–390 (2006). 51

[98] I. Bloch, J. Dalibard & W. Zwerger; «Many-body physics with ultracold gases»; Rev. Mod. Phys. **80**, p. 885–964 (2008). 51

[99] G. Baym, J.-P. Blaizot, M. Holzmann *et al.*; «The Transition Temperature of the Dilute Interacting Bose Gas»; Phys. Rev. Lett. **83**, p. 1703–1706 (1999). 51

[100] M. Yasuda, T. Kishimoto, M. Takamoto *et al.*; «Photoassociation spectroscopy of ^{88}Sr : Reconstruction of the wave function near the last node»; Phys. Rev. A **73** (2006). 51, 52

[101] S. Stellmer, M. K. Tey, B. Huang *et al.*; «Bose-Einstein Condensation of Strontium»; Phys. Rev. Lett. **103** (2009). 51, 60

[102] Y. N. M. de Escobar, P. G. Mickelson, M. Yan *et al.*; «Bose-Einstein Condensation of ^{84}Sr»; Phys. Rev. Lett. **103** (2009). 51

[103] S. Stellmer, M. K. Tey, R. Grimm *et al.*; «Bose-Einstein condensation of ^{86}Sr»; Phys. Rev. A **82** (2010). 51

[104] P. G. Mickelson, Y. N. M. de Escobar, M. Yan *et al.*; «Bose-Einstein condensation of ^{88}Sr through sympathetic cooling with ^{87}Sr»; Phys. Rev. A **81** (2010). 51, 52

[105] H. Scheingraber & C. R. Vidal; «Discrete and continuous Franck Condon factors of the Mg_2 A1Σ+u–X1Σ+g system and their J dependence»; J. Chem. Phys. **66**, p. 3694–3704 (1977). 51

[106] E. Ribeiro, A. Zanelatto & R. Napolitano; «High-intensity and ground-state influence on photoassociation line shapes of ^{88}Sr»; Chem. Phys. Lett. **390**, p. 89–93 (2004). 51

[107] E. Tiesinga, B. J. Verhaar & H. T. C. Stoof; «Threshold and resonance phenomena in ultracold ground-state collisions»; Phys. Rev. A **47**, p. 4114–4122 (1993). 51

[108] S. G. Porsev, M. S. Safronova & C. W. Clark; «Relativistic calculations of C_6 and C_8 coefficients for strontium dimers»; Phys. Rev. A **90** (2014). 52

[109] S. Paul, P. R. Johnson & E. Tiesinga; «Hubbard model for ultracold bosonic atoms interacting via zero-point-energy–induced three-body interactions»; Phys. Rev. A **93** (2016). 52

[110] Y. Cheng, J. Jiang & J. Mitroy; «Tune-out wavelengths for the alkaline-earth-metal atoms»; Phys. Rev. A **88** (2013). 52

[111] J. Ruczkowski, M. Elantkowska & J. Dembczyński; «Semi-empirical analysis of the fine structure and oscillator strengths for atomic strontium»; J. Quant. Spectrosc. Radiat. Transfer **170**, p. 106–116 (2016). 52

[112] T. P. Dinneen, K. R. Vogel, E. Arimondo *et al.*; «Cold collisions of Sr*-Sr in a magneto-optical trap»; Phys. Rev. A **59**, p. 1216–1222 (1999). 52, 59

[113] G. Ferrari, R. E. Drullinger, N. Poli *et al.*; «Cooling of Sr to high phase-space density by laser and sympathetic cooling in isotopic mixtures»; Phys. Rev. A **73** (2006). 52

[114] W. Zwerger (rédacteur); *The BCS-BEC Crossover and the Unitary Fermi Gas* (Springer Berlin Heidelberg) (2012). 52

[115] M. Yan, B. J. DeSalvo, B. Ramachandhran *et al.*; «Controlling Condensate Collapse and Expansion with an Optical Feshbach Resonance»; Phys. Rev. Lett. **110** (2013). 52

[116] T. Kraemer, M. Mark, P. Waldburger *et al.*; «Evidence for Efimov quantum states in an ultracold gas of caesium atoms»; Nature **440**, p. 315–318 (2006). 52

[117] S. B. Nagel, P. G. Mickelson, A. D. Saenz *et al.*; «Photoassociative Spectroscopy at Long Range in Ultracold Strontium»; Phys. Rev. Lett. **94** (2005). 52

[118] M. M. Boyd, T. Zelevinsky, A. D. Ludlow *et al.*; «Nuclear spin effects in optical lattice clocks»; Phys. Rev. A **76** (2007). 53

[119] J. von Zanthier, T. Becker, M. Eichenseer *et al.*; «Absolute frequency measurement of the In^+ clock transition with a mode-locked laser»; Opt. Lett. **25**, p. 1729 (2000). 53

[120] S. Stellmer, F. Schreck & T. C. Killian; «Degenerate quantum gases of strontium»; dans «Annual Review of Cold Atoms and Molecules», p. 1–80 (World Scientific) (2014). 54

[121] C. Kwong, T. Yang, M. Pramod *et al.*; «Cooperative Emission of a Coherent Superflash of Light»; Phys. Rev. Lett. **113** (2014). 54

[122] C. Kwong, T. Yang, D. Delande *et al.*; «Cooperative Emission of a Pulse Train in an Optically Thick Scattering Medium»; Phys. Rev. Lett. **115** (2015). 54

[123] J. A. NEUMAN, P. WANG & A. GALLAGHER; «Robust high-temperature sapphire cell for metal vapors»; Rev. Sci. Instrum. **66**, p. 3021–3023 (1995). 55

[124] V. O. LORENZ, X. DAI, H. GREEN *et al.*; «High-density, high-temperature alkali vapor cell»; Rev. Sci. Instrum. **79**, p. 123 104 (2008). 55

[125] J. MITROY & J. ZHANG; «Dispersion and polarization interactions of the strontium atom»; Mol. Phys. **108**, p. 1999–2006 (2010). 55

[126] F. SORRENTINO, G. FERRARI, N. POLI *et al.*; «Laser cooling and trapping of atomic strontium for ultracold atoms physics, high-precision spectroscopy and quantum sensors»; Mod. Phys. Lett. B **20**, p. 1287–1320 (2006). 59

[127] S. STELLMER, B. PASQUIOU, R. GRIMM *et al.*; «Laser Cooling to Quantum Degeneracy»; Phys. Rev. Lett. **110** (2013). 60

[128] T. CHANELIÈRE, L. HE, R. KAISER *et al.*; «Three dimensional cooling and trapping with a narrow line»; Eur. Phys. J. D **46**, p. 507–515 (2007). 60

[129] V. S. LETOKHOV; «Narrowing of the Doppler Width in a Standing Wave»; ZhETF Pis ma Redaktsiiu **7**, p. 348 (1968). 61

[130] V. S. LETOKHOV & B. D. PAVLIK; «Spectral line narrowing in a gas by atoms trapped in a standing light wave»; Applied Physics **9**, p. 229–237 (1976). 61

[131] A. ASHKIN; «Acceleration and Trapping of Particles by Radiation Pressure»; Phys. Rev. Lett. **24**, p. 156–159 (1970). 61

[132] J. E. BJORKHOLM, R. R. FREEMAN, A. ASHKIN *et al.*; «Observation of Focusing of Neutral Atoms by the Dipole Forces of Resonance-Radiation Pressure»; Phys. Rev. Lett. **S41**, p. 1361–1364 (1978). 61

[133] S. CHU, J. E. BJORKHOLM, A. ASHKIN *et al.*; «Experimental Observation of Optically Trapped Atoms»; Phys. Rev. Lett. **57**, p. 314–317 (1986). 61

[134] G. P. AGRAWAL; *Fiber-Optic Communication Systems* (John Wiley & Sons, Inc.) (2002). 65

[135] M. HARIDIM, B. LEMBRIKOV & Y. BEN-EZRA; «Semiconductor Optical Amplifiers»; dans «Advances in Optical Amplifiers», (InTech) (2011). 65

[136] F. D. MAHAD, A. S. M. SUPA'AT, S. M. IDRUS *et al.*; «Analyses of semiconductor optical amplifier (SOA) four-wave mixing (FWM) for future all-optical wavelength conversion»; Optik - International Journal for Light and Electron Optics **124**, p. 1–3 (2013). 66

[137] P. A. Franken, A. E. Hill, C. W. Peters *et al.*; «Generation of Optical Harmonics»; Phys. Rev. Lett. **7**, p. 118–119 (1961). 66

[138] W. P. Risk, T. R. Gosnell & A. V. Nurmikko; *Compact Blue-Green Lasers* (Cambridge University Press) (2003). 66

[139] J. L. Hall, L. Hollberg, T. Baer *et al.*; «Optical heterodyne saturation spectroscopy»; Appl. Phys. Lett. **39**, p. 680–682 (1981). 66

[140] G. C. Bjorklund, M. D. Levenson, W. Lenth *et al.*; «Frequency modulation (FM) spectroscopy»; Applied Physics B Photophysics and Laser Chemistry **32**, p. 145–152 (1983). 66

[141] J. A. Silver; «Frequency-modulation spectroscopy for trace species detection: theory and comparison among experimental methods»; Appl. Opt. **31**, p. 707 (1992). 66

[142] J. M. Supplee, E. A. Whittaker & W. Lenth; «Theoretical description of frequency modulation and wavelength modulation spectroscopy»; Appl. Opt. **33**, p. 6294 (1994). 66

[143] P. Kluczynski, J. Gustafsson, Å. M. Lindberg *et al.*; «Wavelength modulation absorption spectrometry — an extensive scrutiny of the generation of signals»; Spectrochim. Acta, Part B **56**, p. 1277–1354 (2001). 66

[144] G. S. Nolas, J. Sharp & H. J. Goldsmid; *Thermoelectrics* (Springer Berlin Heidelberg) (2001). 67

[145] J. Kim & Y. Song; «Ultralow-noise mode-locked fiber lasers and frequency combs: principles, status, and applications»; Adv. Opt. Photonics **8**, p. 465 (2016). 67

[146] E. Patzak, H. Olesen, A. Sugimura *et al.*; «Spectral linewidth reduction in semiconductor lasers by an external cavity with weak optical feedback»; Electron. Lett. **19**, p. 938 (1983). 67

[147] F. Duarte (rédacteur); *Tunable Lasers Handbook (Optics and Photonics)* (Academic Press) (1996); ISBN 9780080519760. 67

[148] M. G. Littman & H. J. Metcalf; «Spectrally narrow pulsed dye laser without beam expander»; Appl. Opt. **17**, p. 2224 (1978). 67

[149] R. W. P. Drever, J. L. Hall, F. V. Kowalski *et al.*; «Laser phase and frequency stabilization using an optical resonator»; Applied Physics B Photophysics and Laser Chemistry **31**, p. 97–105 (1983). 68

[150] T. Kessler, C. Hagemann, C. Grebing *et al.*; «A sub-40-mHz-linewidth laser based on a silicon single-crystal optical cavity»; Nat. Photonics **6**, p. 687–692 (2012). 68

[151] D. Matei, T. Legero, S. Häfner *et al.*; «1.5 μm Lasers with Sub-10 mHz Linewidth»; Phys. Rev. Lett. **118** (2017). 68

[152] S. R. S. Varadhan & R. J. Williams; «Brownian motion in a wedge with oblique reflection»; Commun. Pure Appl. Math. **38**, p. 405–443 (1985). 85

[153] R. Feynman, R. Leighton & M. L. Sands; «The Feynman Lectures on Physics»; **3**, p. 1–1 (1963). 89

[154] C. V. den Broeck, P. Meurs & R. Kawai; «From Maxwell demon to Brownian motor»; New J. Phys. **7**, p. 10–10 (2005). 89, 90

[155] P. Reimann; «Brownian motors: noisy transport far from equilibrium»; Phys. Rep. **361**, p. 57–265 (2002). 89, 90

[156] V. Dotsenko, A. Maciołek, O. Vasilyev *et al.*; «Two-temperature Langevin dynamics in a parabolic potential»; Phys. Rev. E **87** (2013). 90, 93

[157] H. C. Fogedby & A. Imparato; «A minimal model of an autonomous thermal motor»; EPL (Europhysics Letters) **119**, p. 50 007 (2017). 90

[158] C. Cohen-Tanoudji, A. Aspect, E. Brunet *et al.*; *Einstein aujourd'hui* (EDP SCIENCES) (2005); ISBN 2868837689. 90

[159] P. Visco; «Work fluctuations for a Brownian particle between two thermostats»; J. Stat. Mech. **2006**, p. P06 006 (2006). 90

[160] H. C. Fogedby & A. Imparato; «A bound particle coupled to two thermostats»; J. Stat. Mech: Theory Exp. **2011**, p. P05 015 (2011). 90

[161] H. C. Fogedby & A. Imparato; «Heat fluctuations and fluctuation theorems in the case of multiple reservoirs»; J. Stat. Mech: Theory Exp. **2014**, p. P11 011 (2014). 90

[162] S. Ciliberto, A. Imparato, A. Naert *et al.*; «Statistical properties of the energy exchanged between two heat baths coupled by thermal fluctuations»; J. Stat. Mech: Theory Exp. **2013**, p. P12 014 (2013). 91

[163] S. Ciliberto, A. Imparato, A. Naert *et al.*; «Heat Flux and Entropy Produced by Thermal Fluctuations»; Phys. Rev. Lett. **110**, p. 180 601 (2013). 91

[164] K.-H. Chiang, C.-L. Lee, P.-Y. Lai *et al.*; «Electrical autonomous Brownian gyrator»; Phys. Rev. E **96** (2017). 91

[165] A. Bérut, A. Petrosyan & S. Ciliberto; «Energy flow between two hydrodynamically coupled particles kept at different effective temperatures»; EPL **107**, p. 60 004 (2014). 91

[166] A. Bérut, A. Imparato, A. Petrosyan *et al.*; «Stationary and Transient Fluctuation Theorems for Effective Heat Fluxes between Hydrodynamically Coupled Particles in Optical Traps»; Phys. Rev. Lett. **116** (2016). 91

[167] S. Ciliberto; «Experiments in Stochastic Thermodynamics: Short History and Perspectives»; Phys. Rev. X **7** (2017). 91

[168] P. Strasberg, G. Schaller, T. Brandes *et al.*; «Quantum and Information Thermodynamics: A Unifying Framework Based on Repeated Interactions»; Phys. Rev. X **7** (2017). 91

[169] A. Ryabov, V. Holubec, M. H. Yaghoubi *et al.*; «Transport coefficients for a confined Brownian ratchet operating between two heat reservoirs»; J. Stat. Mech. **2016**, p. 093 202 (2016). 91

[170] V. Holubec, A. Ryabov, M. Yaghoubi *et al.*; «Thermal Ratchet Effect in Confining Geometries»; Entropy **19**, p. 119 (2017). 91

[171] R. Filliger & P. Reimann; «Brownian Gyrator: A Minimal Heat Engine on the Nanoscale»; Phys. Rev. Lett. **99** (2007). 91

[172] A. Argun, J. Soni, L. Dabelow *et al.*; «Experimental realization of a minimal microscopic heat engine»; Phys. Rev. E **96** (2017). 91

[173] V. Mancois, B. Marcos, P. Viot *et al.*; «Two-temperature Brownian dynamics of a particle in a confining potential»; Phys. Rev. E **97** (2018). 91

[174] U. Seifert; «Stochastic thermodynamics, fluctuation theorems and molecular machines»; Rep. Prog. Phys. **75**, p. 58 (2012). 95

[175] A. Crisanti, A. Puglisi & D. Villamaina; «Nonequilibrium and information: The role of cross correlations»; Phys. Rev. E **85** (2012). 98

[176] N. Grønbech-Jensen & O. Farago; «A simple and effective Verlet-type algorithm for simulating Langevin dynamics»; Mol. Phys. **111**, p. 983–991 (2013). 107

[177] T. Walker, D. Hoffmann, P. Feng *et al.*; «A vortex-force atom trap»; Phys. Lett. A **163**, p. 309–312 (1992). 109

[178] T. Dubček, N. Šantić, D. Jukić *et al.*; «Synthetic Lorentz force in classical atomic gases via Doppler effect and radiation pressure»; Phys. Rev. A **89** (2014). 109

[179] N. Šantić, T. Dubček, D. Aumiler *et al.*; «Experimental Demonstration of a Synthetic Lorentz Force by Using Radiation Pressure»; Sci. Rep. **5** (2015). 109

[180] N. Šantić, T. Dubček, D. Aumiler *et al.*; «Synthetic Lorentz force in an expanding cold atomic gas»; J. Opt. Soc. Am. B **34**, p. 1264 (2017). 109

[181] S. Stenholm; «The semiclassical theory of laser cooling»; Rev. Mod. Phys. **58**, p. 699–739 (1986). 109

[182] J. Bailey; «Chirality and the origin of life»; Acta Astronaut. **46**, p. 627–631 (2000). 111

[183] L. Yan, T. Xiong, K. Rehan *et al.*; «Single-Atom Demonstration of the Quantum Landauer Principle»; Phys. Rev. Lett. **120** (2018). 111

[184] A. C. Barato & U. Seifert; «Cost and Precision of Brownian Clocks»; Phys. Rev. X **6** (2016). 111

[185] T. E. Ouldridge, C. C. Govern & P. R. ten Wolde; «Thermodynamics of Computational Copying in Biochemical Systems»; Phys. Rev. X **7** (2017). 111

[186] A. Gaëtan, Y. Miroshnychenko, T. Wilk *et al.*; «Observation of collective excitation of two individual atoms in the Rydberg blockade regime»; Nature Physics **5**, p. 115–118 (2009). 113

[187] T. G. Walker & M. Saffman; «Entanglement of Two Atoms Using Rydberg Blockade»; dans «Advances In Atomic, Molecular, and Optical Physics», p. 81–115 (Elsevier) (2012). 113

[188] L. Isenhower, E. Urban, X. L. Zhang *et al.*; «Demonstration of a Neutral Atom Controlled-NOT Quantum Gate»; Phys. Rev. Lett. **104** (2010). 113

[189] T. Lahaye, T. Koch, B. Fröhlich *et al.*; «Strong dipolar effects in a quantum ferrofluid»; Nature **448**, p. 672–675 (2007). 113

[190] J. B. Balewski, A. T. Krupp, A. Gaj *et al.*; «Rydberg dressing: understanding of collective many-body effects and implications for experiments»; New J. Phys. **16**, p. 063 012 (2014). 113

[191] J. L. Bohn, A. M. Rey & J. Ye; «Cold molecules: Progress in quantum engineering of chemistry and quantum matter»; Science **357**, p. 1002–1010 (2017). 114

[192] W. Zheng & N. R. Cooper; «Anomalous diffusion in a dynamical optical lattice»; Phys. Rev. A **97** (2018). 114

[193] M. Schreiber, S. S. Hodgman, P. Bordia *et al.*; «Observation of many-body localization of interacting fermions in a quasirandom optical lattice»; Science **349**, p. 842–845 (2015). 114

[194] P. Bordia, H. Lüschen, S. Scherg *et al.*; «Probing Slow Relaxation and Many-Body Localization in Two-Dimensional Quasiperiodic Systems»; Phys. Rev. X **7** (2017). 114

[195] M. Reitter, J. Näger, K. Wintersperger *et al.*; «Interaction Dependent Heating and Atom Loss in a Periodically Driven Optical Lattice»; Phys. Rev. Lett. **119** (2017). 114

[196] S. Nakajima, T. Tomita, S. Taie *et al.*; «Topological Thouless pumping of ultracold fermions»; Nat. Phys. **12**, p. 296–300 (2016). 114

[197] G. Grynberg & C. Robilliard; «Cold atoms in dissipative optical lattices»; Phys. Rep. **355**, p. 335–451 (2001). 117

[198] C. M. Dion, S. Jonsell, A. Kastberg *et al.*; «Bimodal momentum distribution of laser-cooled atoms in optical lattices»; Phys. Rev. A **93** (2016). 117

[199] A. Dechant, S. T. Shafier, D. A. Kessler *et al.*; «Heavy-tailed phase-space distributions beyond Boltzmann-Gibbs: Confined laser-cooled atoms in a nonthermal state»; Phys. Rev. E **94** (2016). 117

[200] N. Van Kampen; *Stochastic Processes in Physics and Chemistry*; North-Holland Personal Library (Elsevier Science) (1992); ISBN 9780080571386. 129

[201] M. Lax; «Fluctuations from the Nonequilibrium Steady State»; Rev. Mod. Phys. **32**, p. 25–64 (1960). 129

Vincent MANCOIS **2018**

Sujet : Transition de phase hors d'équilibre et à longue portée: théorie et expérience

---

Resume : Nous avons étudié les effets de la force longue portée résultante de l'absorption de faisceaux lasers dans un nuages d'atomes froids à deux dimensions. La force créée est attractive et reproduit la gravité Newtonienne le long du faisceau. Le nuage d'atomes, composé de strontium 88 (bosons), est refroidi et piégé sur la transition d'intercombinaison. En transférant les atomes dans un piège dipolaire à deux dimensions à la longueur d'onde magique, une transition de phase hors d'équilibre se produit dans l'ensemble canonique. En dessous d'une température critique, un système de particules autogravitantes peut collapser, phénomène rappelant le processus de formation des étoiles. Nous avons observé expérimentalement, des régimes de compressions transitoires, un résultat en partie satisfaisant qui pourrait être amélioré avec l'utilisation de pièges dipolaires plus puissants. La seconde partie de la thèse se penche sur la réalisation théorique d'un moteur Brownien à partir d'un système de particules piégées à deux dimensions, une situation similaire à notre expérience de collapse à deux dimensions. L'obtention d'un moteur Brownien est caractérisée par l'apparition d'un courant macroscopique de particules. Nous avons montré que ce transport est indépendant des détails du piège et dépend seulement d'une double brisure de symétrie : Résultant de la présence de deux bains thermiques suivant deux axes orthogonaux et d'un piège anisotrope désaligné des axes thermiques.

Mots cles : longe portée, atomes froids, hors d'équilibre, moteur Brownien, Smoluchowski, Langevin.

Subject : Non-equilibrium long-range phase transition in cold atoms: theory and experiment

Abstract: We study the long-range force arising from the absorption of non-saturating laser beams in a two-dimensional cloud of cold atoms. The force created by the lasers is attractive and similar to the usual Newtonian gravity along the beam. The cloud is composed of bosonic strontium 88 cooled and trapped on the intercombination line. Transferring the atoms in a two-dimensional optical dipole trap in a magical wavelength configuration, a canonical non-equilibrium phase transition is expected. Below a critical temperature, self-gravitating particles in two dimensions can collapse, nearly by the same mechanism stars are forming. We observed experimentally transient compressions, a halfway satisfactory result originating from the power limitation of our dipole trap. The second part of the thesis focuses on the theoretical realization a minimal Brownian motor within a system of trapped particles in 2D, similarly to our experimental situation. The phenomenon characterizing the Brownian motor is the appearance of a macroscopic current of particles. We have shown that this direct transport of particles is independent of the details of the trapping potential and obtained if and only if two symmetries are jointly broken: By the presence of two heat baths along orthogonal directions together and an anisotropic trap misaligned from the temperature axes.

Keywords : long-range, cold atoms, non-equilibrium, Brownian motor, Smoluchowski, Langevin.